PROCEEDINGS 2024

WELDING TECHNOLOGY 2024:

Industrial development technology of European Union

2nd INTERNATIONAL SCIENTIFIC CONFERENCE

5th November 2024


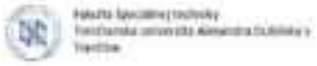





RECENZENTI / REVIEWERS:

Prof. Ing. Milan Marônek, PhD., *Slovak University of Technology in Bratislava, Faculty of Materials Science and Technology in Trnava, Slovakia (SK)*
Assoc. prof. Peter Polák, PhD., *The First Welding Company, Inc. in Bratislava, Slovakia (SK)*
Prof. Dr. József Sárosi, *University of Szeged, Hungary (HU)*
Prof. Dr. György Kovács, *University of Miskolc, Hungary (HU)*
prof. Petro Loboda, DrSc., *National Technical University of Ukraine in Kyiv (UA)*

WELDING TECHNOLOGY 2024
Industrial development technology of European Union

Vydavatel' / Publisher: Vydavateľstvo AlumniPress
J. Bottu 25
917 24 Trnava

Rok vydania / Year of publication: 2024
Vydanie / Issue : prvé / first

ISBN 978-80-8096-307-1
EAN 9788080963071

The organizers of the conference are:

PRVÁ ZVÁRAČSKÁ, a. s. in Bratislava,

STU Faculty of Materials Science and Technology in Trnave (within project APVV-21-0232),

Alexander Dubček University of Trenčín, Faculty of Special Technology.

Vedecký výbor / Scientific Board

Predseda / Chairman:

Dr. h. c. Ing. Peter Fodrek, PhD., hosť. Prof., *The First Welding Company, Inc. in Bratislava, Slovakia (SK)*

Členovia / Members:

Ing. František Kolenič, PhD., *Prvá Zváračská, a. s. Bratislava, Slovakia (SK)*

prof. Ing. Milan Marônek, PhD., *Slovak University of Technology in Bratislava, Faculty of Materials Science and Technology in Trnava, Slovakia (SK)*

Ing. Beáta Šimeková, PhD., *Slovak University of Technology in Bratislava, Faculty of Materials Science and Technology in Trnava, Slovakia (SK)*

Assoc. Prof. Dr. Ing. Pavel Kovačócy, *Slovak University of Technology in Bratislava, Faculty of Materials Science and Technology in Trnava, Slovakia (SK)*

Assoc. Prof. Ing. Jozef Bárta, PhD., *Slovak University of Technology in Bratislava, Faculty of Materials Science and Technology in Trnava, Slovakia (SK)*

prof. Ing. Daniel Kottfer, PhD., *Alexander Dubček University of Trenčín, Faculty of Special technology, Slovakia (SK)*

Assoc. Prof. Ing. Michal Krbaťa, PhD., *Alexander Dubček University of Trenčín, Faculty of Special technology, Slovakia (SK)*

Assoc. Prof. Ing. Róbert Janík, PhD., *Alexander Dubček University of Trenčín, Faculty of Industrial Technologies in Púchov, Slovakia (SK)*

Assoc. Prof. Ing. Marcel Kohutiar, PhD., *Alexander Dubček University of Trenčín, Faculty of Special technology, Slovakia (SK)*

Ing. Ingrid Kovaříková, PhD., *Alexander Dubček University of Trenčín, Faculty of Special technology, Slovakia (SK)*

prof. Ing. Peter Košťál, PhD., *Slovak University of Technology in Bratislava, Faculty of Materials Science and Technology in Trnava, Slovakia (SK)*

Ing. Vanessa Prajová, PhD., *Slovak University of Technology in Bratislava, Faculty of Materials Science and Technology in Trnava, Slovakia (SK)*

prof. Dr. Ing. Steffen Keitel, *SLV Halle, Germeny (DE)*

prof. Volodimir Nesterenkov, DrSc., *Institute of Electric Welding E.O.Patona (PWI) Kiev, Ukraine (UA)*

pplk. doc. Ing. Zbyněk Studený, PhD., *Department of Engineering Technology, Faculty of Military Technology, University of Defence, Brno, Czech Republic (CZ)*

Assoc. Prof. Sergiu-Dan STAN, PhD., Eng., *UTCN Romania (RO)*

Assoc. Prof. Sandra Dedjier, *University of Novi Sad, Serbia (RS)*

kpt. Assoc. Prof. Ing. David Dobrocký, PhD., *Department of Engineering Technology, Faculty of Military Technology, University of Defence, Brno, Czech Republic (CZ)*

prof. Petro Loboda, DrSc., *National Technical University of Ukraine "Igor Sikorsky Kyiv Polytechnic Institute", Ukraine (UA)*

Dr. Ing. Katarzyna Ciosk, *Kielce university of Technology, Poland (PL)*

Assoc. Prof. Milan Rackov, *University of Novi Sad, Serbia (RS)*

Assoc. Prof. Remigiusz Labutsky, *University of Polytechnic, Poznaň, Poland (PL)*

Dr. Róbert Sánta, *University of Dunaújváros, Hungary (HU)*

prof. Dr. József Sárosi, *Szeged Science University, Hungary (HU)*

prof. Lubomir Dimitrov, PhD., *Technical University of Sofia, Bulgaria (BG)*

Assoc. Prof. Dr. Varga Gyula, *University of Miskolc, Hungary (HU)*

prof. Dr. György Kovács, *University of Miskolc, Hungary (HU)*

Assoc. Prof. Dr. M.Sc. Daniel Križan, *Research and Development Department, Business Unit Coil. Voestalpine Steel Division GmbH, 4020 Linz, Austria (AU)*

Programový výbor / Organising Committee

Ing. Beáta Šimeková, PhD., *Slovak University of Technology in Bratislava, Faculty of Materials Science and Technology in Trnava, Slovakia (SK)*

Ing. Ingrid Kovaříková, PhD., *Alexander Dubček University of Trenčín, Faculty of Special technology, Slovakia (SK)*

Ing. Michal Šimek, PhD*., PRVÁ ZVÁRAČSKÁ, a. s. Bratislava, Slovakia (SK)*

Ing. Daniel Dřímal, PhD., *PRVÁ ZVÁRAČSKÁ, a. s. Bratislava, Slovakia (SK)*

Ing. Tomáš Fodrek, *PRVÁ ZVÁRAČSKÁ, a. s. Bratislava, Slovakia (SK)*

Ing. Slavomír Lipár, *PhD., PRVÁ ZVÁRAČSKÁ, a. s. Bratislava, Slovakia (SK)*

Ing. Igor Kováčik, *PRVÁ ZVÁRAČSKÁ, a. s. Bratislava, Slovakia (SK)*

Dr. Róbert Sánta, *University of Dunaújváros, Hungary (HU)*

2ND INTERNATIONAL SCIENTIFIC CONFERENCE
P R O G R A M

WELDING TECHNOLOGY 2024:
Industrial development technology of European Union

5th November 2024

12^{00} – 13^{00} Lunch

12^{30} – 13^{00} Visiting laboratories of PRVÁ ZVÁRAČSKÁ, a. s.

13^{00} Presentation of participants

13^{15} Opening of the scientific conference
Dr. h. c. Ing. Peter Fodrek, PhD., host. prof., general director of PZ, a. s. Bratislava, Slovakia

Section A:
Chairman: Ing. František Kolenič, PhD., PRVÁ ZVÁRAČSKÁ, a. s. Bratislava, Slovakia

13^{20} PULSED ELECTRON BEAM WELDING USING A DYNAMIC CATHODE BOMBARDMENT VOLTAGE SOURCE
Darovec R., Kolenič F. Sekerka R., Koršňák P. (PRVÁ ZVÁRAČSKÁ, a. s. Bratislava)

13^{40} EDDY CURRENT TESTING OF SELECTIVE LASER MELTED AlSi10Mg ALLOY
Gaľetko M., Hatala M., Botko F., Vandžura R. (Faculty of Manufacturing Technologies, Technical University of Košice)

14^{00} THE PROCESS OF MEASURING AND EVALUATING SELECTED ELECTRON BEAM PARAMETERS
Kováč Ľ., Dřímal D., Fodrek T. (PRVÁ ZVÁRAČSKÁ, a. s. Bratislava)

14^{20} WELDING REQUIREMENTS HETEROGENEOUS WELDED JOINTS OF MATERIALS HIGH-STRENGTH STEEL HARDOX 500 AND ASUTENITE STEEL 08CH18N10T FOR NUCLEAR POWER PLANT
Macháček J., Kianicová M., Kovaříková I. (Alexander Dubček University of Trenčín, Faculty of Special Technology)

14^{40} COMPARISON OF THE EFFICIENCY OF CALCULATIONS OF MINIMUM WALL THICKNESSES OF SMALL-CALIBER BARRELS
Polášek M., Bilka M., Kohutiar M., Maryáš J. (Alexander Dubček University of Trenčín, Faculty of Special Technology, VTÚVM, Czech Republic)

15^{00} MODIFICATION OF THE ELECTRON BEAM GENERATION SYSTEM TO INCREASE THE DYNAMICS OF THE WELDING CURRENT CONTROL
Sekerka R., Kolenič F., Koršňák P. (PRVÁ ZVÁRAČSKÁ, a. s. Bratislava)

Section B:
Chairman: Ing. Ingrid Kovaříková, PhD., Alexander Dubček University of Trenčín, Faculty of Special technology, Slovakia

15^{20} EXAMPLES OF LASER WELDING IN INDUSTRIAL PRACTICE
Šimek M., Kolenič F., Fodrek T., Šimeková B. (PRVÁ ZVÁRAČSKÁ, a. s. Bratislava, MTF STU Trnava)

15^{40} STUDY OF WETTABILITY OF BI-AG-TI-(MG) – BASED SOLDERING ALLOYS ON CERAMIC SUBSTRATES SOLDERED BY LASER-ULTRASOUND TECHNOLOGY
Sloboda M., Koleňák R., Gabrhel T., Meluš T., Gogola P., Milde J., Šimek M. (PRVÁ ZVÁRAČSKÁ, a. s. Bratislava, MTF STU Trnava)

16^{00} POSSIBILITIES OF IMPLEMENTING LSP TECHNOLOGY TO IMPROVE ESSENTIAL SURFACE INTEGRITY INDICATORS ON MATERIALS FOR AUTOMOTIVE INDUSTRY
Šajgalík M., Czánová T., Holubják J., Joch R., Cedzo M., Matúš M., Kasenčák M. (PRVÁ ZVÁRAČSKÁ, a. s. Bratislava, Faculty of Mechanical Engineering, University of Žilina)

16^{20} LASER WELDING OF ALUMINUM ALLOY AW6005A USING BRIGHTLINE TECHNOLOGY
Dřímal D., Oselský M., Nerád R., Ormandy R. (PRVÁ ZVÁRAČSKÁ, a. s. Bratislava)

16^{40} POSSIBILITIES OF INCREASING THE RANGE OF ARTILLERY AMMUNITION CALIBER 15MM – M107
Timárová Ľ., Krbaťa M., Kakošová L., Fekiač J.J. (Alexander Dubček University of Trenčín, Faculty of Special Technology)


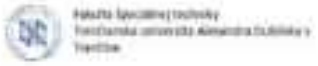





OBSAH / CONTENTS








PULSED ELECTRON BEAM WELDING USING A DYNAMIC CATHODE BOMBARDMENT VOLTAGE SOURCE

Ing. Roman Darovec[1]
Ing. František Kolenič, PhD.[2]
Ing. Rastislav Sekerka[3]
Ing. Peter Koršňák[4]
1ORCID: 0000-0002-7570-864X, PRVÁ ZVÁRAČSKÁ, a.s, **Slovakia**
2ORCID: 0000-0001-9920-2398, PRVÁ ZVÁRAČSKÁ, a.s, **Slovakia**
3ORCID: 0000-0001-6968-367X, PRVÁ ZVÁRAČSKÁ, a.s, **Slovakia**
4ORCID: 0000-0003-2771-556X, PRVÁ ZVÁRAČSKÁ, a.s, **Slovakia**

Abstract: This report deals with the issue of designing a solution for the pulsation of the welding current I_Z by modulating the auxiliary bombardment voltage U_B, as the main parameter, by controlled change of which we will also achieve a controlled change of the welding current I_Z. This document describes the phenomenon of how the modulation (ripple) of the bombardment voltage U_B modulates the time course of the welding current I_Z (pulsation of the I_Z) and describes the way in which we can use the dynamic bombardment voltage U_B source to control such a time change of the welding current I_Z directly in the production process. It describes the technical solution of the dynamic bombardment voltage U_B source based on a fast pulse source and the implementation of these new type of pulse bombardment voltage U_B source into new and original versions of welding Energoblocks, where they fully replace the original linear bombardment voltage U_B sources in order to improve the result of the welding process by modulating the welding current I_Z.
Keywords: electron beam welding, thermoemission cathode, modulation of the of the welding current, pulse source

1. INTRODUCTION

The welding process in electron beam welding is a complex process, the quality and stability of which is influenced by many factors, whether it is the stability of the welding parameters and the performance of the welding Energoblock itself, the stability of the vacuum during the welding process, and the material of the weldment or workpiece itself. In an ideal welding process, all necessary parameters of the welding process are stable with minimal ripple (welding voltage U_Z, control voltage U_W, bombardment voltage U_B, focusing current I_F), which achieves a stable welding current I_Z with constant power (Schultz, 2004). In the welding process, it is therefore very important that the energy that we distribute to the weldment material by the electron beam is constant during the welding process and that the electron beam has sufficient sharpness. In this way, we significantly eliminate possible defects in the weld joint, reduce pores in the weld joint and ensure the necessary depth of the weld material. During our practice of welding different materials, we have come to the realization

that when welding different types of materials, some materials (e.g. materials based on aluminum alloys) exhibit a higher frequency of defects in the weld joint during a welding process with stable parameters, which is a consequence of higher gassing of material in the weld bath (Węglowski at all, 2016). The weld joint thus exhibits a higher number of pores, the weld depth is insufficient and the weld joint surface is wrinkled. Such materials therefore require a different approach to welding technologies than other materials. Through long-term research into the welding technology of materials based on aluminum alloys, we have found that these materials are best welded if the energy distributed to the weld joint is modulated with a certain frequency, which means that the welding current I_Z (electron beam) is pulsed with a certain frequency and a certain ripple (modulation depth), which is determined by the welding technology itself for the given type of material based on aluminum alloys. By appropriately selected frequency and depth of pulsation of the welding current I_Z, we can significantly reduce the gas formation of these materials during the welding process (reduction of pores in the weld) and appropriately form the weld pool. For example, for welding HVH heat exchangers for electric vehicles (AlMgSiFe alloy), it is suitable to pulsate the welding current I_Z with a frequency of 100Hz with a pulsation depth of approximately 50% (Schubert, 2021).

2. PRINCIPLES OF WELDING CURRENT I_Z PULSATION

The first way to pulsate the welding current I_Z is the principle of modulating the desired value of the welding current I_Z itself so that the desired value of I_Z will consist of a direct and alternating component, each of which will be separately adjustable. By combining the settings of these two components, we can arbitrarily pulsate the welding current I_Z. The modified desired value of I_Z is processed by the welding current regulator I_Z and the I_Z regulator controls the control voltage U_W of the control electrode (Wehnelt) so that the real welding current I_Z will copy the modulated desired value of I_Z. This method of pulsating the welding current I_Z has the advantage that it is universal and therefore we can pulsate any selected shape of the welding current I_Z (SINUS, TRIANGLE, SQUARE) with 100% pulsation depth and any selected frequency of the welding current I_Z. However, here we encounter the limits of our control loop (Regulator I_Z → Control voltage U_W source → HV (High Voltage) cable → Electron beam gun), while in particular the capacitance of the filter capacitors of the control voltage U_W source and the capacitance of the HV cable cause a slow response of the control loop to a rapid change in the setpoint I_Z, which results in the fact that the control loop does not have time to react to a setpoint I_Z with a frequency higher than 100 Hz with a corresponding change of the control voltage U_W on the Wehnelt electrode. The real waveform of the welding current I_Z (measured I_Z value) is deformed as a result and the pulsation depth is reduced.

The second way to pulsate the welding current I_Z is the principle of modulation of the control voltage U_W by modulating (ripple) the voltage of the bombardment voltage U_B source, while changing the control voltage U_W directly pulsates the welding current I_Z at a constant desired value of I_Z. The I_Z regulator tries to counteract the change in the welding current I_Z from the

desired value of I_Z, which remains constant, but due to the slow control loop, the I_Z regulator cannot suppress this change in the welding current I_Z, but only partially limits it. The time course of the welding current I_Z thus approximately copies the time course of the bombardment voltage U_B. The principle of pulsation of the welding current I_Z by modulating the bombardment voltage U_B is explained in the following figure (Fig. 1).

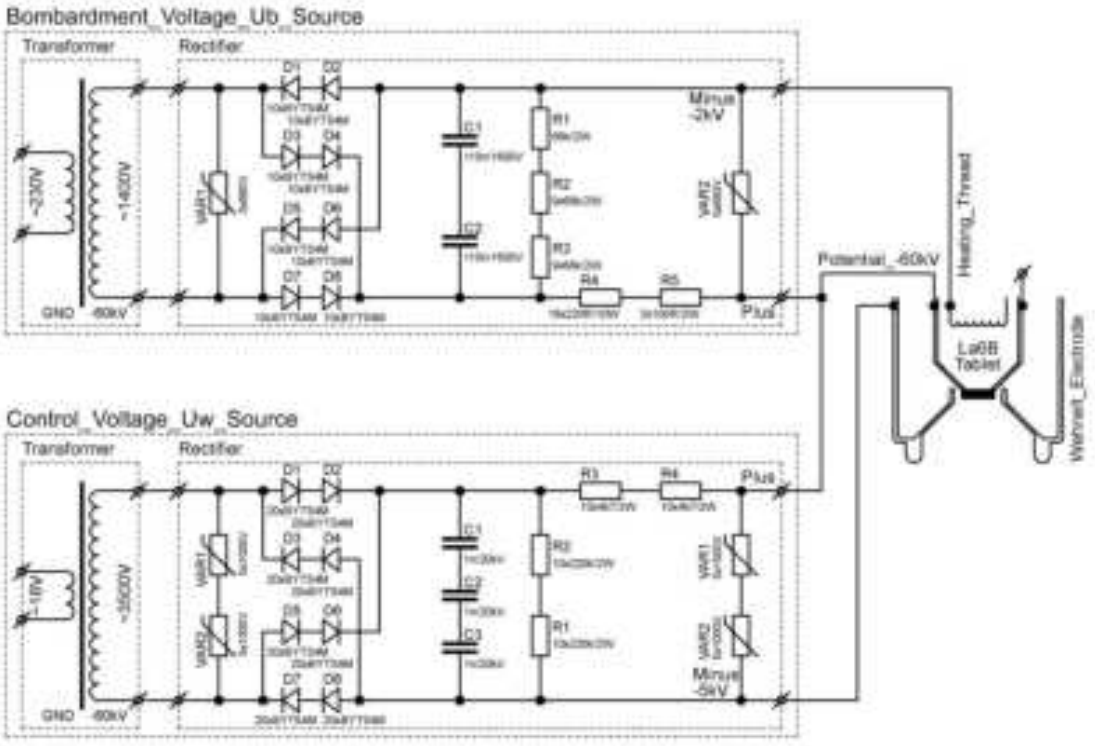

Fig. 1. Connection of bombardment voltage U_B source, control voltage U_W source with electrodes of electron beam gun

In Fig. 1 we have shown the connection of the auxiliary sources (bombardment voltage U_B source, control voltage U_W source) with the electrodes of the electron beam gun, specifically with the Wehnelt electrode and the LaB_6 tablet holder. Both auxiliary sources are connected with their positive poles (plus) to the HV (High Voltage) potential of -60kV, while the negative pole (minus) of the bombardment voltage U_B source (-2kV) is connected to the tablet holder or the LaB_6 tablet and the negative pole (minus) of the control voltage U_W source (-5kV) is connected to the Wehnelt electrode. The negative pole of the bombardment voltage U_B source is connected via a resistor divider (resistors R1, R2, R3, R4, R5) to the negative pole of the control voltage U_W source via its resistor divider (resistors R4, R3, R2, R1), which implies that a change in the bombardment voltage U_B via these resistor dividers will little modulate the control voltage U_W.

Pulsation of the welding current I_Z by the dynamic change of the time course of the bombardment voltage U_B

As we explained in the previous part, the welding current I_Z can be pulsated by changing the time course of the bombardment voltage U_B, because this time change of the bombardment voltage U_B modulates the control voltage U_W on the Wehnelt electrode through the resistor dividers. In order to dynamically change the time course of the bombardment voltage U_B, we must replace the original linear bombardment voltage U_B source with a fast pulse source that can flexibly respond to the requirement of a dynamic change of the bombardment voltage U_B during the welding process. The parameters of the new pulse bombardment voltage U_B source were specified with regard to the requirements of the welding process technology of HVH heat exchangers as follows:

- Maximum value of the bombardment voltage U_B: U_{BMAX} = 2kV
- Maximum power of the source: P_{MAX} = 70W
- Maximum frequency of the bombardment voltage U_B: f_{MAX} = 500Hz
- Bombardment voltage modulation range: 0% ÷ 80%

3. PULSE BOMBARDMENT VOLTAGE U_B SOURCE

The basis of the new pulse bombardment voltage U_B source is the Two Switch Flyback topology (Fig. 2), which is characterized by the use of two switching transistors Q_1 and Q_2, which reduce their voltage stress in the off state. The topology is suitable for higher output voltage (Flyback transformer), is simple (simple rectifier and filtration), durable and has the advantage of galvanic separation of the primary and secondary sides of the source (Flyback transformer).

The transfer of energy from the primary side to the secondary side of the pulse source runs in two steps:

- Switching transistors Q_1 and Q_2 are in the on state:
  - Primary current I_{PRI} flows through the primary winding (N_P) of the Flyback transformer
  - Rectifier diode D_1 is polarized in the reverse direction (secondary voltage on the secondary winding (N_S) has negative polarity)
  - The core of the Flyback transformer is charged with electromagnetic energy
- Switching transistors Q_1 and Q_2 are in the off state:
  - Primary current I_{PRI} does not flow through the primary winding (N_P) of the Flyback transformer
  - The polarity of the secondary voltage on the secondary winding (N_S) is reversed (positive voltage), rectifier diode D_1 is forward polarized
  - Secondary current I_{SEC} flows through the secondary winding (N_S)
  - Electromagnetic energy of the Flyback transformer core in the form of secondary current I_{SEC} charges the filter capacitor C_O

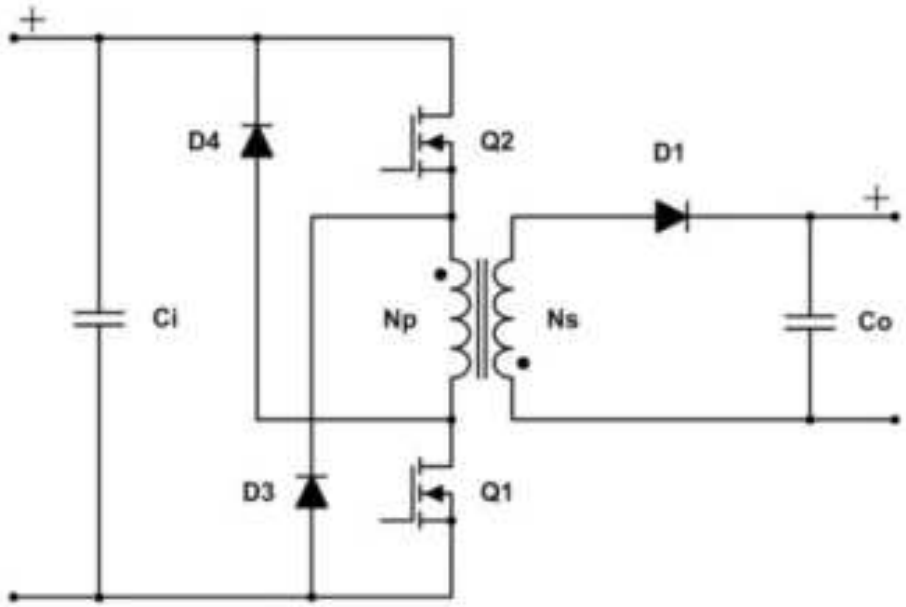

Fig. 2. Two Switch Flyback Topology

Boundary conduction mode

The pulse bombardment voltage U_B source operates in the BCM (Boundary Conduction Mode) mode (Fig. 3), which determines how the energy will be transferred from the primary side to the secondary side of the pulse source to the filter capacitors or to the source output. In BCM mode, the excitation of the primary winding of the Flyback transformer (charging the core with electromagnetic energy) occurs only after the secondary current flowing through the secondary side of the source has ceased (the electromagnetic energy of the core has been exhausted). In this way, we reduce the ripple of the source output voltage and reduce losses on the rectifier diode, because we use all the electromagnetic energy stored in the Flyback transformer core and at the same time do not saturate the core. The pulse source, which operates in the BCM mode, is controlled by feedback based on the sensing of the secondary current so that it adapts its switching frequency to the current load in order to deliver the required power with minimal output voltage ripple.

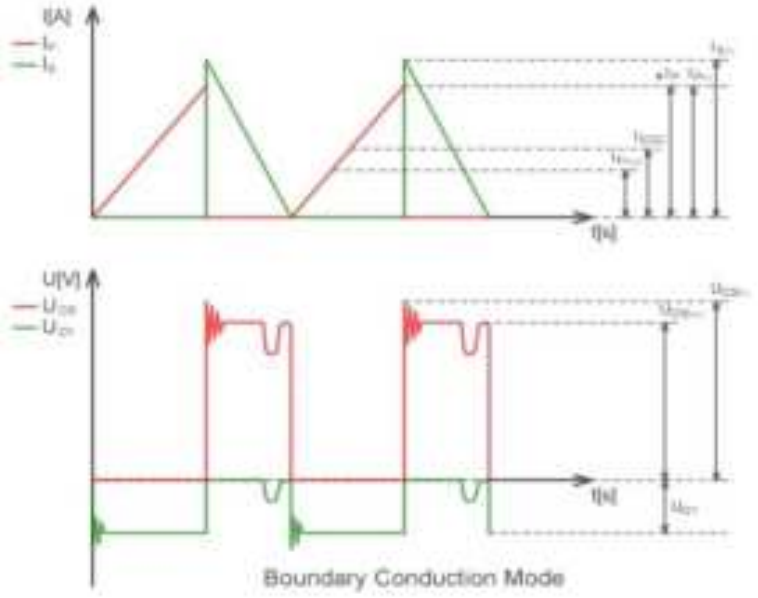

Fig. 3. Voltage time course in Boundary Conduction Mode

Block diagram of the pulse bombardment voltage U_B source

From the block diagram (Fig. 4) it is obvious that pulse bombardment voltage U_B source consists from two main parts, primary part and secondary part. Primary part of the source remains from electrical circuits of the primary driver and secondary part of the source remains from the block of rectifier/filtration and from the block of feedback/regulation. The Flyback transformer performs energy transfer from the primary part of the source to the secondary part of the source. Transformer is applied with >100kV insulation strength between the primary and secondary windings and galvanically separates the primary part of the source (GND potential) from the secondary part of the source (HV potential (-60kV)). The primary part of the source, which is responsible for the excitation (energization) of the Flyback transformer, is controlled by two feedbacks from the secondary side of the source, namely:

- FDB (Feedback) - feedback that controls the switching frequency of the source and the total power of the source (control of the power of the source):
  - Sensing the secondary current of the source on the sensing resistor R_S
  - Sensing the output voltage of the source on the sensing resistor R_{DY}
- OVP (Over Voltage Protection) - feedback that blocks switching of the source when the source output is overvoltage (source protection function)
  - Sensing the output voltage of the source on the sensing resistor R_{OY}

The signals of both feedback links are transmitted to the primary part of the source by an optical fiber (TOSLINK), due to the galvanic separation of the primary and secondary parts of the source.

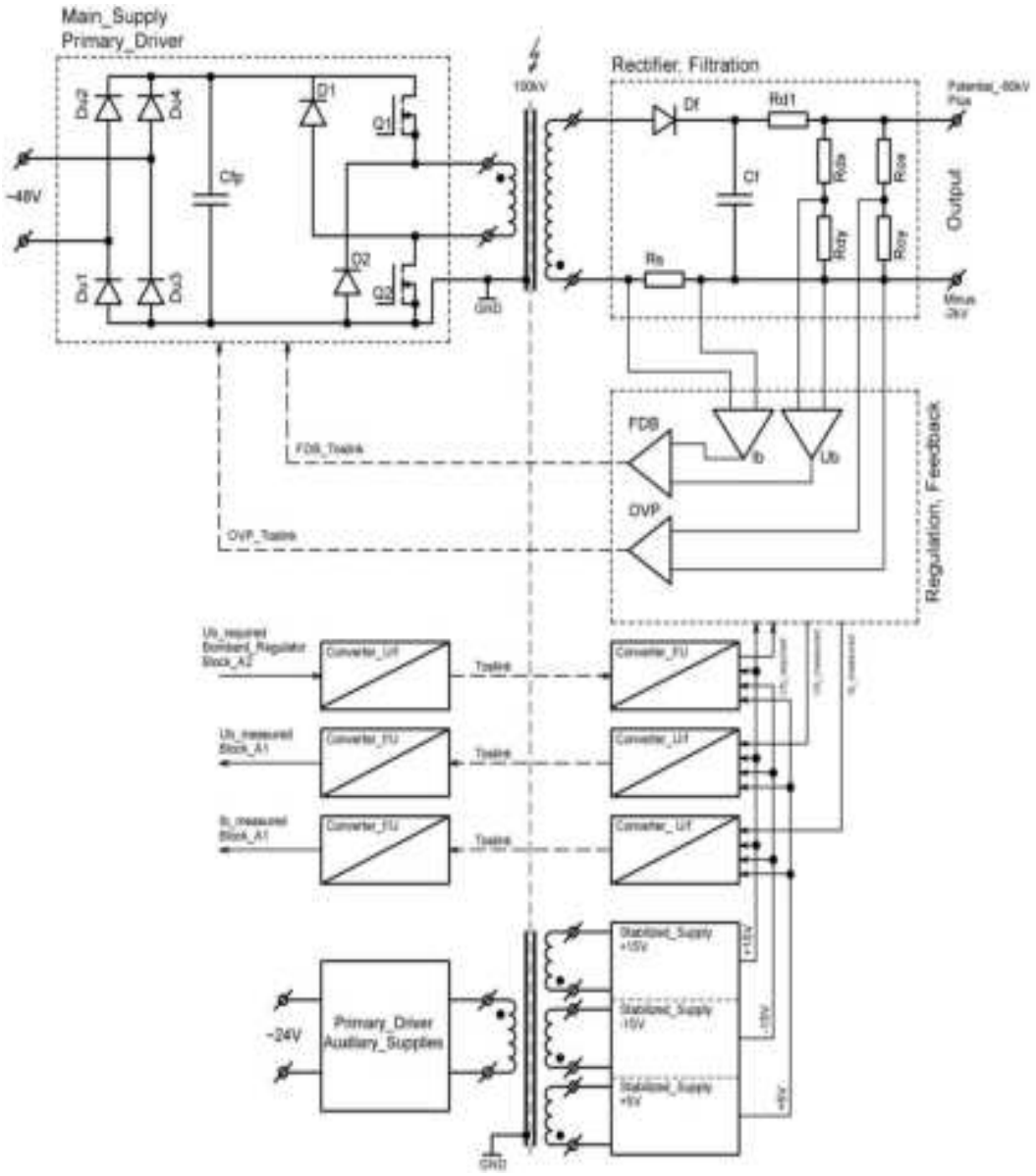

Fig. 4. Block diagram of the pulse bombardment voltage U_B source

The pulse bombardment voltage U_B source has three optical channels, of which two optical channels are used to measure the output voltage U_B and the output current I_B (U/f converter (sec. part) → TOSLINK → f/U converter (pri. part)) and the third optical channel is used to transmit the desired value of the bombardment voltage U_B (U/f converter (pri. part) → TOSLINK → f/U converter (sec. part)).

The last part of the pulse bombardment voltage U_B source is the auxiliary source of supply voltages of the secondary part of the source and measurement channels. It is a simple pulse

source without feedback control that oscillates at basic frequency, which is set in the primary part of the source. The flyback transformer with >100kV insulation strength has three secondary windings connected to the secondary part of the source, which consists of three separate rectifiers with filtering and voltage stabilization +15V, -15V and +5V.

Feedback FDB and OVP

As we have already mentioned in the previous part of the document, feedback FDB (Feedback) controls the performance of the source and feedback OVP (Over Voltage Protection) blocks the source in case of overvoltage of the output voltage.

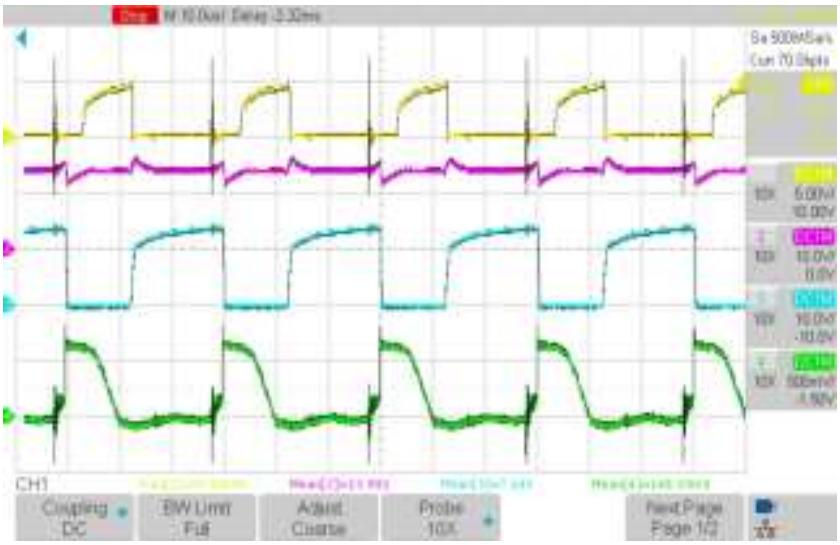

Fig. 5. Time courses of the basic FDB feedback signals

The basis of the power control (feedback FDB, Fig. 5) of the pulse bombardment voltage U_B source, which works in the BCM mode, is the sensing of the size of the secondary current I_{SEC}, which flows through the secondary part of the source (green signal). We recognize two basic operating states of the source according to the secondary current of I_{SEC}:

- $I_{SEC} > 0$ - blocking the switching of the primary part of the source, pumping electromagnetic energy from the core to the filter capacitors in the form of a secondary current I_{SEC}:
  - The output of the current comparator (blue signal) is in negative saturation (Log.0) ($I_{SEC} > 0$)
  - The output of the voltage comparator (purple signal) is in positive saturation (Log.1) ($U_B < U_{DES}$) (the output voltage U_B is less than the desired value of the output voltage U_{DES})
  - The optical receiver (yellow signal) on the primary side of the source is switched off (Log.1), blocking the switching of the source

- I_{SEC} = 0 - enabling the switching of the primary part of the source, fueling the core with electromagnetic energy:
  - The output of the current comparator (blue signal) is in positive saturation (Log.1) (I_{SEC} = 0)
  - The output of the voltage comparator (purple signal) is in positive saturation (Log.1) ($U_B < U_{DES}$) (the output voltage U_B is less than the desired value of the output voltage U_{DES})
  - The optical receiver (yellow signal) on the primary side of the source is switched on (Log.0), enable switching of the source

The current comparator in the control part of the source is controlled by the secondary current I_{SEC}, on the contrary, the voltage comparator compares the desired value U_{DES} of the bombardment voltage U_B with its measured value and, when $U_{DES} < U_B$, blocks the switching of the source through feedback FDB. In this way, the pulse bombardment voltage U_B source regulates the required output power depending on the load of the source and the desired value U_{DES} of the bombardment voltage U_B. The feedback OVP (Over Voltage Protection) has a protective function based on sensing the overvoltage at the output of the source, which must not exceed the value of 2100V. If this happens, the OVP feedback immediately blocks the switching of the source until the overvoltage disappears.

The duty cycle of the pulse bombardment voltage U_B source

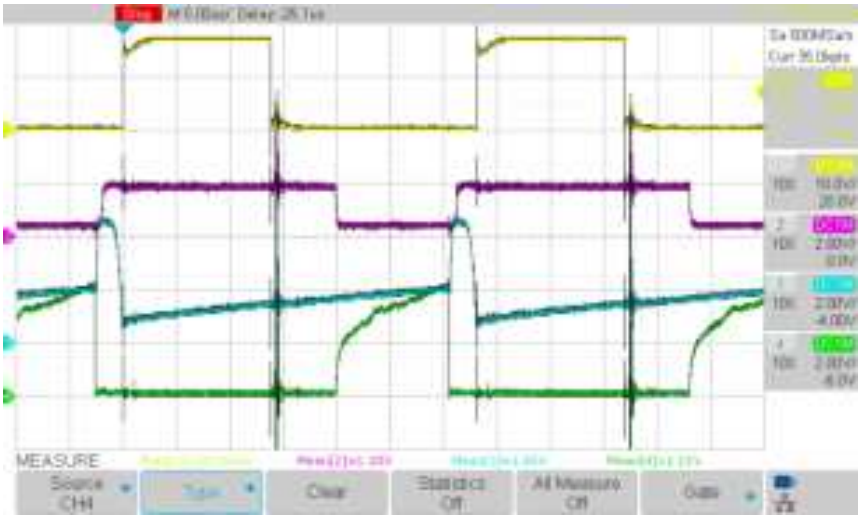

Fig. 6. Time courses of the basic signals of the primary driver of the pulse bombardment voltage U_B source

From the time courses (Fig. 6), it is clear that after the blocking of the source switching (output of the optical receiver in log. 0) (green signal) is immediately generated synchronization pulse (blue signal), which resets the primary driver and if the control signal (purple signal) is greater than 1V, the generation of a new switching pulse (yellow signal) follows, resulting in a new saturation of the transformer core. The generation of the synchronization pulse and the control signal is directly controlled by the signal from the FDB feedback, which means that if the FDB feedback is inactive, the control signal (purple signal) is zero and the switching of the source is blocked. The synchronization pulse is important for synchronizing the switching of the source with the course of the secondary current I_{SEC}, so that the primary driver generates a new switching pulse after the disappearance of the secondary current ISEK, because otherwise the switching would only take place at the basic set frequency and the source would not reach the required power.

Dynamics of the pulse bombardment voltage U_B source

Source dynamics is the response of the source to the input dynamic signal, or it is feature of the source to copy a rapidly changing input signal while maintaining the set power. The dynamics of the pulse bombardment voltage U_B source was tested with the required parameters:

- Output voltage - U_B = 2kV
- Output power - P = 70W
- Depth of pulsation - 0% ÷ 80%
- Frequency - 100Hz ÷ 500Hz
- Type of the input signal:
  - Sinus
  - Square

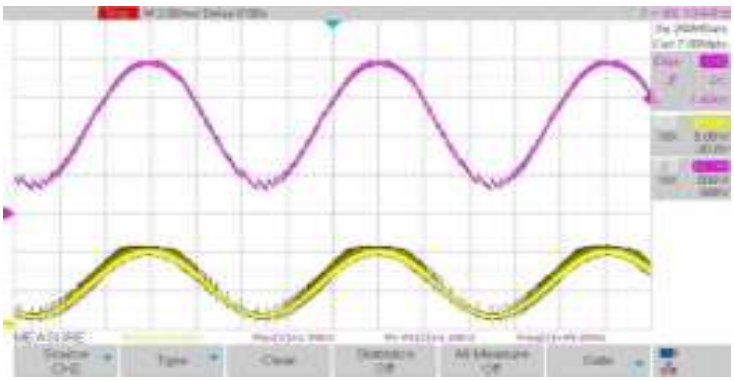

Fig. 7. Response of the output (purple signal) of the pulse source U_B to the input sinusoidal signal with a frequency of 100Hz (yellow signal)

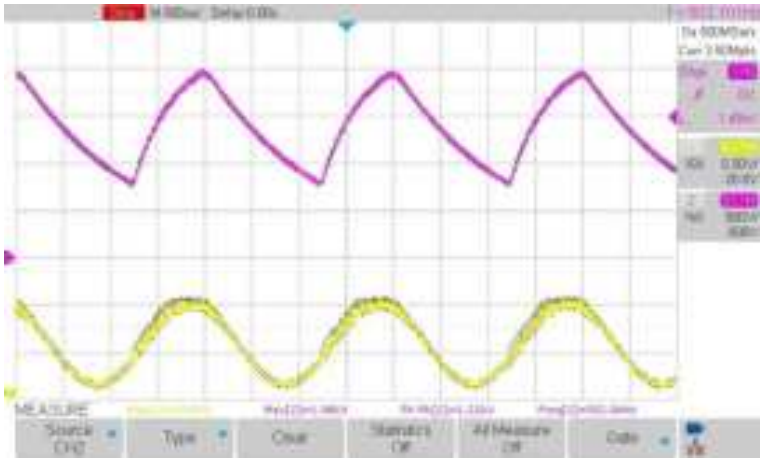

Fig. 8. Response of the output (purple signal) of the pulse source U_B to the input sinusoidal signal with a frequency of 500Hz (yellow signal)

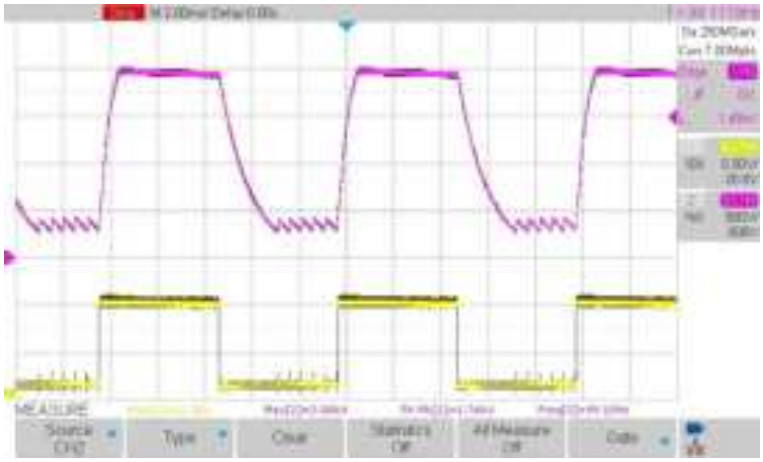

Fig. 9. Response of the output (violet signal) of the pulse source U_B to the input square signal with a frequency of 100Hz (yellow signal)

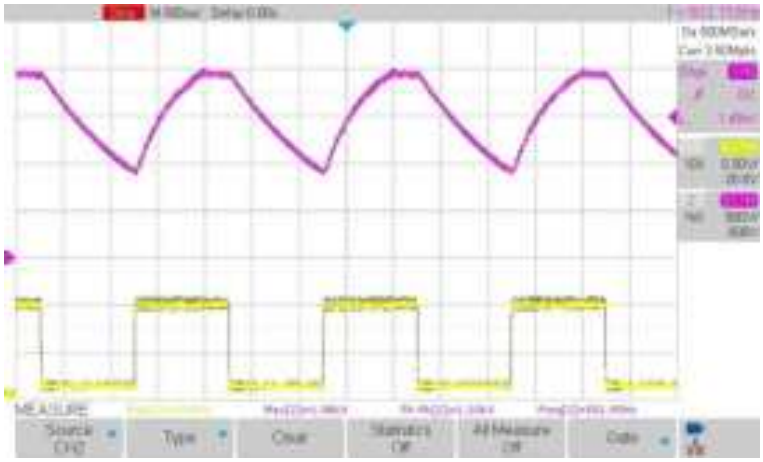

Fig. 10. Response of the output (purple signal) of the pulse source U_B to the input square signal with a frequency of 500Hz (yellow signal)

The following image (Fig. 11) shows a time course of the pulsated welding current I_Z, which is modulated by the bombardment voltage U_B with a modulation depth of 70% and a frequency of 100Hz. This time course of the welding current I_Z in fig. 11 shows the real welding current I_Z, which is welded the circuit of the HVH heat exchanger. The energy is supplied to the weld joint in energy pulses and not continuously, which improves the properties of the weld joint.

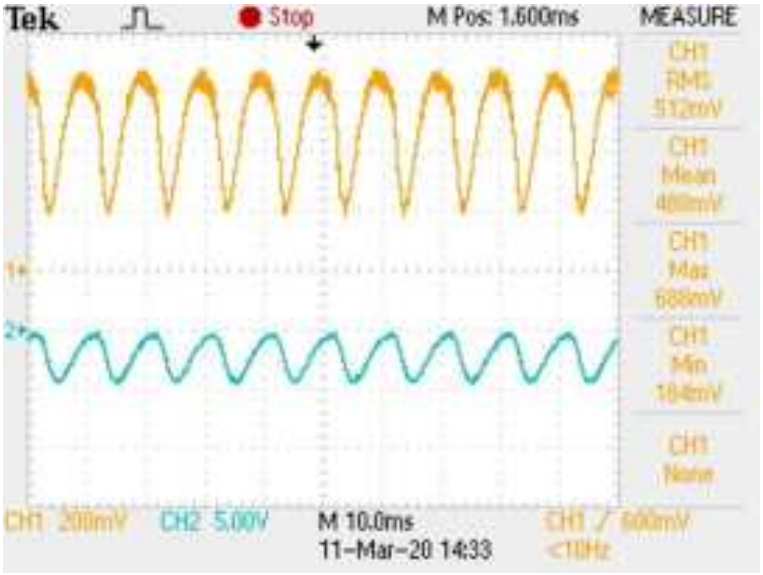

Fig. 11. Time course of the pulsated welding current I_Z (yellow signal) and the output of the welding current regulator I_Z (blue signal)

As we can notice from the pulsated time course of I_Z (Fig. 11), the time course of I_Z does not exactly have the form of a sine function, even though the welding current is pulsated by the bombardment voltage U_B with a sinusoidal course. This is caused by the time delay of the welding current regulation loop I_Z, which is formed by the welding current regulator I_Z and the control voltage source U_W. The control voltage U_W source mainly contributes to the time delay, respectively the time delay of the control loop depends on the size of the filtering capacity of the control voltage U_W source and also on the capacity of the HV cable itself, which connects the electron beam gun to the system of auxiliary sources (sources U_B and U_W).

Practical realization of the pulse bombardment voltage U_B source

As we have already mentioned, the pulse bombardment voltage U_B source is composed of two parts, namely the primary part and the secondary part, which are connected at two different potentials, the difference being 60kV. The practical realization of the pulse source must respect this fact and therefore the primary part of the source, primary driver, implemented in a typed box from the Schroff company as part of the auxiliary power supply stand (GND potential) (Fig. 11).

Fig. 12. The primary part of the pulse source with individual modules of the main and auxiliary source drivers

The secondary part of the source with Flyback transformer, rectifier, filtering, control and measurement is placed for EMC in a black rack aluminum box in a Small container (HV potential (-60kV)).

Fig. 13. The secondary part of the source is placed in a black aluminum box

This combination of primary and secondary part of the pulse bombardment voltage U_B source can be easily integrated into older types of EBW machines.

4. CONCLUSION

The pulsation of the welding current I_Z is necessary when welding certain types of materials to achieve a high-quality weld without pores and defects in the weld joint. The previous methods of pulsation the welding current I_Z (change in the filtration capacity of the linear source U_B) over time appeared to be insufficiently effective for the needs of the welding process technology. The pulse bombardment voltage U_B source brings new possibilities of pulsation of the welding current I_Z not only by changing the frequency of pulsation, but also by changing the depth of pulsation and the shape of the signal, which was not possible with the previous type of pulsation I_Z. At the same time, the pulse source U_B also includes the optical measurement channels of the bombardment voltage U_B and the bombardment current I_B, which gives the operator a better overview of the parameters of the welding process. During the trial deployment of the pulse source U_B in the production process of HVH heat exchangers, the reliability of the topology of the pulse source U_B was confirmed.

ACKNOWLEDGEMENTS

This work was supported by Agency for the Support of Research and Development under Contract No. APVV 18-0402.

REFERENCES

Schultz H.: Electron Beam Welding, Cambridge: Abingdon Publishing, England, 2004, ISBN 1-85573-050 2.

Węglowski M., Błacha S., Phillips A.: Electron beam welding – Techniques and Trends – Review, Vacuum Journal, Volume 130, August 2016, Pages 72-92

G. Schubert: Electron Beam Welding – Process, Applications and Equipment, PTR-Precision Technologies Inc, Enfield, 2021

Jim Williams: Analog Circuit Design, 1991

George Clayton, Steve Winder: Operational Amplifiers, 2003

EDDY CURRENT TESTING OF SELECTIVE LASER MELTED AlSi10Mg ALLOY

Eng. MSc. Matúš Geľatko, PhD.[1]
Dr. h.c. prof. Eng. MSc. Michal Hatala, PhD.[2]
assoc. prof. Eng. MSc. František Botko, PhD.[3]
Eng. MSc. Radoslav Vandžura, PhD.[4]
[1]ORCID: 0000-0003-3047-7232, Faculty of Manufacturing Technologies, Technical University of Košice with a Seat in Prešov, 080 01 Prešov, **Slovakia**
[2]ORCID: 0000-0001-8943-1584, Faculty of Manufacturing Technologies, Technical University of Košice with a Seat in Prešov, 080 01 Prešov, **Slovakia**
[3]ORCID: 0000-0001-9728-9004, Faculty of Manufacturing Technologies, Technical University of Košice with a Seat in Prešov, 080 01 Prešov, **Slovakia**
[4]ORCID: 0000-0002-3837-6340, Faculty of Manufacturing Technologies, Technical University of Košice with a Seat in Prešov, 080 01 Prešov, **Slovakia**

Abstract: Different properties of Additive Manufactured (AM) aluminium alloy can influence the identification using the Eddy Current Testing (ECT) method, which has predispositions for effective evaluation of its surface and subsurface layers. Important is mainly the lower density and higher electrical conductivity. The presented study is a part of larger research focused on the creation of methodology for the ECT identification of AM components. The described experiment is focused on the identification of surface notch-type artificial defects of various orientations and positions in depth, surface artificial clusters of pits and subsurface artificial clusters composed of spherical cavities including unmolten powder. Within the preparation of experiment, a lift-off diagram and a standard penetration depth diagram are interpreted. The main part includes ECT identification of four specimens with the above-mentioned artificial defects with the description of the signal curve characteristics. Obtained results represent an important contribution to the information basis for a design of subsequent experiments within research.
Keywords: additive manufacturing, aluminium alloy, non-destructive testing

1. INTRODUCTION

Additive Manufacturing (AM) represents a modern and sophisticated approach for the creation of complex functional parts. Selective Laser Melting (SLM) technology operates with materials in the form of powder, which are melted using the laser power, whereas the final component is created after solidification layer-by-layer. SLM metal materials are well-known

for their different properties in comparison with their conventional equivalents, mainly in the case of a density. The Eddy Current Testing (ECT) method provides possibilities in reliable non-destructive identification of defects in surface layers of materials, however mentioned density can influence the effectiveness of ECT. Also, influential is higher electrical conductivity of the aluminium based materials. Recent studies in the field of ECT of AM parts were devoted to the measurement of a density (Spurek et al., 2022), identification of defects (Ehlers et al., 2020), or simulations of signal-to-defect variations (E. Farag et al., 2022) in various materials on the base of stainless steels (Geľatko et al., 2022), nickel-based alloys (Guo et al., 2021), or titanium alloys (Du et al., 2018). It is necessary to evaluate the influence of various types and sizes of defects on the ECT signal within a certain part of the comprehensive research, what is the main objective of this partial experiment, whereas the aluminium alloy is the material of interest.

2. METHODOLOGY OF RESEARCH

The experimental material selected for research was aluminium alloy powder labeled AlSi10Mg, mainly with higher content of Si and Mg. The content of elements is included in Table 1.

Table 1
AlSi10Mg alloy chemical composition

Element	Al	Si	Fe	Cu	Mn	Mg	Ni	Zn	Pb	Ti	Sn
Mass [%]	Balance	9-11	≤ 0.55	≤ 0.05	≤ 0.45	0.2-0.45	≤ 0.55	≤ 0.1	≤ 0.05	≤ 0.05	≤ 0.05

Source: (Data Sheet: AlSi10Mg)

A material was fused into the solid state using the SLM technology, by which 4 experimental specimens were prepared in Technical University in Ostrava (Czech Republic) - Center of 3D printing Protolab. The following Table 2 contains technological parameters which were set on the optimal values for reaching the best possible homogeneity of specimens.

Table 2
Technological parameters of SLM process

Parameter	Value
Laser power (*P*)	275 W
Scanning velocity (*v*)	1150 mm.s^{-1}
Hatching distance (*d*)	80 µm
Layer thickness (*t*)	30 µm
Scanning strategy	Chessboard (Fig. 1)
Gas protection	Argon (Ar)

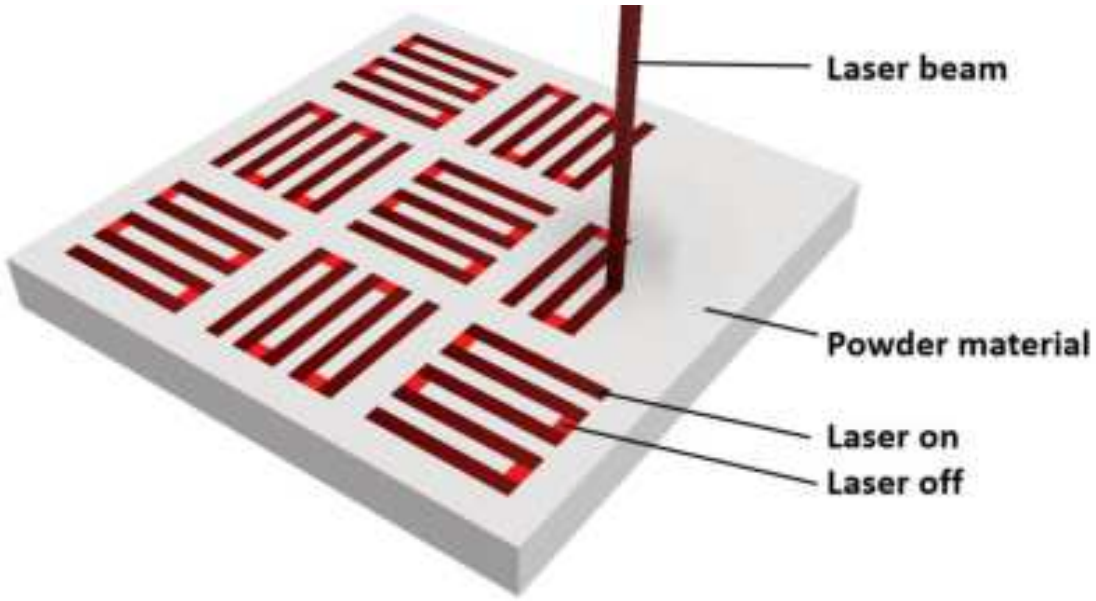

Fig. 1. Chessboard scanning strategy (Meander stripe and chessboard hatchings pattern)

The energy input (ε) of laser beam during the scanning process was calculated at the level of 99.64 J.mm^{-3}, according to equation (1) (Gu and Shen, 2009).

$$\varepsilon = \frac{P}{v \cdot d \cdot t} \tag{1}$$

Four experimental specimens were designed with artificial defects on their surface layer and in their subsurface layers (Fig. 2). Basic dimensions are 140 x 30 x 10 mm and designed artificial defects consist of notches, surface-reaching cavities and subsurface spherical cavities, representing cracks, pits and porosity. Identified surfaces of specimens were polished before the indetificaiton.

Fig. 2. NORTEC 600 device, OLYMPUS probe and experimental specimens

Designed artificial defects were measured using the eddy current testing device NORTEC 600 by the OLYMPUS company. A device interprets the presence of defects in the form of signal curves. IMPEDANCE (IMP) regime depicts signal curves as deviations on vertical (VMAX) and horizontal (HMAX) axis and the SWEEP (SWP) regime depicts signal deviations in the form of peaks on the vertical axis over the time. For better depiction of signal curves, GAIN function was used for the intensification of obtained signal on both axis and ANGLE function was used for the rotation of obtained signal (NORTEC 600 Eddy Current Flaw Detector User's Manual, 2022). OLYMPUS S/500HZ-40KHZ/.44 (11.2 mm in diameter) absolute probe with the frequency range of 0.5 – 40 kHz was used for the identification of artificial defects.

3. RESULTS

During the recent experiment (Geľatko et al., 2024), three probes were compared during the measurement of notch-type (5 mm deep) and hole-type (5 mm diameter) defects using 10 kHz which is their only mutual frequency. The identification was evaluated for both IMP and SWP regimes. During the measurement with P1 probe (0.3 – 10 kHz; 15.7 mm), higher deviation was reached on horizontal axis (4.7 HMAX) in the case of notch (grey curve), which influenced eddy currents in the greater extend. For the hole type defect (blue curve), signal variation is less significant. Its curve readability is better within the SWP regime, since at the IMP regime its shape is ambiguous and could be easily affected by noise signals during the real measurement in practice. Reasons of such negligible deviation are related to the properties of P1 probe, mainly in the form of its diameter, hence its gap in the center of coil is greater and eddy currents´ sensitivity is more suppressed in this area, what caused depression of middle peak within the signal curve almost to zero position. Another

consequence of probe diameter is possible edge effect that can suppress the sensitivity. The last factor is used excitation frequency, which is boundary within this probe, where attenuation of signal occurs.

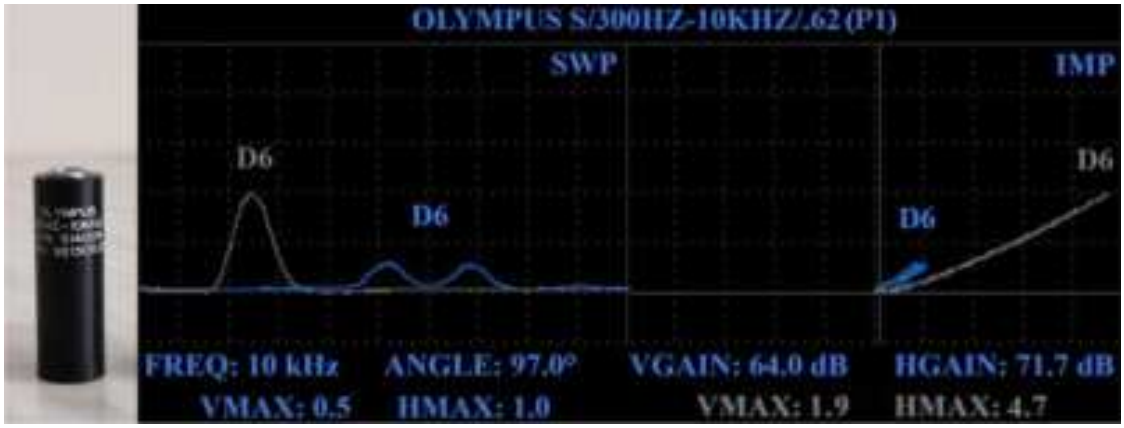

Fig. 3. ECT signal of P1 probe

A similar shape of curves was obtained using the P2 probe (0.5 – 40 kHz; 11.2 mm), similarly with the highest deviation on horizontal axis (4.9 HMAX) of the notch (Fig. 4). However, used frequency is from the middle of its frequency range, hence deviations are of greater value and signal curves have more characteristic and readable shape in both regimes. Also, the middle peak of the hole type defect does not reach zero position.

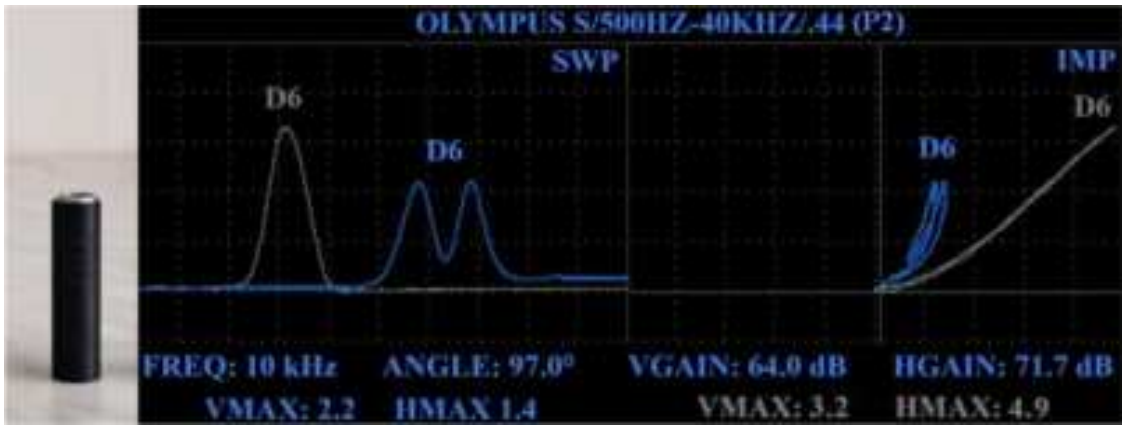

Fig. 4. ECT signal of P2 probe (used in this experiment)

In the case of P3 probe (10 – 100 kHz; 10 mm), higher deviation was present on vertical axis (3.9 VMAX) at notch type defect (Fig. 5). Shapes of curves are characteristic for individual defects, but the curve of notch type defect is steeper in the vertical direction and middle peak of hole type defect is in the half of its overall curve, which is caused by higher frequency range of the probe and hence its higher sensitivity.

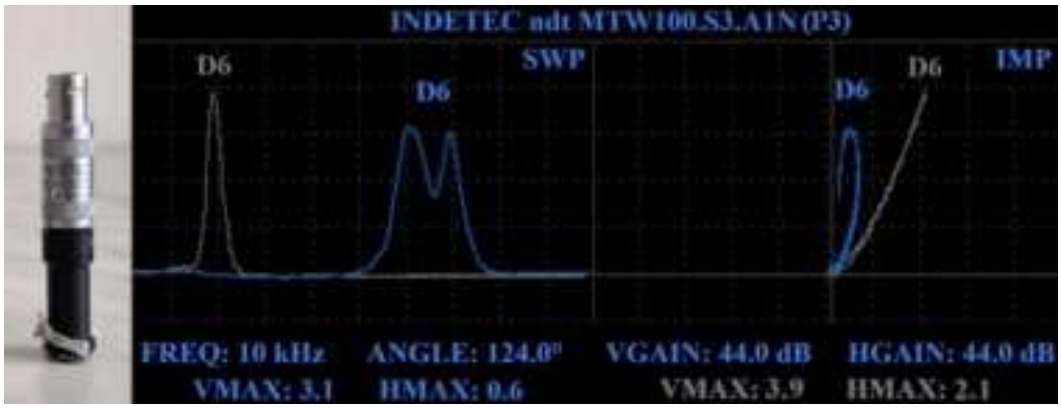

Fig. 5. ECT signal of P3 probe

Overall maximal deviation on vertical axis was reached at notch measured using P3 probe (3.9 VMAX) and overall maximal deviation on horizontal axis was reached at notch measured using P2 probe (4.9 HMAX). P2 probe showed to be suitable for the identification of surface reaching defects using higher frequency and also subsurface defects due to its ability of using the lower excitation frequencies. Within the first stage of the experiment, the sensitivity of the probe was evaluated through the construction of lift-off diagram (Fig. 6). It expresses the combination of signal deviation on vertical axis and horizontal axis as the response to the changes of lift-off distance, which represents the variation of distance between the probe and a measured surface in its whole frequency range. This variation was reached by the application of normalized plastic shims in the range of 0.15 – 1.2 mm. Obtained diagram of a typical lift-off shape is less balanced due to the lower deviations on vertical axis. Lower frequencies around 500 Hz express lower sensitivity, hence less significant measurement results can be predicted. Frequencies around 2.5 kHz and 5 kHz reached higher deviation on vertical axis (VMAX), which is more sensitive to material discontinuities, thus they can be suitable for the experiment.

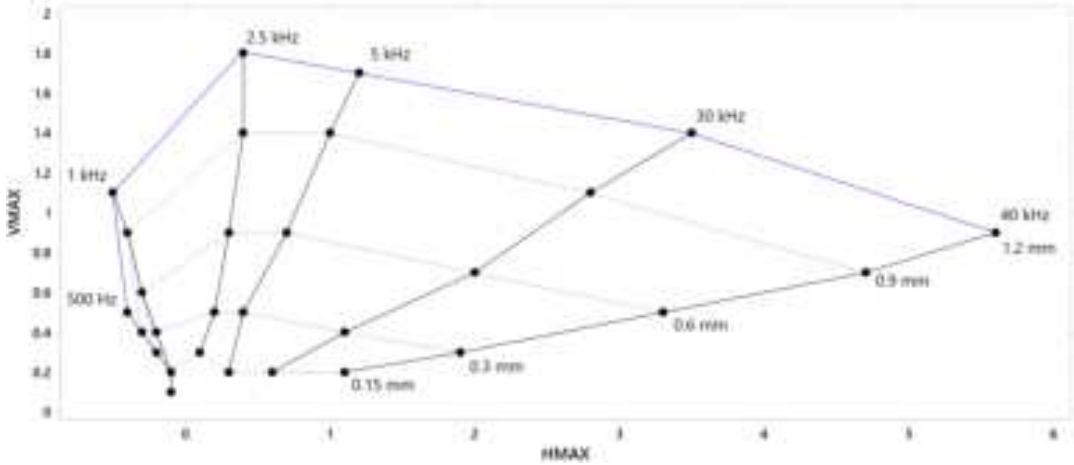

Fig. 6. Lift-off diagram of OLYMPUS S/500HZ-40KHZ/.44 probe

High frequencies are inclined to lower values of VMAX variation and vice versa to higher values of HMAX variation, which is more sensitive to lift-off distance changes (Fig. 6). However, they can be appropriate for the measurement of surface reaching defects, due to the lower penetration depth and their natural higher sensitivity. Following diagram (Fig. 7) includes standard penetration depth (δ) of eddy currents into the AlSi10Mg material at the frequency range of used probe, which is defined as a depth where eddy currents have 37% density considering the 100% density on the surface of a material, and at which the method can provide reliable measurement results. This parameter was calculated for selected frequencies according to equation (2) (García-Martín et al., 2011).

$$\delta = \sqrt{\frac{1}{\pi . f . \mu . \sigma}} \tag{2}$$

Where f is the excitation frequency, μ is the magnetic permeability and σ is the electrical conductivity. As aluminium based materials are considered non-magnetic, only σ parameter is important for calculation. The manufacturer of a material states its value in data sheet (Data Sheet: AlSi10Mg) at 37.76% IACS (International Annealed Copper Standard) and measured value during the recent experiment was 39.52% IACS. This difference can be considered as negligible after the calculation of δ. Based on a diagram (Fig. 7), the probe can penetrate into the depth around 0.5 mm at 40 kHz and up to maximal depth around 4.80 mm at 500 Hz frequency.

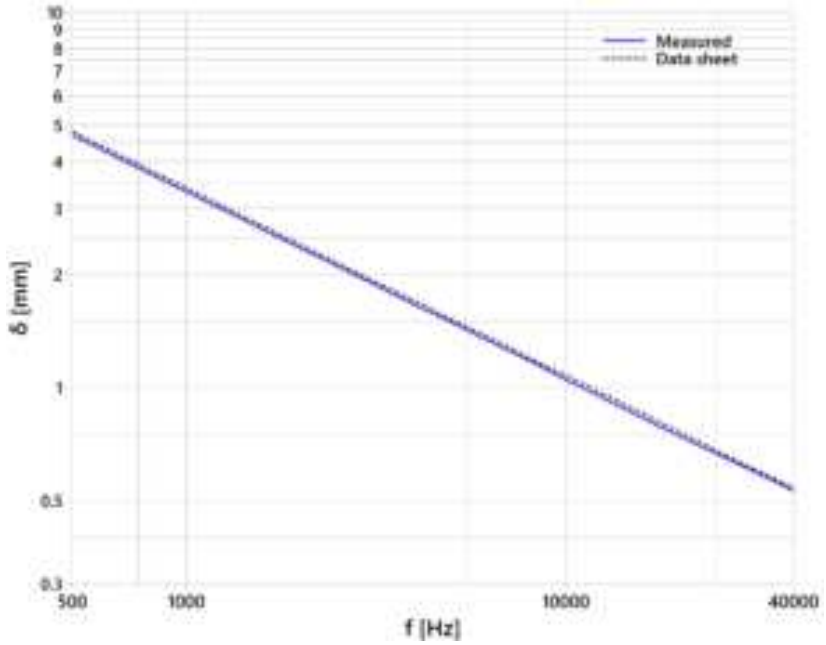

Fig. 7. Standard penetration depth diagram of OLYMPUS S/500HZ-40KHZ/.44 probe

Specimen 1 was designed with artificial defects on its surface. D1 defect is a notch of 0.2 mm width, 1 mm depth and length through the whole width of specimen. D2 is the same but situated at a 1 mm depth below the surface. D3 is rotated at 90° and 10 mm long. Defects D1-D3 were designed for the comparison of ECT signals according to various locations and orientations of notch-type defects, representing surface cracks. Defect D4 is a cluster of 0.5 mm deep holes and in 1 mm diameter, representing surface pits. The last D5 defect is a combination of D1 root with a sphere of 2 mm diameter in its middle, designed for the evaluation of dominant signal from notch-type and sphere-type defect representing the pore. All 5 artificial defects were measured at 30 kHz frequency with the same intensification of signal on both axis (VGAIN/HGAIN: 52 dB), 110° ANGLE rotation and the motion of probe in a longitudinal direction of specimen (axis of section in Fig. 8). The first notch (D1) caused typical signal deviation in the form of strong peak, due to its location on the measured surface. Its occurrence below the surface (D2) causes a strongly attenuated peak, as the consequence of the higher conductive material presence between the probe and a defect. The signal curve of D3 defect is a single-peak type. Its lower deviation can be ascribed to the less influence on the probe in the width axis direction. Reversibly, its wider shape within two lower thirds is the result of influencing the probe during the longer time through its motion along the axis of notch. The second phenomenon also pays for the D4 defect, which signal curve is similarly wider. Despite the fact that hole-type defects cause double-peak deviation curve, cluster showed the single-peak curve. The strongest deviation curve was observed in the case of D5 defect, where its overall shape was more influenced by the notch than the sphere.

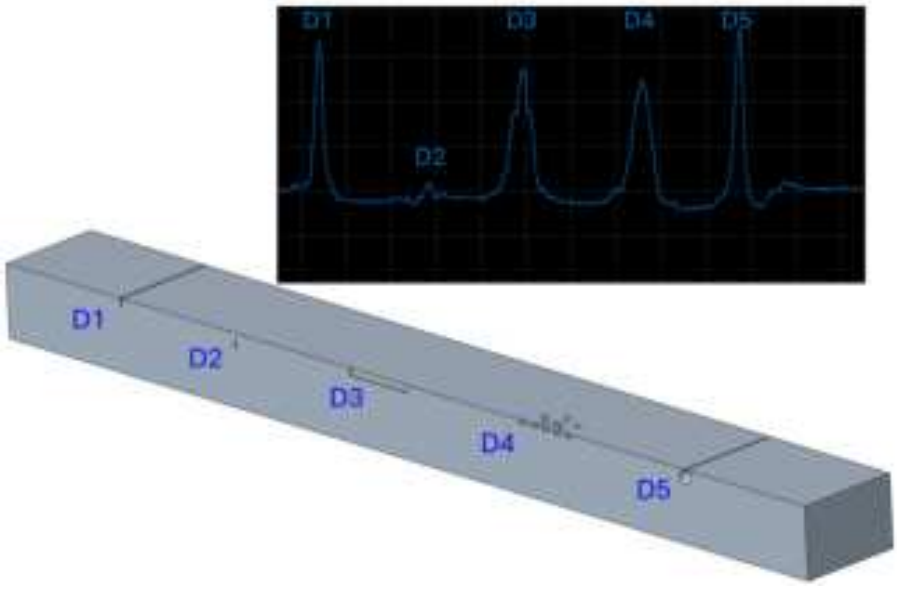

Fig. 8. Section of specimen 1 with surface defects and obtained ECT signal (SWP regime)

Similar characteristics of signal curves were obtained during the measurement using the IMP regime at the same parameters (Fig. 9). However, it is more difficult to distinguish signal of

differently oriented notch (D3) and holes cluster (D4) in comparison with SWP regime. IMP signal curves of all 5 defects are represented by the strong peak mainly in the vertical direction, which is characteristic for the notch-type defects. D4 defect curve includes a small bend in its middle, but it can be considered as negligible. Worth mentioning is the D2 defect which caused very weak deviation which can be easily lost in the noise signal during the measurement in real conditions.

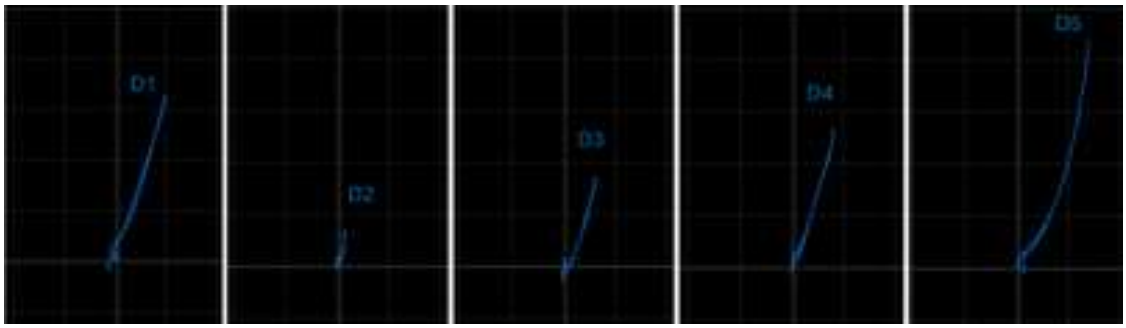

Fig. 9. ECT signal of defects in specimen 1 (IMP regime)

Specimen 2 included spherical cavities of 1 mm diameter which were composed of 4 artificial clusters (Fig. 10), representing pores filled by unmolten powder. Each cluster had its top cavity 1 below the surface. Clusters were designed with one cavity in the middle which was surrounded by cavities graded at 45° horizontal axis and their common pattering at 45° around the vertical axis. Distances between walls of cavities within clusters were various (D1 = 1 mm, D2 = 1.5 mm, D3 = 2 mm, D4 = 2.5 mm). Defects were measured using IMP regime at 2.5 kHz frequency, lift-off signal was rotated to the left bottom corner (30°), VGAIN and HGAIN were set on 85 dB and 66 dB, respectively. Reference signal was calibrated by placing the probe on the place without a defect and D1-D4 signals were obtained by placing the probe on areas above their location. The highest deviation was observed during the probing of D1 defect (-1.4 VMAX). With the increase of gaps between cavities, a signal variation decreases, whereas D3 and D4 clusters caused similar deviation around -1 VMAX. Predicted reason can be higher number of cavities within D1 cluster which influenced eddy currents. Higher gap between cavities causes their situation in deeper layers where eddy currents have no ability to reach them, hence lower number of cavities influence their density. Based on these signal characteristics, it can be stated that clusters were not probed in their full dimensions.

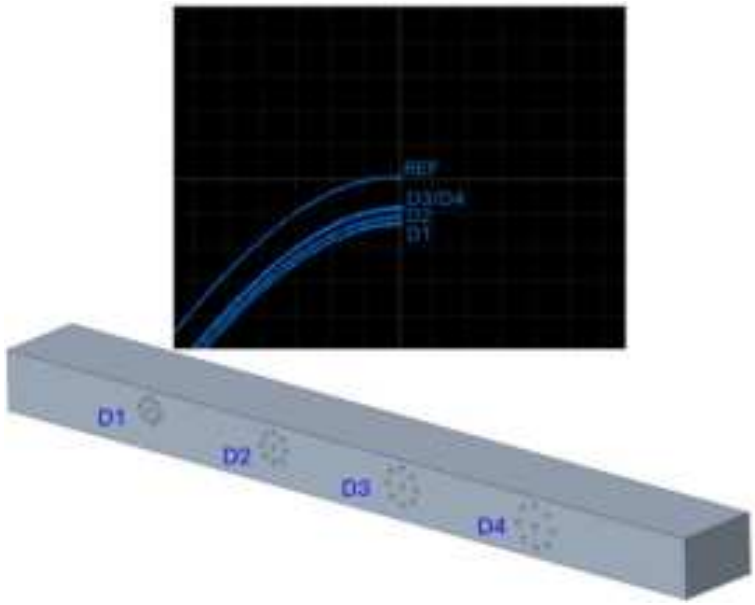

Fig. 10. Section of specimen 2 with subsurface defects and obtained ECT signal (IMP regime)

Specimen 3 was designed with similar 1 mm cavities with the top of clusters 1 mm below the surface (Fig. 11). D1 cluster included one central cavity surrounded by 4 cavities at 90° around horizontal axis and their common patterning around vertical axis at 90°, with the mutual distance of walls at 1 mm. D2 cluster included more cavities with pattering at 45° in both axis. In the case of D3 cluster, D1 layout was extended by another one cavity in all directions, with mutual distance of 0.5 mm. D4 cluster represents extended D2 cluster by another one cavity in all directions, with mutual distance of 0.5 mm. Parameters of a measurement and the strategy of a measurement were set based on the evaluation of specimen 2. The highest deviation was reached during the probing of D2 defect (-1.4 VMAX), similarly to the same D1 defect in specimen 2. Despite the fact that D1 and D3 clusters include lower number of cavities in comparison with the D2 cluster, their signal curves reached a lower but similar deviation. The lowest deviation was observed during the measurement of D4 defect, and the reason can be the complicated layout of clusters which partly overlap each other, and technology fused this area of material in a different way than was designed.

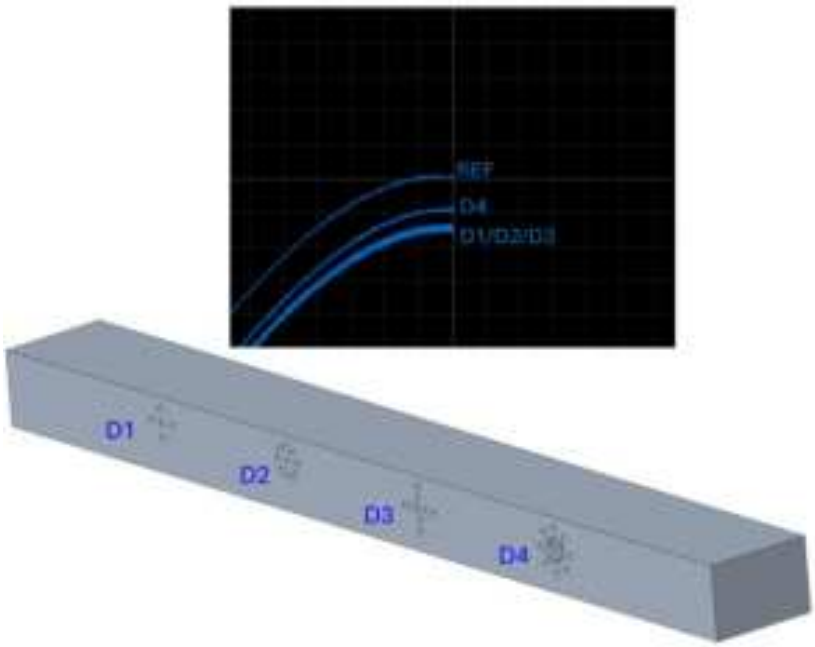

Fig. 11. Section of specimen 3 with subsurface defects and obtained ECT signal (IMP regime)

Specimen 4 was designed with subsurface spherical artificial defects of 1 mm diameter with 1 mm distance which were connected to the clusters, representing the porosity clusters fulfilled by unmolten powder (Fig. 12). Clusters were composed of one sphere in their bottom with gradual increasing of their number in the direction of surface using the rotational pattern around the middle axis of cluster. Measuring parameters and strategy were the same as in the case of specimen 2. It is evident that increasing of cluster size increased the signal deviation, with the maximum reached in the case of D4 (2.3 VMAX). This phenomenon confirms the statement that higher content of unmolten powder in subsurface layer causes higher ECT signal variation. A deviation inclines to positive values, which can be predicted as the consequence of higher unmolten powder content right below the surface in the case of all four clusters.

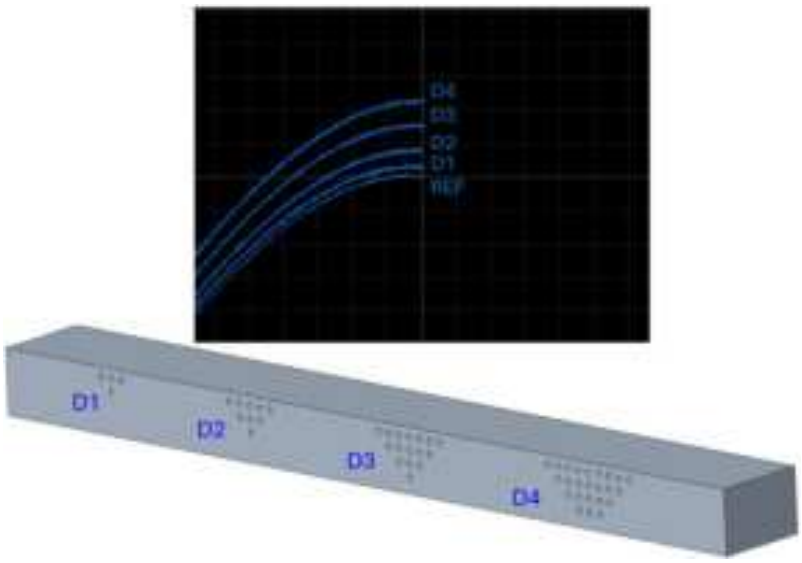

Fig. 12. Section of specimen 4 with subsurface defects and obtained ECT signal (IMP regime)

4. DISCUSSION

In a follow-up to the previous experiments and findings in other studies from the field, certain similarities and differences can be stated. Notch-type defect on the surface causes strong single-peak signal curve (Geľatko et al., 2022) in both regimes (SWP and IMP), however its presence below the surface of AlSi10Mg alloy causes significant attenuation of obtained signal, what is the consequence of more difficult identification of subsurface defects in such higher conductive material (Geľatko et al., 2024) The change of its orientation at 90° causes widening of curve within SWP regime. Despite that hole-type defect causes double-peak curve (E. Farag et al., 2022) within SWP regime, cluster of pits on the surface depicts wide single-peak curve. A single spherical cavity can increase single-peak deviation of notch; however, the double-peak shape is not present. Furthermore, the defects mentioned are difficult to distinguish within the IMP regime. At appropriate setting within IMP regime, porosity clusters can be identified, where their mutual distance and number of individual cavities can influence the signal, but these parameters cannot be distinguished in detail according to obtained signal curves within the evaluated material. The phenomenon mentioned is related to the sensitivity of eddy currents to a different density of material (Spurek et al., 2022), which can include empty porosity and porosity fulfilled by unmolten powder. Moreover, SLM technology does not have to make complicated artificial defects in a precise shape, what can be seen in a figure of recent study (Du et al., 2018).

5. CONCLUSION

The presented experiment focuses on the eddy current testing of artificial defects in SLM aluminium alloy AlSi10Mg. Obtained signal deviations were evaluated based on different parameters of notch-type defects, surface blind holes and subsurface cavity clusters. Based on resulting data, certain conclusions can be drawn:

- Characteristics of signal curves obtained at probing surface hole-type and notch-type defects at 10 kHz were described for three different probes, where influence of various frequency range was interpreted.
- Lift-off diagram and standard penetration depth were depicted for selected probe and evaluated material.
- The SWP regime showed itself to be more suitable for distinguishing various more complicated surface-reaching defects.
- A complicated measurement of subsurface defects in AlSi10Mg alloy was confirmed.
- The IMP regime was confirmed as appropriate for identification of larger areas which included discontinuities in subsurface layers.
- The influence of various layouts of cavity clusters showed to have influence on obtained ECT signal.

Subsequent experiments within this complex research need to be focused on the evaluation of different densities of AM materials using ECT method and check depicted signal curves according to designed artificial defects on other AM materials and real induced defects.

ACKNOWLEDGEMENTS

This work was funded by grant 02/TUKE/2024. This work was funded by the Slovak Research and Development Agency under contract No. APVV-21-0228 and the projects VEGA 1/0391/22, KEGA 017TUKE-4/2023 were granted by the Ministry of Education, Science, Research and Sport of the Slovak Republic. Article is the result of the Project implementation: Development of excellent research capacities in the field of additive technologies for the Industry of the 21st century, ITMS: 313011BWN5, supported by the Operational Program Integrated Infrastructure funded by the ERDF.

REFERENCES

Data Sheet: AlSi10Mg. Center of 3D Printing Protolab.

Du, W., Bai, Q., Wang, Y., & Zhang, B. (2018). Eddy current detection of subsurface defects for additive/subtractive hybrid manufacturing. The International Journal of Advanced Manufacturing Technology, 95, 3185-3195.

Ehlers, H., Pelkner, M., & Thewes, R. (2020). Heterodyne eddy current testing using magnetoresistive sensors for additive manufacturing purposes. IEEE Sensors Journal, 20(11), 5793-5800.

E. Farag, H., Toyserkani, E., & Khamesee, M. B. (2022). Non-destructive testing using eddy current sensors for defect detection in additively manufactured titanium and stainless-steel parts. Sensors, 22(14), 5440.

García-Martín, J., Gómez-Gil, J., & Vázquez-Sánchez, E. (2011). Non-destructive techniques based on eddy current testing. Sensors, 11(3), 2525-2565.

Geľatko, M., Hatala, M., Botko, F., Vandžura, R., & Hajnyš, J. (2022). Eddy current testing of artificial defects in 316L stainless steel samples made by additive manufacturing technology. Materials, 15(19), 6783.

Geľatko, M., Hatala, M., Botko, F., Vandžura, R., & Hajnyš, J. (2024). Study of Eddy Current Testing Ability on SLM Aluminium Alloy. Materials, 17(14), 3568.

Gu, D., & Shen, Y. (2009). Balling phenomena in direct laser sintering of stainless steel powder: Metallurgical mechanisms and control methods. Materials & Design, 30(8), 2903-2910.

Guo, S., Ren, G., & Zhang, B. (2021). Subsurface defect evaluation of selective-laser-melted inconel 738LC alloy using eddy current testing for additive/subtractive hybrid manufacturing. Chinese Journal of Mechanical Engineering, 34, 1-16.

Meander stripe and chessboard hatchings pattern. Renishaw Official Website. [online] Available at: https://www.renishaw.com/resourcecentre/en/details/Meander-stripe-and-chessboard-hatchings-pattern--95492?lang=en [Accessed 26 Oct. 2024].

NORTEC 600 Eddy Current Flaw Detector User's Manual, (2022). Evident Official website. [online]: https://www.olympus-ims.com/en/downloads/detail/?0[downloads][id]=276825861 [Accessed 26 Oct. 2024].

Spurek, M. A., Spierings, A. B., Lany, M., Revaz, B., Santi, G., Wicht, J., & Wegener, K. (2022). In-situ monitoring of powder bed fusion of metals using eddy current testing. Additive Manufacturing, 60, 103259.

.

THE PROCESS OF MEASURING AND EVALUATING SELECTED ELECTRON BEAM PARAMETERS

Ing. Ľuboš Kováč[1]
Ing. Daniel Dřímal, PhD.[2]
Ing. Tomáš Fodrek[3]
[1]ORCID: 0000-0003-4308-805X, PRVÁ ZVÁRAČSKÁ, a. s., Slovak Republic
[2]ORCID: 0000-0003-2311-6228, PRVÁ ZVÁRAČSKÁ, a. s., Slovak Republic
[3]ORCID: 0000-0001-6534-8321, PRVÁ ZVÁRAČSKÁ, a. s., Slovak Republic

Abstract:
Knowledge of the emission system condition and the time profile of the pulsed welding current during electron beam mass welding is a key requirement for ensuring reliable operation of the welding complex and minimizing failures due to insufficient electron beam quality. During use, the cathode gradually wears out at high temperatures to the point where the emitted electron beam is of insufficient quality to achieve the required weld quality. In order to control and assess the quality of the emission system the measurement apparatus was developed to measure the transverse profile of the energy distribution in the electron beam. A method based on the sensing the time course of the beam current as it passes through the measuring slit was used. The time waveform of the electron current captured by the Faraday measuring electrode placed under the slit is passed through the protection and signal adaption module to the DAQ module, where it is digitized and transferred to a PC. The software tool runs there to record and evaluate the captured waveforms. An example of the deployment of a measurement setup on a batch welding machine is described in the presented paper. The quality of the measured electron beam is assessed on the basis of the characteristic parameters of the computed approximation to the ideal Gaussian distribution, the standard deviation and the mean value of this approximation. The mean value μ corresponds to the position of the maximum of the approximation. The difference between the mean value of the approximation and the position of the maximum of the measured signal indicates the symmetry of the beam. The value of the standard deviation σ of the calculated approximation indicates the slenderness of the whole profile. The smaller σ is, the narrower and steeper the section of the beam profile is. The extent to how closely the measured electron beam profile matches the ideal shape is expressed by the deviation of the measured signal from the Gaussian approximation. A larger deviation means a more deformed beam.
Keywords: electron beam, welding, beam profile, emission cathode

1. INTRODUCTION

The electron beam welding process is widely used in various industries, including aerospace and automotive, especially when high demands are placed on the quality and integrity of the

welded joints. The advantage of electron beam welding is the ability to efficiently control the energy concentration over a very wide range. The electron beam can be used as a very soft heat source to heat the material (low areal energy density in the beam) by defocusing and dynamic deflection without significant loss of energy transfer to the material, unlike a laser beam (reflectivity problems). By contrast, the electron beam allows to achieve very high areal energy densities in the beam (at the level of 10^7-10^8 W.cm^{-2}). This makes it possible to produce narrow and deep welds with low thermal effect of welded materials. Therefore, this method is highly effective for welding metallic materials with high melting temperatures, metals or alloys with problematic weldability, thick or, on the contrary, thin and subtle parts. Welding is usually carried out in a high vacuum environment (10^{-2} Pa), which virtually eliminates oxidation of the weld metal in the process. The vacuum also promotes degassing of the fusion bath.

One of the key components of the electron beam welding complex is the emission cathode. It serves as a source of electrons, which are subsequently accelerated by an electrostatic field and focused on the surface of the material, and eventually statically or dynamically deflected. Materials such as W, Ta, LaB_6, thorium oxides, or other materials with low output work energy that are capable of thermal emission of electrons are used as materials for emission cathodes. An important requirement is that the emission temperature is lower than the melting temperature of the cathode material. Thus, the cathode plays a critical role in the generation of the electron beam and determines its characteristics such as current intensity, beam geometry, energy distribution and stability. The application of LaB_6 cathodes is supported by the good emissivity at relatively low temperatures (1 700 K). In the case of W cathodes, a higher temperature (2 000 K) is required to achieve thermal electron emission.
At the beginning of the lifetime, the emissivity of the LaB_6 cathode is high, the material and surface of the cathode is undamaged, and it exhibits low electron output work at relatively low temperatures. The emission currents are stable and uniform and therefore the energy distribution of the electron beam from the LaB_6 cathode is homogeneous, symmetrical, typically with a Gaussian distribution of energy in the beam (ideal for precision applications such as welding).

Over time, cathode wear occurs, mainly due to contamination, diffusion of material on the cathode surface and evaporation of La at high temperatures. There is a decrease in emissivity (the cathode temperature has to be increased to achieve the same emissivity). Inhomogeneity in electron emission may also occur. As a result of inhomogeneous emission from different parts of the cathode surface, the beam may become asymmetric, which can lead to a deterioration in the focusing quality of the beam.

In the final stage, the emissivity decreases, the cathode reaches the end of its lifetime and the beam profile is significantly deformed. The cathode surface is severely damaged (cracks, contamination, erosion), which reduces the effective electron emission area. At this stage, it

is difficult to control the energy distribution, which leads to a reduction in the accuracy and quality of welding or other operations. Increasing the temperature of the emission cathode may no longer be sufficient to achieve the desired welding current.

Degradation processes lead to a gradual deterioration of the emission capability, which can have a negative effect on the total number of emitted electrons, the homogeneity of the energy distribution in the beam and the overall stability of the system. Therefore, the condition of the emission cathode directly affects the quality of the electron beam and thus the entire welding process and can lead to defects formation. Higher operating temperatures of cathodes accelerate their degradation. Dimensional changes due to dilatation, faster diffusion of atoms and intense evaporation increase. The deteriorated vacuum level in the electron gun also leads to damage of the cathode surface.

The pressure increase in the electron gun is usually caused by welding contaminated material (grease, corrosion, etc.) or by welding material containing elements with high vapors pressure (Zn, Mg, ...). Similarly, a large melt pool area, e.g. in surface reflow welding, intensifies the evaporation of the processed material and can lead to an increase of the pressure in the electron gun and contamination of the emission cathode. The different types of LaB_6 cathode damage are illustrated in fig. 1.

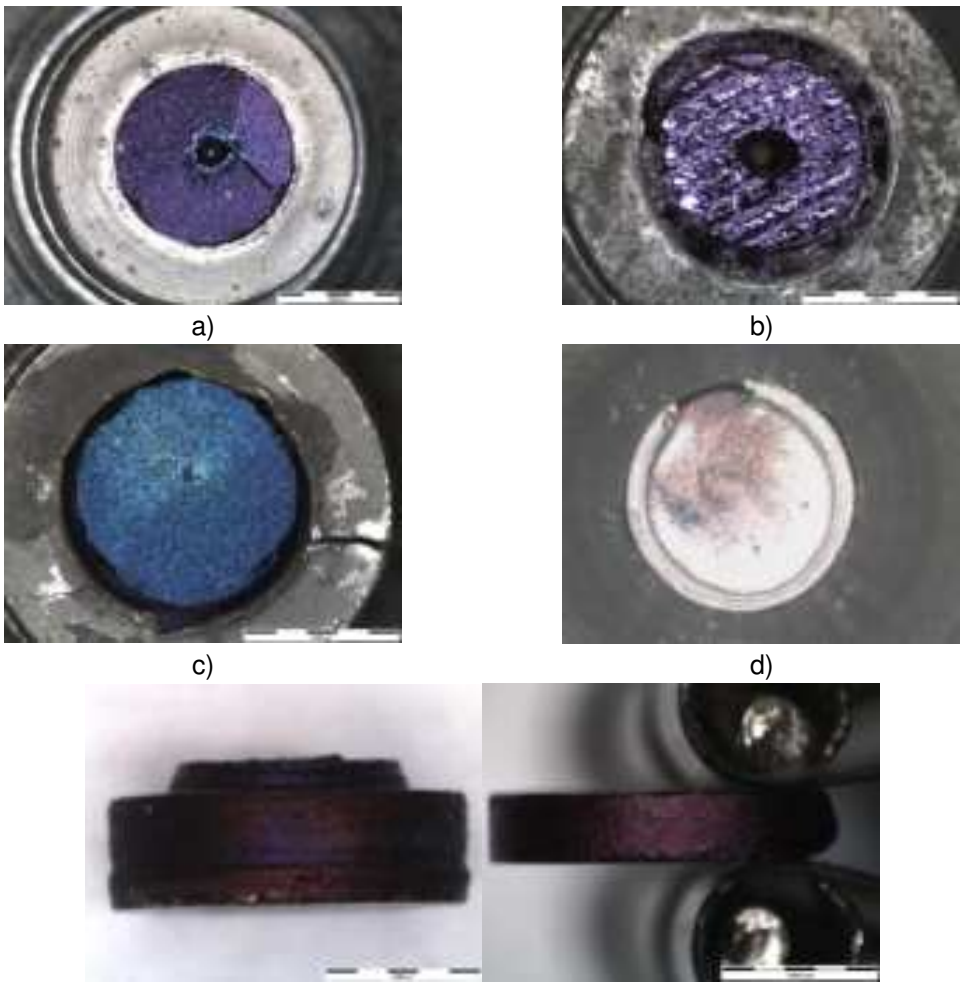

Fig. 1 Examples of LaB_6 emission cathode damage
a) mechanical damage due to extreme thermal stress (cracking, chipping), b) erosion by positive ions from the welding process, c) contamination by light atomic elements, d) contamination by metal vapors, e) evaporation of the cathode material.

There are several methods for the assessment of the cathode condition, and one of the most widely used and effective being the measurement of the energy distribution in the electron beam. Various methods can be used to make this measurement. One of the most widely used is based on the measurement of the electron beam or the assessment of the energy distribution in the electron beam using a Faraday probe with a linear slit or a small aperture. The measurement itself generally consists of measuring the total current or a portion of the current of the electron beam. A measuring probe (Faraday cylinder) with a slit allows the measurement of the transverse profile of the electron beam. The slit is adjustable and consists of tungsten parts for high temperature resistance and increased durability. The width of the measuring slit is adjustable to meet the basic assumption - the width of the slit must be

smaller than the diameter of the electron beam to be measured. The narrower slit can measure a more accurate image of the actual electron beam profile, but at the same time the current signal obtained is lower in intensity and significantly more sensitive to interference. To eliminate the influence of the thickness of the linear aperture, bevels are formed on the prisms at the measuring area. A Faraday probe collection electrode is placed below the linear slit to capture the electron current passing through the slit. This current is further routed through a measuring resistor and subsequently processed as an analog voltage signal. In order to increase the absorption of the passing electrons by the collecting electrode, the surface at the impact point is electron-machined so that the angle of incidence is not perpendicular, but any reflections take place inside the Faraday probe. The collecting electrode is electrically isolated from the entire structure of the measuring probe by insulating pads.

2. THE MEASUREMENT PROCESS OF AN ELECTRON BEAM TRANSVERSE PROFILE WITH THE CHANGE OF THE FOCUSING CURRENT AS A VARIABLE BEAM PARAMETER ON THE EXPERIMENTAL TECHNOLOGICAL COMPLEX PZ ELZA UNI

Measurements were made using a Faraday probe with a slit aperture. The width of the linear slit was set to 0.1 mm. The measurement probe was positioned so that the slit was aligned with the undeflected electron beam, the working distance was 525 mm.

On the deflection generator, a linearly rising or falling "Ramp" waveform with an amplitude of $10V_{PP}$ and a total pulse time of 2 ms (frequency 500 Hz) was set for the adjacent channel, perpendicular to the measurement slit. The corresponding deflection of the electron beam from one extreme position to the other at a working distance of 525 mm was approximately 50 mm, which the beam traversed in a time of 1 ms. The division of the power exciter deflection coil input circuit was set to a division of 1:2. The generator was switched to "Burst" mode with a limited number of cycles performed per run "NCycle" with a value of "Cycle=1". In order to keep the beam in the extreme deflection position in the idle state, the triggering phase was set to "Phase=90°". In order to synchronize the triggering of the recording of the measurement by the DAQ module PicoScope 3204D, the synchronization pulse generation parameter "Trig Out" was set on the generator with a leading edge at the beginning "Leading", a delay ""Delay=0" and an unwanted automatic repetition after "Period=500s". The electrical TTL sync signal was routed from the BNC connector of the "Sync" generator of the respective channel via a coaxial cable to the DAQ module to the external trigger input of the oscilloscope "Ext - External trigger". The trigger mode of the generator has been selected "Manual", in which the deflection can be started manually by pressing the "Trigger" button or by an external command received via the Ethernet communication interface from the master control computer of the welding workstation.

The deflection generator control is fully integrated into the control system of the experimental electron beam complex PZ ELZA UNI as well as into the single purpose mass production electron beam welding workstations for welding die-cast aluminum alloy castings for the automotive industry. The commands specified for the generator can be used to set and control all the most commonly used functions and, at the same time, any command supported by the DAQ module itself (PC oscilloscope) can be entered using the "SCPI" commands.

The technological program for the control of the measurement process is specified in the welding operator control program (fig. 2). The program can guide the measuring Faraday probe to the working position or is started with a preset position. In the example of the program, the positioning table with the probe is pre-set to the working position. The power supply is switched on with the electron gun is opened and started. The focusing current is set to approximately focus on the surface of the measuring slot at the selected accelerating voltage.

Fig. 2 Example of a technology program for the measurement process control

The initial commands (ID0 and ID1) perform the on/off switching of the used channel of the deflection generator with respect to the orientation of the measurement slit. The following command is the time setting required for the generator to process the previous commands (ID2). The command in line ID3 switches on the electron beam to the value of the chosen welding current according to the value defined by parameter ID0 (in this case Iz = 40 mA). The focusing current will be changed during the entire process segment, up to line ID7, from the initial set value 855 mA + DIfStart = 40 mA to the values 855 mA + DIfEnd = DIf, the initialization value for DIf is set to -10 mA. The hold on line ID4 is used to stabilize an electron beam. Line ID5 is used as a "Repeat" flag when executing a program loop. Line ID6 contains the time to process the previous command (to be used in the loop). Line ID7 sets the beam parameters to the updated parameters (recalculated DIf, to be used in the loop). Time (ID8) to process the previous command. Line ID9 is to start one deflection cycle with the "Trigger" command. Again, the time to process the command. On line ID 11, the increment Step=2 is added to the DIf variable. From line ID 12, the program executes the "Repeat" command to jump to the "Repeat" instruction on line ID 5. The number of programs passes with the "Repeat" statement is 11. In the repeat loop, the focal current changes by

the 2 mA "Step" value defined in parameter ID3 and the DAQ module starts recording the measurement. Subsequently, after the last loop pass on line ID 13, the welding current is switched off to Iz=0 and the program is terminated with a final pause for a clearer termination of the archiving of the welding parameters. The whole measurement progress is recorded in the parameter archives and it is possible to trace the switching on, stabilization and holding of the welding current Iz as well as the stepwise change of the focusing current If, see fig. 3.

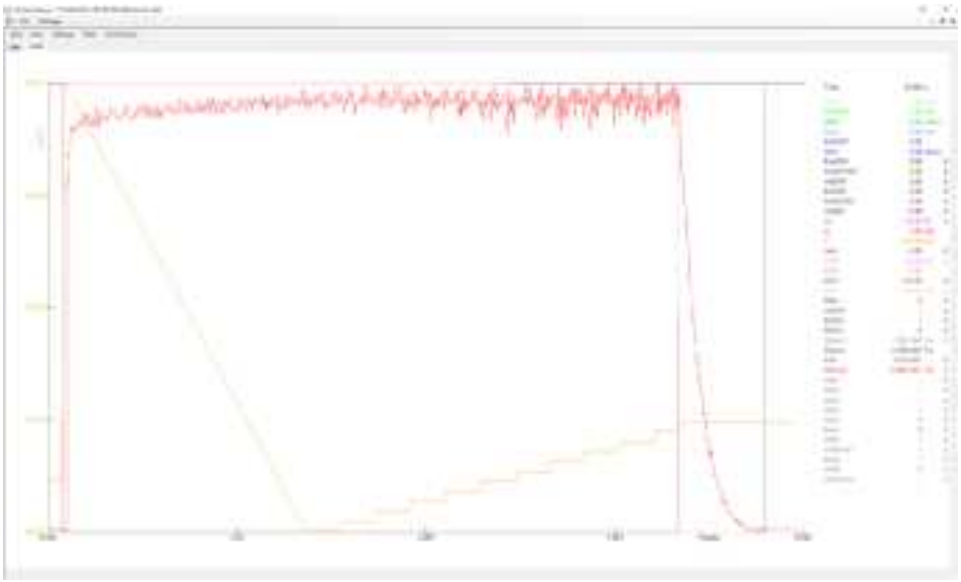

Fig. 3 Recorded measurement progress

During signal generation for the deflection system, a synchronization pulse is also generated for recording the measured signal by the DAQ module. The leading edge of the synchronization signal that triggers the measurement of the DAQ module is generated right at the beginning of the deflection. Of the total beam travel time from one edge position to the other (1 ms), only the time period during which the electron beam passes over the measurement slit is relevant, i.e. approximately 50 to 150 µs. This needs to be taken into account by the delayed start of the high sampling rate analogue waveform recording with respect to the synchronization pulse from the deflection generator. This reduces the amount of data to be captured, transferred, recorded and processed.

The "Beam Analysis" software system for measurement of selected electron beam characteristics is used to set the measurement parameters of the DAQ module (PC oscilloscope PicoScope 3204D), transfer the data, subsequent processing, display in the form of a time-dependent graph and evaluation of the characteristics of the acquired waveforms.

Before the measurement is started, it is necessary to set several parameters of the DAQ module. For the measurement, the range of the input used was set to ±5 V and the Offset was set to 5 V. Using a DC offset of half the range in the oscilloscope input circuits allows to increase the sensitivity of the voltage input of the A/D converter since the input range is always symmetrical and the measured signal is strictly negative. To simplify the illustration, the input negative signal is inverted to obtain a positive waveform. The measurement trigger "Trigger" has been set to "Mode: Auto" on the leading edge "Direction: Rising" of the external sync input "Chanel: External" at the value "Voltage:1 V". Recording delay after trigger "Delay:460 µs". Selected time base "Time Base:10 µs" at "Number of waveforms in the chart:1" recording length 100 µs. With the selected sampling period "Sample period:16" we obtain 6250 recording samples, which is a suitable number both for achieving sufficient sensitivity and a reasonable volume of data for transmission, processing and storage.

The DAQ module configured is ready to capture, transfer and process the data that will be measured after starting the measurement procedure from the technological computer of the welding workplace. Once the technology program is started, the electron beam is repeatedly passed over the measuring slit of the Faraday probe and the measured data are captured, transferred and displayed on the screen of the portable PC ready for further analysis.

3. STANDARD DEVIATION AS AN ASSESSMENT PARAMETER OF ELECTRON BEAM QUALITY

The energy density of the electron beam generated in an electron gun with an undirected LaB_6 cathode of circular shape is not uniform, but corresponds to a Gaussian distribution. The energy or electron current profile is highest in the center and decreases towards the edges. Knowledge of the actual energy density allows the assessment of the suitability of the thermoemission system for welding with a regard to ensure the desired weld quality with the required weld penetration. In high cadence welding, during the lifetime of the emission system, the LaB_6 cathode is degraded on its surface and possibly also in its volume due to its gradual evaporation, erosion by bombardment with positively charged particles, mechanical damage, contamination by atoms impairing the emission capability (poisoning) and its overheating. Early detection of beam quality deterioration and thus the potential reduction in weld performance is important to maintain quality production and the overall economics of the welding process. Since the ideal electron beam energy density profile has the shape of a Gaussian distribution, parameters that assess the average and degree of similarity of the beam under consideration to the ideal Gaussian distribution were chosen to determine the evaluation parameters of the electron beam.

In order to suppress the influence of the industrial environment interference on the acquired waveforms, a 1st order input filter with two-step filtering with adjustable amplitude threshold is applied in the software. Subsequently, the calculation module of the program calculates an

approximation of the measured signal in the form of an ideal Gaussian curve, where the maximum value of the approximated curve corresponds to the maximum value of the measured waveform. The result of the approximation calculation is the standard deviation σ and the mean value, which explicitly characterize the equation of the Gaussian curve (fig. 4 and 5).

Whereby the mean value μ corresponds to the position of the maximum of the approximation. The difference between the mean value of the approximation and the position of the maximum of the measured signal describes the symmetry of the beam. For a symmetric beam, they are identical. In the case of distorted asymmetric profiles, the mean value of the approximation shifts further from the position of the maximum of the measured waveform.

The value of the standard deviation σ of the approximation computed provides an indication of the thinness of the whole profile. The smaller σ is, the narrower and steeper the profile of the beam is. Approximately 68% of the values (power) are in the interval $\mu \pm \sigma$, 95% of the values are in the interval $\mu \pm 2\sigma$, and 99.7% are in the interval $\mu \pm 3\sigma$.

Another parameter calculated is the deviation of the measured signal from the Gaussian approximation. The value reflects the degree of matching of the measured shape to the ideal shape. A larger deviation means a more distorted beam.

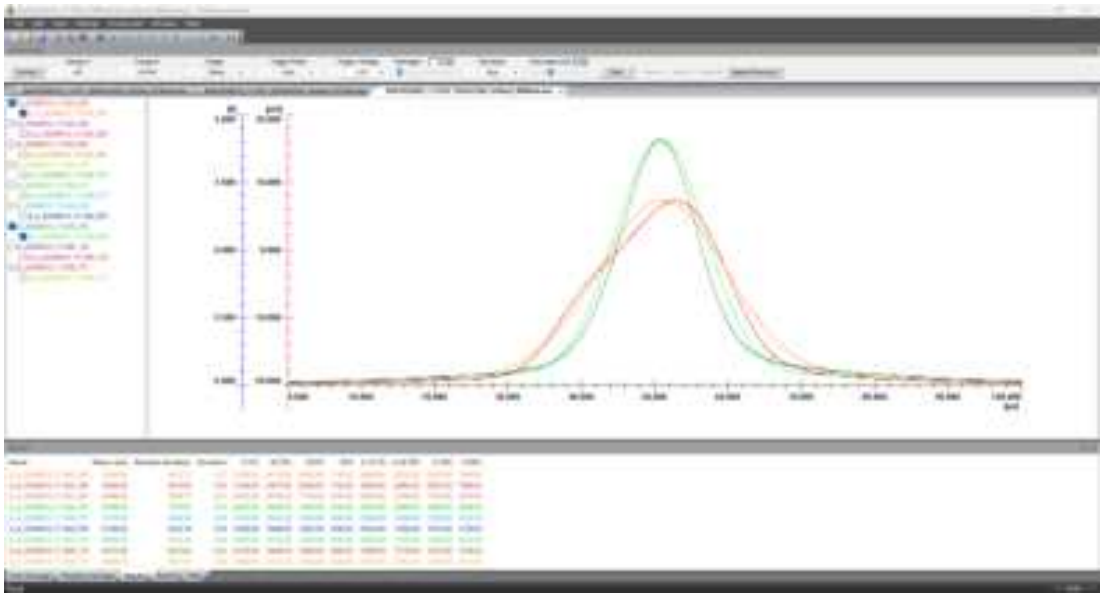

Fig. 4 Program window with recorded waveforms

Fig. 5 Calculated parameters of the waveforms and their approximations

4. CONCLUSION

The standard deviation seems to be a suitable description of the energy distribution for the assessment of electron beam. This assessment parameter is suitable for assessing the quality of the electron beam and also has a meaningful value about the state of the emission cathode, as it describes the "slenderness" of the electron beam. It is the slenderness (beam width relative to the maximum value) that reflects the concentration of energy in the electron beam, concentrated mainly around the beam axis, and responsible for the ability of the beam to penetrate the material. The choice of standard deviation as an assessment parameter of beam quality has been confirmed as very appropriate in the view of both theoretical considerations and experiments performed so far.

The second chosen evaluation parameter of beam quality is the deviation, which is defined as the difference between the actual beam profile and the calculated approximation to the ideal Gaussian waveform. This expresses the degree of local disturbances in the beam energy distribution, as a consequence of which it may be difficult to focus the electron beam to the desired extent. As a consequence, the penetration capability of the electron beam is deteriorated, there is a problem with the stability of the vapor's gas channel, which can lead to increased pore formation in the weld metal and a decrease in the weld depth.

The functionality of the measuring apparatus and the chosen solution has been successfully tested in operation on electron-beam technological complexes.

ACKNOWLEDGEMENTS

This work was supported by the Slovak Research and Development Agency under the contract No. APVV-20-0103.

REFERENCES

Aman P. Kaur: Electron Beam Diagnosis for Weld Quality Assurance, Department of Electronic and Computer Engineering, College of Engineering, Design and Physical Sciences, Brunel University London, 2016.

AWS C7 Committee on High Energy Beam Welding and Cutting: Recommended Practices for Electron Beam Welding, 4th Edition, American Welding Society, 2013.
ISO EN 14744-2018 1 až 3, Zváranie – Akceptačné skúšky zariadení na zváranie elektrónovým lúčom, 2000.
Kaur A., Ribton C., Balachandran W.: Development of a novel device and analysis method for characterizing electron beams for welding applications, Proceedings 12th International Conference on Electron Beam Technologies, ELEKTROTECHNICA & EL-EKTRONICA E+E, Vol. 51. No 5-6/2016, p. 170, ISSN 0861-4717.
Kovac L., Drimal D., Mastalir P.: Technické riešenie systému monitorovania vybraných parametrov elektrónového lúča pre procesy vysokokadenčného zvárania, ZVÁRAČ č. 3, ročník XX, 2023, ISSN 1336-5045, s. 3-6.
Liebig C., Fath J., Löwer T.: Electron beam characterizing and its relevance for pro-duction, Proceedings 12th International Conference on Electron Beam Technologies, EL-EKTROTECHNICA & ELEKTRONICA E+E, Vol. 51. No 5-6/2016, p. 166, ISSN 0861-4717.
Schultz H: Electron beam welding, Cambridge, Abington-publishing, ISBN 3 87155 111 2, 1994.
Zobač M.: Řízení a diagnostika elektronového svazku pro pokročilé technologie, Dizertační práce, Ústav fyzikálního inženýrství, Fakulta strojního inženýrství, VUT Brno, 2009.

WELDING REQUIREMENTS HETEROGENEOUS WELDED JOINTS OF MATERIALS HIGH-STRENGTH STEEL HARDOX 500 AND ASUTENITE STEEL 08CH18N10T FOR NUCLEAR POWER PLANT

Ing. Jiří Macháček[*]
doc. Ing. Marta Kianicová, PhD[*]
Ing. Ingrid Kovaříková, PhD[*]**.**
[*] Alexander Dubček University of Trenčín, Faculty of Special Technology

Abstract:
Within the framework of the project of welding a heterogeneous welded joint of high-strength steel HARDOX 500 and austenitic steel used in the primary circuit of nuclear power plants 08CH18N10T, the weldability of these steels will be tested, including verification of the welded joint and HAZ. Two welding methods will be compared from the point of view of sample preparation. The first samples will be made with an austenitic weld on the HARDOX 500 material to reduce internal stress in the welded joint. The second samples will be made without an austenitic weld, therefore regardless of the stress created in the welded joint. The results will be compared and evaluated to determine whether these materials can be welded and which method is more suitable for them. Based on the results of the chemical and structural composition of the welded joint and the comparison of mechanical properties, a comparison will be made with the results of materials currently used in the design and construction of new nuclear units.

Keywords: welding requirements, austenite, high-strength steel, material testing, heterogeneous weld joint

1. INTRODUCTION

Requirements for welding high-strength steels in our case HARDOX 500 and austenite used in nuclear power plants 08CH18N10T.
Each of these steels has completely different welding requirements, due to their composition, structure and mechanical properties. In the project of welding high-strength steels and austenitic steels for nuclear power plants (Fig. 1), we want to demonstrate the usability of high-strength steels within the scope of the applicability of these steels in order to increase the safety of pressure vessels of high-pressure water reactors.
Welding of these steels will be carried out using the TIG method in a protective atmosphere with inert gas (argon). This welding method is suitable for both tested materials.
Furthermore, a design of individual tests is made for testing to verify the chemical and mechanical properties of the weld joint, as well as HAZ.

There is currently not much experience in welding high-strength steels with austenitic steels. We currently know that heterogeneous welds with austenitic and duplex steels can be made in high-strength steels. However, we have no experience with welds that are subject to such demanding requirements as those imposed by nuclear technology and legislation.

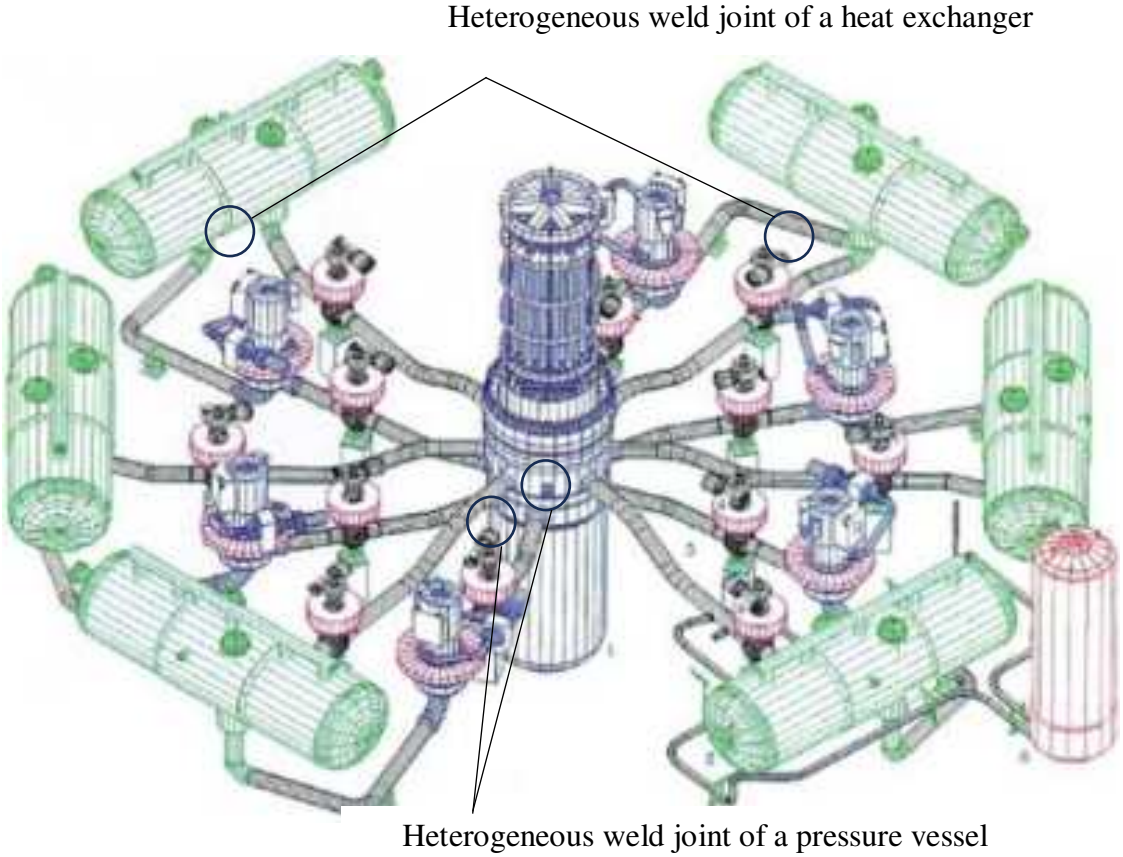

Fig. 1 primary circuit diagram of a nuclear power plant

2. PRINCIPLES FOR WELDING HTG WELDS

The requirements for welding HTG welds within the pressure system of the primary circuit of nuclear power plants are governed by specific procedures given by the project. The permitted welding methods are TIG methods, manual arc welding, a combination of these two methods and automatic submerged arc welding using filler materials.

Before welding parts made of austenitic stainless steels with parts made of non-self-hardening steels with a carbon content of up to 0.3 wt%, pearlitic steels with a wall thickness of more than 10 mm, a single-layer weld must be applied to the weld surfaces of pearlitic steels in advance, with a total thickness after machining of 5±1 mm.

The weld on HARDOX steel is performed due to the change of compressive stress to tensile stress. This will reduce the stress in the weld joint and thus prevent the formation of cracks in the weld. Also, a heterogeneous weld is made by the weld overlay and the subsequent welding with austenitic steel is performed as a homogeneous weld joint (Fig. 2).

Fig. 2 Weld scheme of transitional weld

Within the project, weld joints are also made without this weld overlay and the results of the individual weld joints will be compared. On the picture (Fig. 3) you can see the different structure of the grains of the individual materials.

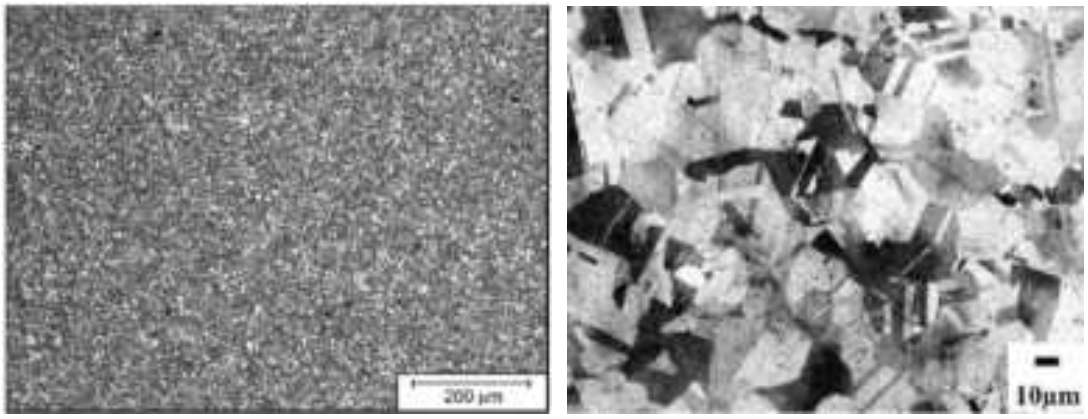

Fig. 3 Comparison of the structure of the materials used from the left: High-strength carbon steel HARDOX 500, austenitic steel 08CH18N10T

3. HIGH-STRENGTH STEELS

High-strength steels should be considered sensitive to cold cracking and prone to the formation of retarded cracks induced by diffusion hydrogen. The higher the yield strength, the higher this sensitivity. Since the cold cracking behavior in steels has a great influence on the welding parameters and thus on the production costs of structural elements, extensive

research into cold cracking has been carried out by steel manufacturers and research institutes.
The cold cracking behavior of welded joints depends, in addition to the chemical composition of the base material and the weld metal, on the following factors: sheet thickness, preheating and interpass temperatures, heat input, internal stress state and stiffness of the welded structure. However, the interaction between the tendency to form cold cracks and the mechanical properties of the welded joints must be taken into account. In addition to the above-mentioned influencing factors, this also includes the geometry of the weld and the welding process.

The influence of interpass temperatures on the mechanical properties of the weld joint
Too fast cooling results in high hardness values in the HAZ. Too slow cooling risks not guaranteeing the required strength and toughness values in the HAZ.
In practice, this means that the higher the yield strength, the more different the mechanical values will be if the welder changes the welding speed. This is more than likely the case with manual welding and must be taken into account when evaluating mechanical tests.

3.1 Damaging effect of hydrogen

Hydrogen has the smallest atoms of all gases and is dissolved in a solid, metallic matrix after high temperature ranges. Depending on the type of steel and the amount in the weld metal, this hydrogen can lead to the formation of cracks in the weld joint. Cracks induced by hydrogen do not have to occur immediately after welding. Cracks sometimes occur after 48 hours. These are always brittle, transcrystalline cracks that occur transversely to the weld joint.
The welding result of high-strength steels can be significantly influenced by the choice of the location of the weld joint during the construction of the weldment, and subsequently by the choice of a suitable filler material. Determining the welding procedure. Here, a frequent mistake occurs when verifying the procedure, when the strength of the future welds and their design are not taken into account during test welding (for economic reasons). Testing simple fillet or butt joints may not take their resulting stiffness into account for these steels. This is where problems often occur after the weld is made. Hot cracks, cracks induced by diffusion hydrogen, etc. This is usually caused by the sum of relatively "minor" errors in determining the welding procedure, which are not taken into account much in the case of classic structural steels.
For high-strength steels, subsequent final inspection is also important, from the point of view of crack initiation. Suppressed cracks induced by diffusion hydrogen may only appear after 48 hours, so a weldment inspected by capillary testing immediately after welding may be good, but after delivery to the customer may be a "scrap" piece, therefore, for these types of steels, it is recommended to observe the period after which final inspection will take place, specifically capillary testing, or possibly magnetic testing.

4. FERRITIC STAINLESS STEELS

In general, all types of ferritic stainless steels require a detailed analysis of the chemical composition and condition of the steel. The structure of the steel can be purely ferritic, martensitic, martensitic-austenitic or martensitic with carbide and carbonitride precipitates. From a welding point of view, the low toughness of hardenable ferritic stainless steels means that there is a risk of hydrogen-induced cold cracking, which can be avoided by using filler materials with a low content of diffused hydrogen in the weld metal.

Stainless steels are welded with low heat input using filler materials, preferably of the same chemical composition. In cases where the weld joint operates at temperatures lower than 400 °C, an austenitic filler material with higher plasticity in the weld metal can be used for welding. This reduces the possibility of cold cracks.

Austenitic stainless chromium steels contain at least 16.5 wt. % Cr with sufficient amounts of Ni and Mn and C (N) to achieve an austenitic structure. Other elements to obtain the required properties may be Mo, Ti, Nb, Cu, Si. The structure of austenitic steels can be determined in advance using the calculation of Cr and Ni equivalents with subsequent representation in Schaeffler, Delong, W.R.C. or implant diagrams.

Steels are supplied with different delta ferrite contents in terms of suppressing hot cracks. The amount of delta ferrite is expressed by the ferrite number (FN), which indicates the magnetic attraction of the ferromagnetic phase approximately the content of delta ferrite in the solid solution of austenite. It is determined in the range of 0 to 10% according to EN ISO 8249.

4.1 Special features when welding austenitic steels

As already mentioned, a serious problem of unstabilized austenitic steels and welded joints is their reduced resistance to intergranular corrosion, namely at higher temperatures. At temperatures of 450 to 850 °C, in unstabilized austenitic steels, intensive formation (precipitation) of chromium carbides along grain boundaries occurs, while the areas adjacent to the carbides are simultaneously depleted (denuded) of chromium. As a result of the corrosive agent, intensive intergranular corrosion occurs in the chromium-depleted areas. Similarly, during welding, in unstabilized austenitic steels, the formation of depleted zones in areas of the welded joint heated to temperatures of 450 to 850 °C and further exposed to the effects of the corrosive agent occurs. Another problem in welding austenitic steels is their susceptibility to the formation of carbide and intermetallic phases in the HAZ, where microsegregation of phosphorus and sulfur along dendrites and grain boundaries can also occur during the welding process.

The picture (Fig. 4) shows prepared samples for welding a heterogeneous weld joint, on which individual tests will subsequently be performed to verify chemical and mechanical properties.

Fig. 4 Weld samples

5. PREPARATION OF MATERIAL FOR PERFORMING INDIVIDUAL TESTS

To perform the tests, it is necessary to prepare individual samples. In order to have a sufficient number of samples for the selected tests, it is necessary to determine the cutting plan and place the individual test bodies in the prepared welded sample so that all samples have the required dimensions and at the same time contain the entire weld area (HAZ of the base material 08Ch18N10T, additional material Inertrod 309L, HAZ of the base material HARDOX 500). For this reason, the cutting plan must be performed in both a transverse section (Fig. 5) and a longitudinal section (Fig. 6).

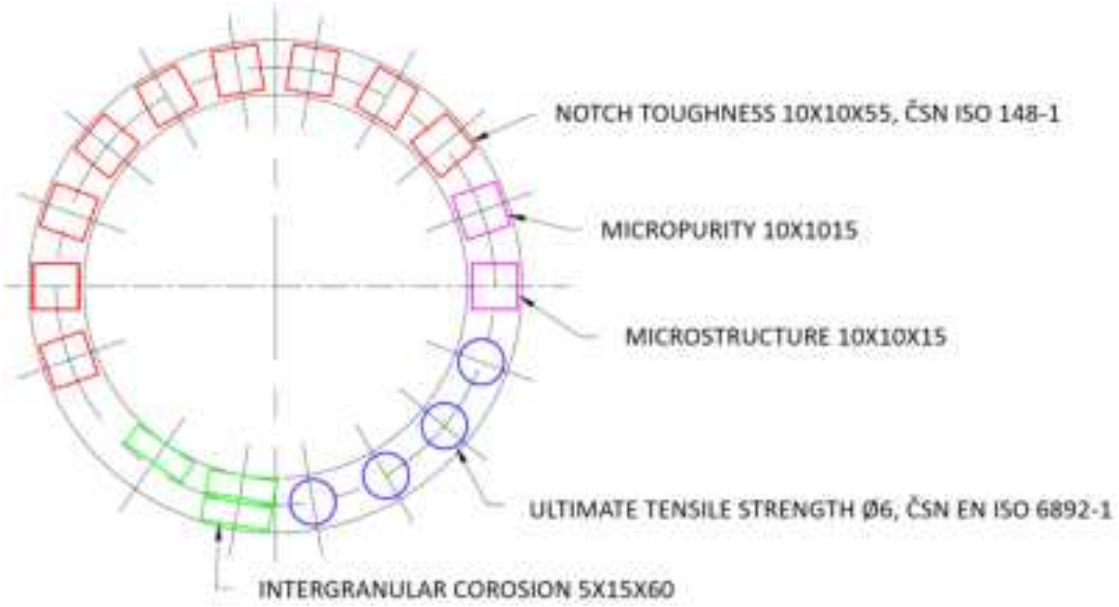

Fig. 5 Cross-sectional plan

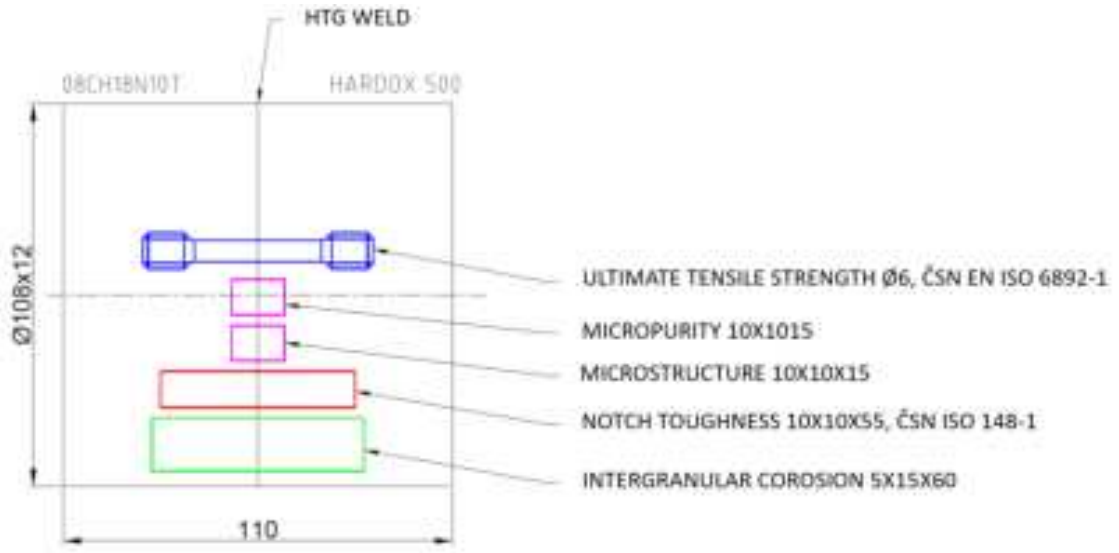

Fig. 6 Sectional plan in longitudinal section

The dimensions of individual samples are given by the standards according to which the given test is performed.
At the same time, the number of individual samples for the given test is calculated.

CONCLUSION

During welding, it is necessary to comply with all the required criteria for welding individual steels (HARDOX 500, 08CH18N10T), where the probability of weldability is relatively high. In case of negative results, it is possible to perform a range of subsequent heat treatment, which can significantly affect the mechanical properties of the welded joint and HAZ.
Within the framework of this project, the weldability of the materials in question with significantly different grain structure, chemical and mechanical properties will be verified.

REFERENCES

LEINVEBER, Jan a VÁVRA, Pavel. Strojnické tabulky: pomocná učebnice pro školy technického zaměření. 2., dopl. vyd. Úvaly: Albra, 2005. ISBN 80-7361-011-6.

PTÁČEK, Luděk. Nauka o materiálu I. Brno: CERM, 2001. ISBN 80-7204-193-2

PTÁČEK, Luděk. Nauka o materiálu II. 2. opr. a rozš. vyd. Brno: CERM, 2002. ISBN 80-7204-248-3

Svařované tlakové nádoby z austenitických nerezavějících ocelí: konf., Brno 1977: sborník přednášek. Brno: Dům techniky ČVTS, 1977

ČSN EN ISO 6892-1 (420310) A Kovové materiály - Zkoušení tahem. Část 1, Zkušební metoda za pokojové teploty = Metallic materials - Tensile testing. Part 1, Method of test at room temperature. Praha: Úřad pro technickou normalizaci, metrologii a státní zkušebnictví, 2021. Dostupné také z: http://csnonline.agentura-cas.cz/.

ČSN ISO 148-1 (420381) N Kovové materiály - Zkouška rázem v ohybu metodou Charpy. Část 1, Zkušební metoda = Metallic materials - Charpy pendulum impact test. Part 1, Test method. Praha: Úřad pro technickou normalizaci, metrologii a státní zkušebnictví, 2010. Dostupné také z: http://csnonline.agentura-cas.cz/.

ČSN EN ISO 3834-1 Požadavky na kvalitu při tavném svařování kovových materiálů: Část 1: Kritéria pro volbu odpovídajících požadavků na kvalitu. Květen 2022. Praha: Česká agentura pro standardizaci, 2022.

COMPARISON OF THE EFFICIENCY OF CALCULATIONS OF MINIMUM WALL THICKNESSES OF SMALL-CALIBER BARRELS

Ing. Ing. Polášek M.[1]
Ing. Bilka M.[2]
Assoc. prof. Ing. Kohutiar M, PhD.[3]
Mgr. Josef Maryáš, Ph.D.[4]

[1]ORCID: 0009-0004-5275-5242, Alexander Dubček University of Trenčín, Faculty of Special Technology, Department of Mechanical Technologies and Materials, Ku Kyselke 469, 911 06 Trenčín, **Slovakia**
[2]ORCID: 0009-0009-9673-3754, Alexander Dubček University of Trenčín, Faculty of Special Technology, Department of Mechanical Technologies and Materials, Ku Kyselke 469, 911 06 Trenčín, **Slovakia**
[3]ORCID: 0000-0002-4710-5913, Alexander Dubček University of Trenčín, Faculty of Special Technology, Department of Mechanical Technologies and Materials, Ku Kyselke 469, 911 06 Trenčín, **Slovakia**
[4] VTÚ, state enterprise, branch plant VTÚVM, Slavičín, Czech Republic

Abstract: In every weapon system or small-caliber firearm, safety for users is essential. Safety in small-caliber firearms is associated with the firing process. Dangerous areas include the breech mechanism and its strength during firing. Another crucial aspect of safety in using small-caliber firearms is the proper dimensioning of the barrel during firing, with both standard and proof ammunition. The barrel of a small-caliber firearm must be functional according to the requirements of the client and, if possible, as light as possible while maintaining proper functionality within the given parameters. However, sometimes there is no requirement for low weight, for example, in sports firearms where accuracy is paramount. We will focus on the correct calculations for the minimum wall thickness of the barrel in this work.
Keywords: gun barrel, barrel strength, yield strength, pressure in the barrel

1. INTRODUCTION

When designing a new barrel for a small-caliber firearm, safety is essential, but the requirement is usually for safety with proper system functionality. The main requirement for small-caliber firearms is to achieve the lowest possible weight of the barrel and thus the overall weapon or weapon system, which are often conflicting requirements. Of course, other requirements are also important if we need a barrel that, in addition to the required durability, has the best possible accuracy for long-distance shooting. We require a longer barrel as well as larger outer diameters of the barrel. If we were designing a barrel for an automatic

weapon, we would also have to consider barrel cooling, which usually also means further increasing the outer diameters and thus the weight. Once we have established the requirements for the type of weapon we are designing the barrel for, whether it is a bolt-action rifle for hunting, a bolt-action rifle for precision shooting (“sniper rifle”), semi-auto, full-auto, or something for special use, we must base our calculations on the internal ballistics of the given cartridge or caliber. When we have the internal ballistics throughout the entire proposed barrel length and the material parameters we will use to manufacture the barrel, we can use appropriate types of calculations to determine the minimum diameters in each part of the barrel. The suitability of individual calculations for the minimum safe diameters of barrels will be addressed in this work.

2. EXPERIMENTAL DETAILS

To calculate internal ballistics, we used the Quick-LOAD program, which calculates internal ballistics based on input data, which are:

- cartridge – .50 BMG (12.7x99 mm)/CIP standard,
- gun barrel length 800 mm (including cartridge chamber),
- gun powder type LOVEX D100, producer Explozia Pardubice (CZ),
- amount of gun powder 14.3 g = 220.7 grains/reloading tables Explozia Pardubice (CZ),
- total maximum cartridge length .50 BMG – 138.31 mm/CIP standard,
- usable cartridge content .50 BMG – 15,809 cm3/QuickLOAD,
- bullet Hornady A-MAX 50cal. 750 grains/item 5165 Hornady.

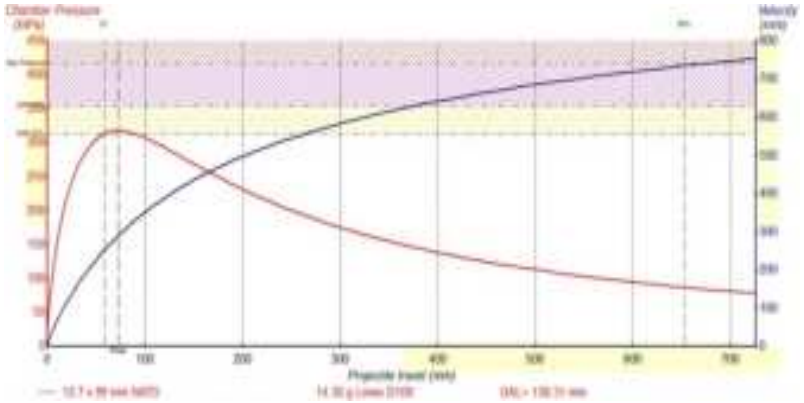

Fig. 1 Graphical representation of the course of pressure profile in the QuickLOAD pro-gram (red), the velocity of the projectile bottom (blue) and in the barrel (without the cartridge chamber) at 20 ° C

In Fig. 1 we can see a graph of the course of the barrel pressure in dependance on the barrel length, where is a sharp rise in pressure to maximum pressure and a gradual decline of the barrel pressure after reaching maximum. This graph also shows the acceleration of the projectile in the barrel de-pending on the length of the barrel. Speed and pressure are

marked from the bottom of the projectile. The bottom of the projectile is 73.808 mm from the bottom of the barrel.

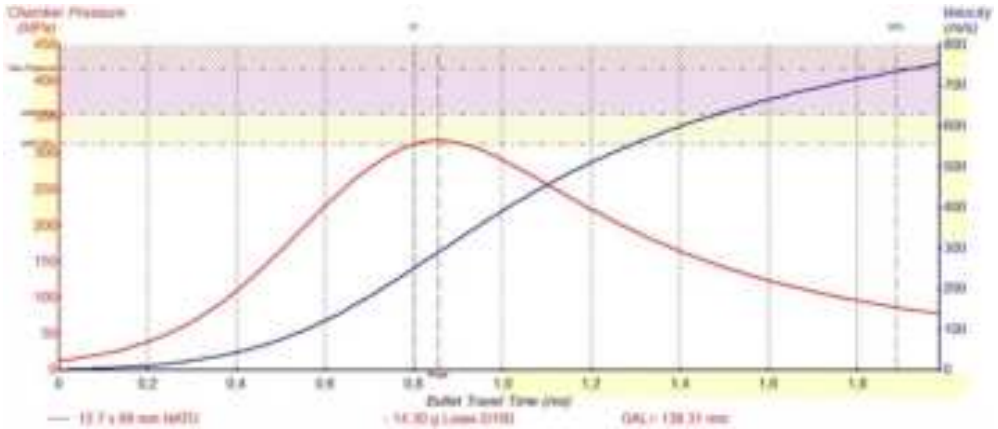

Fig. 2 Graphical representation of the course of pressure profile depend on time in the QuickLOAD pro-gram (red), the velocity of the projectile bottom (blue) and in the barrel (without the cartridge chamber) at 20 ° C

Fig. 2 shows a graphical representation of the pressure and velocity profile of the base of the projectile over time in the barrel. As seen in the graph, the barrel is a very non-standard pressure vessel, which fills to a maximum pressure of around 300-400 MPa in less than 1 ms. It empties in about 1 ms. This entire process occurs in less than 2 ms, with the barrel being continuously emptied during filling due to the expanding gases flowing around the projectile in the barrel. The graph shows that reaching maximum pressure takes about 40% of the total time of the shot. Furthermore, we see that the acceleration of the projectile is greatest around the maximum pressure in the barrel. After that, the acceleration of the projectile slowly decreases. This also causes the extension of the barrel beyond 700-800 mm to only slowly increase the muzzle velocity of the projectile, even though each increase in muzzle velocity means an increase in the projectile's energy. For comparison, barrels with lengths of 28" (71.12 cm) and 48" (121.92 cm) were used to fire a Hornady A-Max bullet weighing 750 grains (48.599 g). With a 28" barrel, the muzzle velocity is 2700 fps (822.96 m/s). With a 48" barrel, the muzzle velocity is 2700 fps (899.16 m/s). This difference is 76.20 m/s, which is a significant energy difference for a projectile weighing 48.599 g. The exact energy difference for a projectile fired from a 28" barrel and a 48" barrel is 3188.71 J. This energy difference is more than six times the total energy of a 9x19 (Luger) cartridge.
We made the calculation at the following places in the barrel:

- bottom of the cartridge chamber, inner diameter at least 20.52 mm, safety coef. k = 1.1, design pressure 529.1 MPa,
- cartridge case top, inner diameter at least 14.33 mm, safety coef. k = 1.1, design pressure 529.1 MPa,
- place of maximum pressure, inner diameter 13 mm, safety coef. k = 1.2, design pressure 577 MPa,

- place at the end of the barrel, inner diameter 13 mm, safety coef. k = 1.2 (safety coefficient at the end of the barrel is stated at least 2.5 in the literature [6], but since the condition of the minimum wall of the barrel is 2.5 mm, this condition of the safety coefficient is exceeded many times), design pressure 123.24 MPa, or at least the thinnest wall 2.5 mm, because the calculated size is usually smaller.

3. RESULTS AND DISCUSSION

Demonstration of each type of calculation of a simple unstrengthen barrel at material strength Re = 1100 MPa

3.1 Method 1. Calculation performed in the flexi-ble area with sample calculation, according to the authors M. Fišer and S. Procházka, at Re = 1100 MPa

Dynamic value of yield strength:

- at Re = 1100 Mpa
- the calculated value is σKD = 1133 Mpa
- p = pk – inner pressure

$$\alpha = \left(\frac{\sigma_{KD}}{p_K} \right)^2 \qquad (1)$$

- at pk = 529.10 MPa the calculated value of the coefficient α = 4.59
- at pk = 577 MPa the calculated value of the coefficient α = 3.86
- at pk = 123.24 MPa the calculated value of the coefficient α = 84.52

$$x = \sqrt{\frac{\alpha + \sqrt{4\alpha - 3}}{\alpha - 3}} \qquad (2)$$

- at pk = 529.10 MPa, x = 2.315
- at pk = 577 MPa, x = 2.936
- at pk = 123.24 MPa, x = 1.123
- d2MN – minimum outer diameter of the barrel
- r1 – inner radius of the barrel
- d1 – inner diameter of the barrel

$$d_{2MN} = d_1 \sqrt{\frac{\alpha + \sqrt{4\alpha - 3}}{\alpha - 3}} \qquad (3)$$

$$d_{2MN} = d_1 \,.\, x \qquad (4)$$

Table 1
Calculated minimum outer diameters of the barrel by Method 1 at Re = 1100 MPa

P.č.	r_1 (mm)	d_1 (mm)	d_{2MN} (mm)	α	x	p (MPa)
1	10,40	20,80	47,52	4,59	2,32	529,1
2	7,165	14,33	33,18	4,59	2,32	529,1
3	6,50	13,00	38,18	3,86	2,94	577,0
4	6,50	13,00	14,60	84,52	1,12	123,24

This method is suitable for calculations when there is a large difference between the design pressure and the yield strength pressure of the material. The yield strength is significantly higher than the design pressure, which means that the value of the coefficient α is much greater than 3. If the coefficient α is close to 3, the calculated values are unrealistically large. This can be mitigated by replacing the material with a better one that has a higher yield strength.

3.2 Method 2. According to the author J. Škvarek, using the strength theory based on the maximum shear stress with a sample calculation at Re = 1100 MPa [13]

$$\sigma_{red}^{II} = \frac{2}{3} \cdot \frac{\sqrt{3}x^2}{a^2 - 1} \cdot p_1 \qquad (5)$$

where:

- a = r2 / r1 a x = r2 / r
- r1 – inner radius of the barrel
- r2 – outer radius of the barrel
- r – radius of the barrel at the point of calculation
- p = pk = p1 – internal pressure
- σ_{red2} – maximum shear stress

When calculating the minimum wall thickness of the barrel, the yield strength will not be exceeded beyond 0.5 mm from the inner side of the barrel wall.

Table 2
Calculated minimum outer diameters of the barrel using Method 2 at Re = 1100 MPa

P.č.	r_1 (mm)	r_2 (mm)	d_{2MN} (mm)	r (mm)	$r-r_1$ (mm)	a	x	p (MPa)	s_{red2} (MPa)
1	10,40	21,20	42,40	10,90	0,50	2,04	1,94	529,1	1098,68
2	7,165	12,50	25,00	7,665	0,50	1,91	1,74	529,1	1090,68
3	6,50	12,00	24,00	7,00	0,50	2,15	2,00	577,0	1098,53
4	6,50	7,22	14,44	7,00	0,50	1,10	1,02	123,24	1099,07

In this method, according to the theory of maximum shear stress, it follows that the reduced stress on the inner surface of the wall is greater (or overestimated compared to the actual

pressure) than in the theory of maximum elongation, from which the shear stress method is derived (at higher pressures). At lower pressures, it is the opposite.

3.3 Method 3. According to the authors J. Pech and F. Kozderek with sample calculation at Re = 1100 MPa [10]

$$R = r.\sqrt{\frac{k+0,4.p}{k-1,3.p}} \qquad (6)$$

Formula for calculating the minimum wall thickness:

- R – outer radius,
- r – inner radius,
- $p_k = p$ – inner overpressure,
- k – allowable stress (yield strength).

Table 3
Calculated minimum outer diameters of the barrel by Method 3 at Re = 1100 MPa

P.č.	r (mm)	d_{2MN} (mm)	p (MPa)
1	10,40	36,75	529,1
2	7,165	27,89	529,1
3	6,50	25,17	577,0
4	6,50	14,36	123,24

This method is very practical. With this method it is possible to calculate favourable results, even if the results of other methods are already really unusable values (meaning very big minimum outer averages, which can no longer be used in practice). This method shows that it is older, from the war period, when the designers could quickly verify in practice what they calculated, and thus created more effective empirical methods than just theoretical way.

3.4 Method 4. authors from TFA Rheinmetal-Bors. Taschenbuch f.d. Artilleristen with a sample calculation at Re = 1100 MPa [10]

$$R = r.\sqrt{\frac{3.k+2.p}{3.k-4.p}} \qquad (7)$$

Formula for calculating the minimum wall thickness:

R – outer radius
r – inner radius
p – internal overpressure
k – allowable stress (yield strength)

Table 4
Calculated minimum outer diameters of the barrel by Method 4 at Re = 1100 MPa

P.č.	r (mm)	d_{2MN} (mm)	p (MPa)
1	10,40	39,53	529,1
2	7,165	30,31	529,1
3	6,50	27,35	577,0
4	6,50	14,61	123,24

This method is similar to method 3, making it a very practical method according to the book from which the author derived this calculation. It is a method from before World War II, when exactly the same principles applied as I mentioned in method 3. The results are slightly larger (by a few percent, depending on the difference between the design pressure and the yield strength of the material) than those of method 3, but they are also very practically usable.

3.5 Results of Outer Wall Diameters at Re = 1100 MPa, Calculated by All Methods

Table 5
Calculated Minimum Outer Diameters of the Barrel at Re = 1100 MPa

re=1100MPa, min. diameters	diameter 20,8 mm	diameter 14,33 mm	diameter 13 mm	diameter 13 mm
method	Pk 529,1 MPa	Pk 529,1 MPa	Pk 577 MPa	Pk 123,24 Mpa
1 [mm]	47,65	33,18	38,18	14,60
2 [mm]	51,00	35,10	43,00	14,48
3 [mm]	36,75	27,89	25,17	14,36
4 [mm]	39,53	30,31	27,35	14,61
max. [mm]	51,00	35,10	43,00	14,61
min. [mm]	36,75	27,89	25,17	14,36
diameter difference max-min [mm]	14,25	7,21	17,83	0,25
radius difference max-min [mm]	7,13	3,61	8,92	0,13
difference max-min [%]	38,78	25,85	70,84	1,74

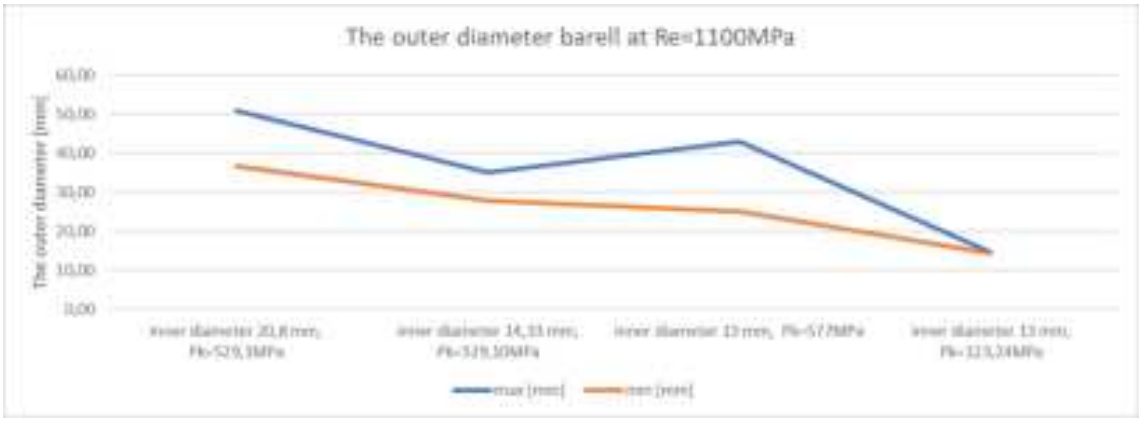

Fig. 3 Graph of the Envelope Curve of Minimum and Maximum Diameter at Re = 1000 MPa

In Table 5 and Fig. 3, we see the calculated values and graphical representation of the calculated minimum diameters of the barrel at four points (these points are very important for the design of the external dimensions of the barrel) with a yield strength of the material used for the barrel of 1100 MPa. The first point is at the bottom of the chamber, the second is at the end of the chamber, the third is at the point where the maximum pressure in the barrel is calculated, and the fourth point is at the end of the barrel, where the pressure is the lowest. With this yield strength value, which is almost double the design pressure, all methods calculate very similar and acceptable results for the minimum diameters. It is also evident here that the last two methods calculated the smallest minimum diameters, which is best for the user (for a lighter weapon). The largest differences in results between different methods are at high design pressures and large internal barrel diameters. As the internal diameters and design pressures decrease, the differences in the calculated results also decrease.

3.6 Results of Outer Wall Diameters at Re = 900 MPa, Calculated by All Methods

Table 6
Calculated Minimum Outer Diameters of the Barrel at Re = 900 MPa

re=900MPa, min. diameters	diameter 20,8 mm	diameter 14,33 mm	diameter 13 mm	diameter 13 mm
method	Pk 529,1 MPa	Pk 529,1 MPa	Pk 577 MPa	Pk 123,24 Mpa
1 [mm]	99,99	69,83	N	14,95
2 [mm]	N	N	N	14,89
3 [mm]	47,15	36,31	35,46	14,74
4 [mm]	52,76	44,89	40,49	15,05
max. [mm]	99,99	69,83	40,80	15,05
min. [mm]	47,15	36,31	35,46	14,74
diameter difference max-min [mm	52,84	33,52	5,34	0,31
radius difference max-min [mm]	26,42	16,76	2,67	0,16
difference max-min [%]	112,07	92,32	15,06	2,10

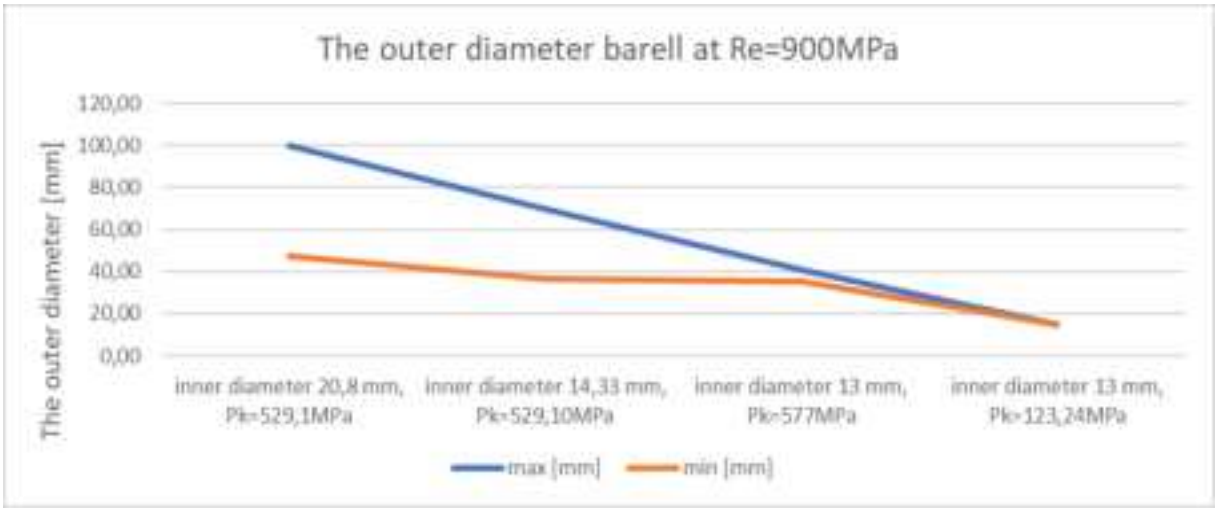

Fig. 4 Graph of the Envelope Curve of Minimum and Maximum Diameter at Re = 900 MPa

In Table 6 and Fig. 4, we see the calculated values and graphical representation of the calculated minimum diameters of the barrel at four points, with a yield strength of the material used for the barrel of 900 MPa. With this yield strength value, which is 200 MPa lower than the previous calculation, we see that the methods begin to reach their limit values, specifically methods 1 and 2. Again, it is evident that methods 3 and 4 calculated the smallest minimum diameters, which is best for the user (for a lighter weapon).

3.7 Results of Outer Wall Diameters at Re = 800 MPa, Calculated by All Methods

Table 7
Calculated Minimum Outer Diameters of the Barrel at Re = 800 MPa

re=800MPa, min. diameters	diameter 20,8 mm	diameter 14,33 mm	diameter 13 mm	diameter 13 mm
method	Pk 529,1 MPa	Pk 529,1 MPa	Pk 577 MPa	Pk 123,24 Mpa
1 [mm]	N	N	N	15,18
2 [mm]	N	N	N	14,89
3 [mm]	61,84	65,17	57,79	15,01
4 [mm]	71,93	89,27	80,53	15,37
max. [mm]	72,80	89,27	82,00	15,41
min. [mm]	61,84	50,20	57,79	14,88
diameter difference max-min [mm	10,96	39,07	24,21	0,53
radius difference max-min [mm]	5,48	19,54	12,11	0,27
difference max-min [%]	17,72	77,83	41,89	3,56

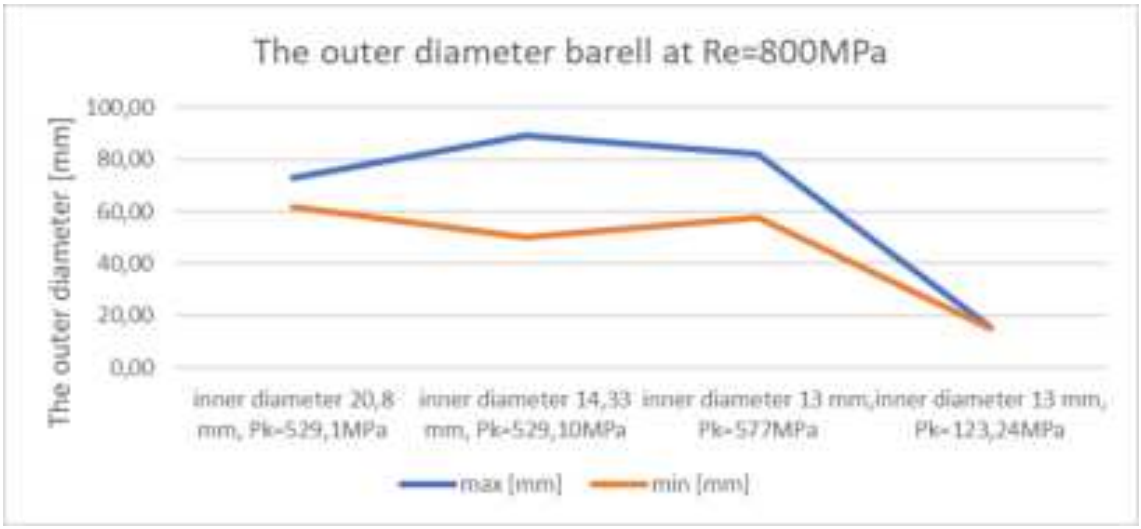

Fig. 5 Graph of the Envelope Curve of Minimum and Maximum Diameter at Re = 900 MPa

In Table 7 and Fig. 5, we see the calculated values and graphical representation of the calculated minimum diameters of the barrel at four points, with a yield strength of the material used for the barrel of 800 MPa. With this yield strength value, which is 100 MPa lower than the previous calculation, we see that the first two methods reach their limit values. This is true for all points except the point where the design pressure is the lowest. Again, it is evident that methods 6 and 7 calculated the smallest minimum diameters, which is best for the user (for a lighter weapon).

3. CONCLUSION

Empirical calculations to determine the minimum safe wall thickness of a small-caliber barrel used in this work are from different time periods. The first two are newer and the other two are older, from the period before and immediately after World War II. According to the calculated values in the work, the usability of each method is best if we use a material for the production of the small-caliber barrel whose yield strength is approximately twice as high as the maximum design pressure in the barrel. Limited by the yield strength of the chosen material, we can process the material appropriately, as we will drill and further machine it along its entire length in its hardened state. In practice, hardened materials with a hardness of 35-40 HRC are used; at higher hardness, machining becomes problematic due to tool life. The results of the methods used in this work show that overall lighter safe small-caliber barrels can be calculated using methods that emerged around World War II (Methods 3 and 4). Thus, in a period when development in this area was progressing at a high pace. Furthermore, the newer methods (Methods 1 and 2) used in this work can be considered methods with a higher safety coefficient. This makes sense, as in peacetime there is an effort to achieve a higher degree of safety. Our tests on the MP50 rifle, which was developed and manufactured in Slovakia, caliber 50 BMG. These rifles were loaned to us for testing by the

manufacturer, MIPO Slovakia s.r.o. We can also consider the calculations from the World War II period (Methods 3 and 4) to be very safe calculations and possibly slightly overdimensioned.

ACKNOWLEDGEMENTS

This research work was created within the project “Research on the Characteristics of Steels Essential for Increasing the Durability of Selected Special Equipment Structures”, code of the project D08_2024, based on the financial support from the Internal Grant Scheme of the Alexander Dubček University of Trenčín (Call for proposals: Early Stage Grants).

REFERENCES

[1] Fišer, M. 2003. Malorážové zbraně. Zaklady konstrukce, U-1172. Brno : Vojenská akademie v Brně, 2003. 360 p.

[2] Fišer, M. and Balla, J. 2004. Malorážové zbraně, konstrukce, U-1377. Brno : Univerzita obrany, 2004. 399 p. ISBN 8085960796.

[3] Pech, J. and Kozderka, F. 1953. Poznámky o onštrukcii automatických zbraní. Praha : Konštrukta Praha, 1953.

[4] Fišer, M. and Popelínský, L. 2004. Malorážové zbraně: Konstrukce. Brno : Univerzita obrany, 2004. ISBN 80-85960-79-6.

[5] Fišer, M. and Procházka, S. 2007. Projektovaní loveckých, sportovních a obranných zbraní. Ostrava : Vysoka škola báňská, 2007. 142 p.

[6] Polášek, M. 2020. Ideový návrh jednorano-vej odstreľovacej pušky kaliber .50 BMG. Diplomová práca. Alexander Dubček University of Trenčín. Trenčín : 2020. 91 p.

[7] Lobaev, V. 2010. The Sharpshooting. 2010. ISBN 9785902073727.

[8] Lilja, D. and Lilja, S. 2020. Barrel Lengths & Velocities for the 50 BMG. [online]. Available at: https://riflebarrels.com/barrel-lengths-velocities-for-the-50-bmg/ [Accessed 15 Oct. 2024].

[9] Fišer, M., Lipták, P., Procházka, S., Macko, M. and Jozefek, M. 2006. Automatické zbrane: Konštrukcia skúšanie, 1st ed. Trenčín : Trenčianska univerzita Alexandra Dubčeka v Trenčíne, 2006. 263 p. ISBN 80-8075-089-0.

[10] Popelínský, L. 2000. Projektování automatických zbraní: Výpočet funkčního diagramu automatické zbraně, 1st ed. Brno : Vojenská akadémia, 2000. 118 p.

MODIFICATION OF THE ELECTRON BEAM GENERATION SYSTEM TO INCREASE THE DYNAMICS OF THE WELDING CURRENT CONTROL

Ing. Rastislav Sekerka[1]
Ing. František Kolenič, PhD.[2]
Ing. Peter Koršňák[3]
[1]ORCID: 0000-0001-6968-367X, PRVÁ ZVÁRAČSKÁ, a.s., **SLOVAKIA**
[2]ORCID: 0000-0001-9920-2398, PRVÁ ZVÁRAČSKÁ, a.s., **SLOVAKIA**
[3]ORCID: 0000-0003-2771-556X, PRVÁ ZVÁRAČSKÁ, a.s., **SLOVAKIA**

Abstract:

The paper presents a modern concept of dynamic control of the welding current of an electron beam welding machine using Flyback topology. The contribution presents a new concept of dynamic control of the welding current of electron beam devices. The results of the analysis of the modules of the welding current regulation source, designed with the primary use of impulse sources, clearly pointed out the potential of the flyback topology to achieve the rise and fall of the control voltage of the welding current from 0 to 5 kV and back to 0 in a time horizon of up to 1 ms. In the solution process, it was shown that good dynamics of welding current control can be achieved even with high-voltage separation of the primary and secondary circuits of the source at the level of 100 kV. A functional time model of control, regulation and switching of the source with rising and falling edges up to 1ms was created. Based on the achieved results, a functional model of dynamic control of the welding current was created with the dynamics of the start-up and run-down of the welding current within 1 ms. To verify the technological possibilities of the designed system, an experimental workplace with an integrated welding current control system was built. Two technologies were verified – welding of an aluminum alloy with a pulsed current and drilling holes in a 2 mm thick steel sheet with an electron beam.

Keywords: electron beam, EB current control, topology of current control

1. INTRODUCTION

Electron beam welding equipment and technologies have been operated by PRVÁ ZVÁRAČSKÁ for over two decades. During this period, the equipment has undergone various innovations and improvements, not only due to the change in the component base, but also, as a priority, the improvement of individual parameters. Such a relentless effort to innovate technological complexes has a great economic impact and allows us to improve our position in the highly competitive environment of global manufacturers of similar equipment.

The delivery of electron beam welding technological complexes is carried out within the framework of a modular concept [3,4], which allows us to gradually improve individual modules while maintaining the input-output requirements for each module separately, and

innovations do not affect other parts of the system. Each module can operate as a completely independent unit, and this approach represents a great opportunity to meet the different requirements of individual customers.
Increasing the dynamics of welding current control is one of the basic prerequisites for expanding the applications of electron beam technologies in the field of ecological production of vehicles, components in the production of renewable energy sources and other technologies for decarbonization of industry, which are currently coming to the forefront in the industrial sector. After an in-depth analysis of the results obtained, this assumption appears to be feasible.
The update of the technical solution of the functional node – a Wehnelt source with higher control dynamics – consists in an original circuit solution in the use of 3 separate branches on the secondary side connected in series, which on the one hand has increased the number of components used, which encourages the feeling that the mean time to failure of the entire module is decreasing, but at the same time we have distributed the voltage stress over three branches and thus achieved higher reliability. This solution provides significant added technical value to the electron beam generation system and expands the functionality of the entire electron beam welding system as a whole. After implementation, we will achieve an increased level of dynamics in the control of process parameters and will also improve the system‘s response to resolving critical conditions.

2. RESEARCH ON DYNAMIC CONTROL CIRCUITS OF WELDING CURRENT OF ELECTRON BEAM EQUIPMENT

2.2 Original concept of welding current control

The original concept of electron beam devices in the welding current control part was designed for power control as passive, where the electrode gun was considered as a passive element, the circuit solution included passive components and the parameters of the entire HV route were taken as a passive chain. The secondary side was not equipped with any active elements that would compensate for the natural properties of the passive network.
With the general increase in the availability of higher-quality components, the possibilities of applying active elements on the high voltage side gradually began to open up. In our case, it is necessary to connect the components to a potential of 60 kV, which means very precise design of circuit connections, use galvanic separations for measuring and controlling parameters on the high voltage side and also use the most modern insulating materials, which subsequently allow reducing the physical dimensions of transformers and other components.
In the passive chain, mainly the filter capacities and cable capacities cause a limitation of the maximum speed of welding current control. This can be eliminated by creating active electronics on the high-voltage side, which will charge and discharge these capacities faster, which will allow to increase the speed of welding current control. With the high availability of modern SMD components (small dimensions, low parasitic inductances), we gain several

advantages. At the same time, as the complexity of circuits increases, the physical dimensions of the circuit connections do not increase, and the lower parasitic inductances of modern components have less impact on the functionality of the circuit connection. The original concept using passive components on the high-voltage side can be seen in Fig. 1 – a view of the rectifier and filter boards of the Wehnelt and Bombard sources. Fig. 2 shows a view of the entire small container where the auxiliary sources for the electrode system are stored.

Fig. 1 Original concept – control node solution with passive components

Fig. 2 Original concept – view of the entire container

The original solution, with the given configuration, cannot provide fast dynamic changes in welding current control. The rise times are in the range of 10-30 ms (Fig. 3).

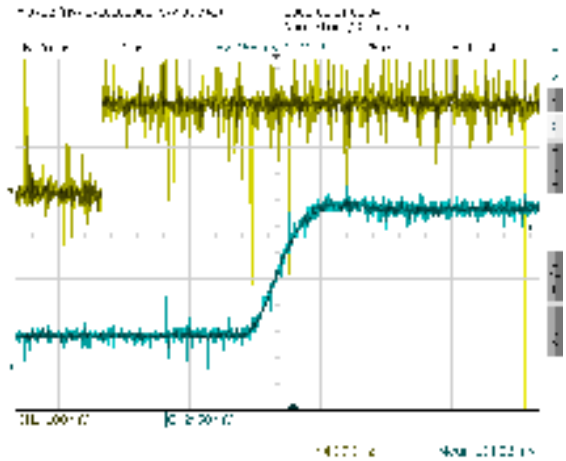

Fig. 3 Welding current ramp (Iz = from 0 to 20mA) - original concept

2.3 New welding current control concept

As mentioned above, in the new concept it was necessary to design circuit solutions based on high potential, the development proceeded in successive steps from the simulation of functionality with the software tools LT Spice and MicroCap to the design of circuit solutions that used the knowledge from the simulation. The most modern available component base was used. The individual stages of development were followed by extensive testing procedures, where reliability, resistance to discharges and breakdowns in the electrode system of the electron gun (which is a frequent phenomenon in electron beam equipment), EMC compatibility and circuit stability were verified. In the resulting design, we designed and implemented a circuit solution with suitable parameters (Fig. 4 and Fig. 5).

Fig.. 4 Solution of the Wehnelt source at a potential of 60kV

Fig. 5 View of a small container with active circuits at a high potential of 60kV

The active elements on the high-voltage side are measured and controlled via feedback using optical cables with converters developed by us. They allow measuring the real operating values of the electron gun parameters and provide their continuous and continuous monitoring. The higher control system can record these values and store them in the welding parameters database, which brings a huge advantage to the technologist in the diagnostics, development and analysis of welding procedures. The entire complex already incorporated into the electron beam complex can be seen in Fig. 6. On the left is the Energoblok, on the right is the power switchboard with the control system for the entire electron beam workplace (welding parameter control, control of movements in the chamber and outside the chamber, control of vacuum equipment and support equipment – cooling, hydraulics, compressed air, etc.

Fig. 6 New concept – Energy block and drive and pumping control switchboard

We subjected the new concept to comprehensive testing, performing various measurements at a wide range of input parameters. The testing was carried out at the following parameters:
Welding voltage U: Uz = 45kV
Primary cathode bombardment current: Ib(prim) = 240mA
Secondary cathode bombardment current: Ib (sec) = 12mA
Focusing current: If = 700mA
Sample distance: h = 262mm (from flange)
Sample movement speed: v = 20mm/s
Setpoint Iz – generator output: Amplitude: U = 1V
Offset: +500mV
Frequency: f = 50Hz/2kHz
Waveform: rectangular/arbitrary waveform

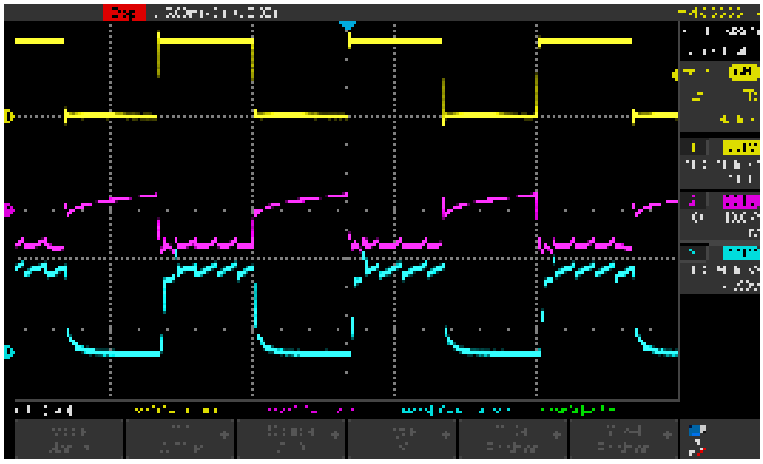

Fig. 7 Welding current – NEW concept – pulses – 50Hz (yellow – setpoint, purple – regulator output Iz, blue – measured value Iz)

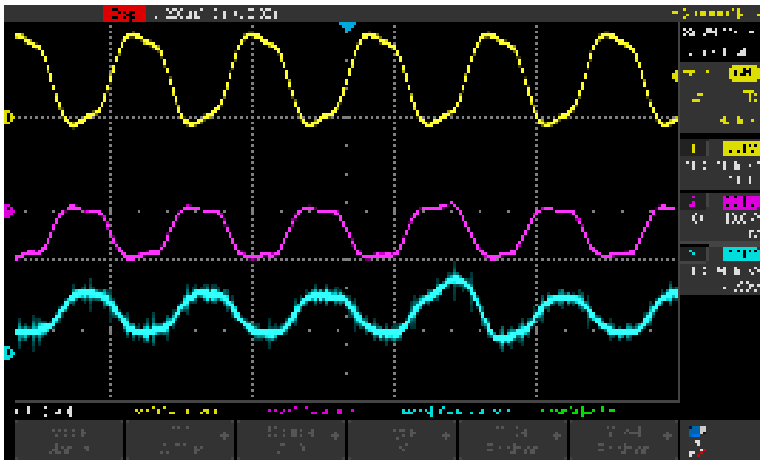

Fig. 8 Welding current – NEW concept – pulses – 2kHz (yellow – setpoint, purple – Iz controller output, blue – measured Iz value)

The measurements in Fig. 7 and Fig. 8 show a step change in the welding current. This increase lasts for approximately 1 ms (with the desired rectangular signal), which opens up possibilities for various applications where pulsation of the welding current can be used.

2.4 Verification on a Faraday cylinder in a chamber

As part of testing the compliance with the required parameters, tests were also performed on the Faraday cylinder in the welding chamber with the following parameters with satisfactory results (Fig. 9):

Comparison of the welding current waveforms Iz – reg (purple) and Iz – faraday (blue)
Welding voltage U: Uz = 45kV
Primary cathode bombardment current: Ib(prim) = 240mA
Secondary cathode bombardment current: Ib (sec) = 12mA
Setpoint Iz (yellow) – generator output Amplitude U = 2V (pulse 0mA – 200mA)

Offset: +1V
Frequency: f = 500 Hz
Waveform: rectangle

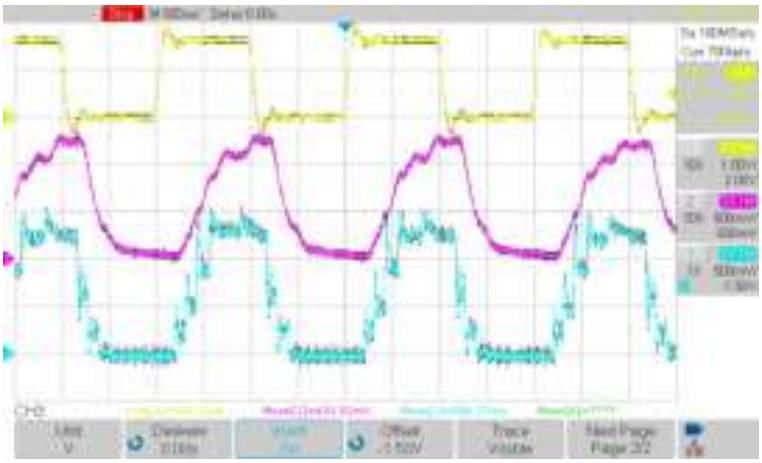

Fig.. 9 Verification using a Faraday cylinder in a welding chamber

2.5 Technological verification of the dynamic welding current control system

Technological verification of the dynamic welding current control system was carried out on two demanding technological applications of electron beam in industrial practice. In the first case, it was a verification of the surface formation of the weld bead and monitoring of the susceptibility to the formation of defects in welded joints of aluminum alloy type EN AW 6005A by pulsed welding current in a variable range of pulsation frequencies from 0 to 2 kHz. In the second case, the possibility of creating holes - punching a steel sheet 2 mm thick with a short, high-energy electron beam pulse was verified.

All verification experiments were carried out on a universal electron beam device PZ EZ UNI 2G. The experimental workplace was arranged in such a way as to enable the implementation of linear welded joints on samples of selected materials of the selected configuration. The motion-mechanical equipment of the workplace allowed positioning of experimental samples in orthogonal linear axes x, y and z with fine regulation of position and speed. The experimental workplace has an internal volume of 3.02 m3 with internal dimensions of 1300 x 1500 x 1550 mm, which represents sufficient space for the implementation of verification technological experiments. The external appearance of the experimental workplace PZ EZ UNI 2G is shown in Fig. 10.

Fig.. 10 Experimental electron beam workstation for research into welding of CrMo steels

The workplace was equipped with an electron beam generation system, into which the developed system of rapid welding current regulation was integrated. An electron gun with a beam power of up to 7 kW was placed on top of the welding chamber. A crystalline lanthanum boride cathode with a diameter of ϕ 1.2 mm was used for electron emission, which was indirectly heated by electron bombardment from the back of the cathode.
The basic technical parameters of the beam generation system in question were as follows:
Acceleration voltage adjustable from 30 to 60 kV,
max. electron beam power up to 7 kW,
beam power regulation range 30 W to 7 kW,
welding current working range from 1 to 120 mA,
acceleration voltage stability ± 1.0%,
control electrode voltage adjustable 0-4 kV,
cathode heating power adjustable from 20-100 W,
focusing current adjustable 0.2 to 2 A,
focusing current stability. ± 0.5%,
electron beam deflection adjustable max. up to ± 7°.
deflection frequency up to 10kHz.
The experimental workstation allowed the beam to be adjusted to the weld joint using a CCD camera. The system is integrated in the electron gun and allows observation of the scene in the beam axis.
From the point of view of electron beam diagnostics, the workstation was equipped with a measurement of the transverse beam energy distribution using the slit method with a Faraday cylinder. For comparison, the measured minimum beam diameter in the focus at a distance of 300 mm from the focusing coil had a value of d = 0.4 mm at an accelerating voltage of 55 kV and a current of 100 mA.

An integral part of the experimental workstation was software for collecting and editing welding process parameters, which allows simultaneous recording of more than 15 process parameters with a sampling period of 1 to 10 ms.
The assembled experimental workstation enabled optimal positioning of prepared experimental samples, precise adjustment of the electron beam to the weld joint, control of electron beam parameters as well as recording of selected welding process parameters.

2.6 Results of verification of pulse welding technology of aluminum alloy type EN AW 6005 A

EN AW-6005A AlSiMg(A) is a medium-strength, heat-treatable alloy with excellent corrosion resistance. It has excellent extrusion properties with a good surface finish. It is used in the extrusion of complex profiles where greater strength is required. The alloy is well weldable by resistance methods and arc methods with filler metal.
The weldability of the alloy in question by concentrated energy sources, such as electron beam, is good when welding with non-pulsed welding current, with good surface formation and no defects in the weld joint. The aim of the verification technological experiments was to compare the properties of weld joints achieved on the aluminum alloy in question with the use of pulsed welding current.
The verification was carried out by remelting on samples 5 mm thick and 300x400 mm in size using the bead on plate method. The first reflow was performed at an accelerating voltage of 46 kV with a constant welding current Iz of 35 mA, focused on the sample surface at a welding speed of 40 mm/s and a total beam power of 1.6 kW. The macrostructure of the reflow is shown in Fig. 12.

Fig. 11 Macrostructure of a welded joint produced by constant welding current

It can be stated that this is a weld with good surface formation without defects and discontinuities in the weld metal (Fig. 11).
Further welds were performed with a pulsed welding current at an effective beam power of 1.6 kW and a welding speed of 40 mm/s. The pulsation frequencies were set to 10Hz, 100

Hz, 200 Hz, 500 Hz, 1000 Hz and 2000 Hz. The time course of the pulsation was a rectangle with levels from 0% to 100% Iz. Fig. 12 shows the macrostructures of welds made with a pulsed welding current at selected pulsation frequencies.

10 Hz

100 Hz

500 Hz

1000 Hz

Fig. 12 Macrostructures of welds made with pulsed welding current at selected frequencies

Based on the analysis of macrosections of the welds on the AW-6005A AlSiMg aluminum alloy, we can conclude that its weldability with a pulsed electron beam is limited. It was observed that in the area of low welding current pulsations up to approximately 100 Hz, when a continuous weld bead does not form, the weld joint is prone to cracking. This is due to the rapid cooling of the weld metal, when high stresses arise in the process of extremely steep solidification, which are the cause of cracking. On the contrary, at high values of welding current pulsations, a quasi-continuous weld bead is formed with typical weld defects, the cause of which is the high dynamics of the weld pool. We observe weld metal spatter, weld root overflow, ignitions, etc. It can be concluded that welding aluminum alloys prone to cracking with a pulsed welding current can be recommended only in special cases.

2.7 **Results of verification of the technology of drilling steel sheets with a concentrated electron beam**

Micro-hole drilling using electron beam technology tests the ability to dynamically control the electron beam. To create holes in metal materials in a vacuum, it is necessary to achieve extraordinary electron beam characteristics. Thanks to the rapid start-up of the welding current to the desired value, a high energy density can be achieved in the focus of the electron beam. To create a hole in a metal material in a vacuum, a beam energy density of at least 108 W/cm² is required.[1,2,4,] This is not possible at lower beam energy densities. A vapor-gas capillary must be formed at the point of impact of the beam on the material, which is filled with molten metal. This forms the basis of the hole. The molten metal in the capillary expands explosively due to the high energy density of the beam and blows the molten metal out of the capillary.

The verification of the electron beam hole-making technology was carried out on the PZ EZ UNI 2G electron beam device, into which an electron beam generation system with high dynamics of welding current control was integrated. A 2 mm thick metal plate made of 11 500 steel was used as a sample. A single electron beam pulse at an accelerating voltage of 46

kV was used to create the hole. The electron beam was focused on the surface of the metal plate and the pulse energy was regulated by the welding current Iz and the rectangular pulse duration. A typical pulse time course is shown in Fig. 13.

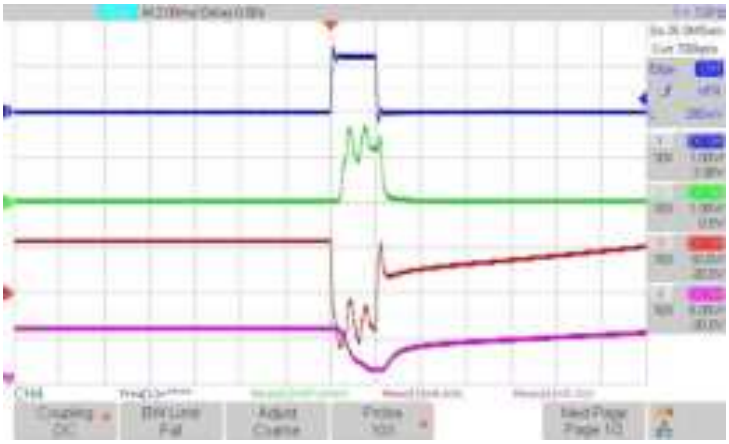

Fig. 13 Time course of the welding current pulse for drilling holes

Legend:
CH1 (blue) - waveform of the welding current setpoint Iz (waveform from the generator)
CH2 (green) - waveform of the measured welding current Iz
CH3 (red) - waveform of the welding current regulator output Iz
CH4 (purple) - waveform of the control voltage Uw (wehnelt)

The pulse duration was 2ms, the welding current was 100 mA and the focusing current If = 756mA. Between the two drilling processes the beam was switched off. In the next position the beam is switched on. This procedure allows very high drilling frequencies. Fig. 14 shows a photograph of the drilled hole.

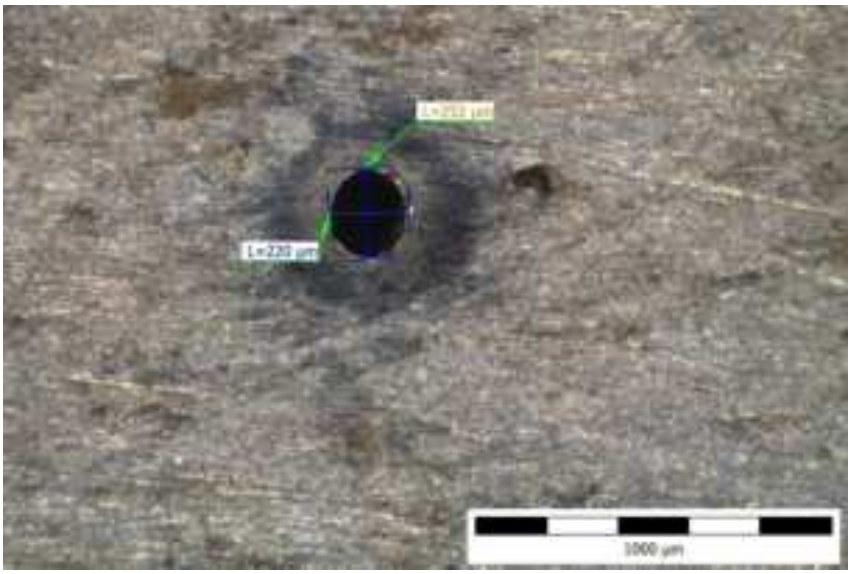

Fig. 14 Dimensions of a drilled hole in a 2 mm thick steel plate

Fig. 15 shows a steel plate with holes drilled by individual pulses according to the above parameters with a pulse duration of 2 ms.

Fig. 15 2 mm thick steel plate with electron beam drilled holes

3. CONCLUSION

The achieved output technical parameters of the dynamic control of the welding current of electron beam devices are as follows:

- voltage range of processing the input measured signal .....0 – 5 kV,
- start and stop of the control voltage of the Wehnelt electrode 0 – 5kV..... up to 1 ms
- output signal in the range .....0-10 V,
- galvanic separation from the measured point .....min. 100 kV,
- width of the transmitted bandwidth of the measured signal .....up to 10 kHz.

Based on the verification technological tests carried out, it was demonstrated that the proposed system of dynamic control of the welding current of electron beam devices significantly expands the use of electron beam technologies in industrial practice.

Acknowledgements:

This work was supported by the Agency for the Support of Research and Development under contract number APVV-20-0100.

REFERENCES

[1] Schultz H.: Electron Beam Welding, Cambridge: Abingdon Publishing, England, 2004, ISBN 1-85573-050 2.

[2] Je-Ee Ho and Hong T. Young: The Analysis on Penetrating Efficiency in High-Energy Beam Drilling, Key Engineering Materials, Vol. 364-366 (2008) pp 308-314 Online: 2007-12-06, © (2008) Trans Tech Publications, Switzerland,

doi: 10.4028 / www.scientific.net / KEM.364-366.308
[3] Kolenič F., Faragula P., Maštalír P.: Modernizácia modulov elektrónového dela umiestneného vo vnútri vákuovej komora, Zvárač XIII/2016, s. 16-19, ISSN 1336-5045.
[4] Darovec R., Kolenič F., Kunštek D., Koršňák P.: A new approach to welding current modulation in electron beam welding, Procs of the International Conference "Welding technology 23, PRVÁ ZVÁRAČSKÁ a.s, Bratislava, 8. Nov 2023, ISBN 978-80-8096-298-2 https://www.pzvar.sk/id-konto/konferencia/Zbornik_Welding Technology 2023.pdf

EXAMPLES OF LASER WELDING IN INDUSTRIAL PRACTICE

Ing. Michal Šimek, PhD.[1]
Ing. František Kolenič, PhD.[2]
Ing. Tomáš Fodrek[3]
Ing. Beáta Šimeková, PhD.[4]
[1] 0000-0002-0920-9877: First Welding Company, Inc. **Slovakia**
[2] 0000-0001-9920-2398: First Welding Company, Inc. **Slovakia**
[3] 0000-0001-6534-8321: First Welding Company, Inc. **Slovakia**
[4] 0000-0002-6499-0096: Faculty of Materials Science and Technology, Slovak University of Technology **Slovakia**

Abstract: The paper presents a solution of welding technology of clutch carriers and drive disc assembly. Welding was realized on workplace equipped with a solid-state disk laser TRUMPF with power of laser beam up to 5 kW and rotary positioning equipment. Welded joints made by laser welding complied NDT as well as in terms of the integrity of welds, weld metal structure and HAZ description.

Keywords: laser welding, clutch carrier, drive disc assembly

1. INTRODUCTION

The new and constantly increasing demands of manufacturing practice drive both the quantitative and qualitative growth of advanced welding technologies in mechanical production. In the field of metallic material joining technologies, there is continuous development, influenced by both these increasing requirements and the growing demands for the technological infrastructure needed for laser technologies (Gausinger, 2005)
The clutch is part of the transmission system, and its function is to transmit torque from the engine to the gearbox, while also allowing for a short-term interruption of the torque. This interruption is essential for shifting gears and for smooth vehicle acceleration. In modern passenger cars, single-plate friction clutches are typically used. They feature a soft engagement and are controlled either by a lever mechanism directly (in older vehicles) or, more commonly today, by indirect hydraulic control. In the case of large transmitted torques, such as in trucks, dual or even triple-plate clutches are used (Kolenič et al., 2011).
The clutch carrier (Fig. 1) ensures the precise placement and holding of the clutch system on the shaft of the transmission system. The component itself contains holes for the supply of hydraulic oil.

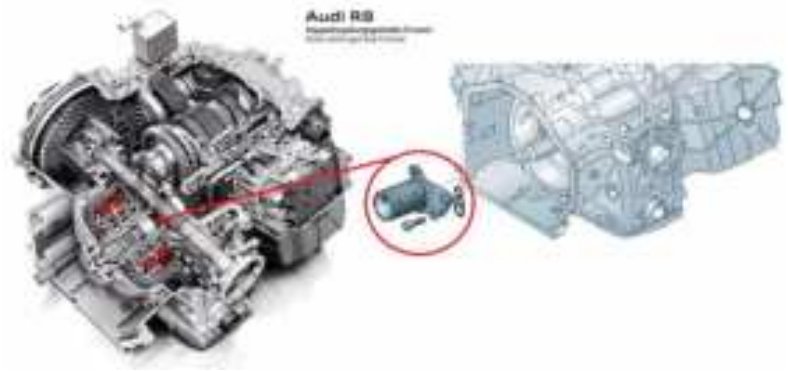

Fig. 1. The clutch carrier assembly (Kolenič et al., 2011)

The clutch disc assembly consists of a steel hub and a disc-plate (Fig. 2). Both components have several defined shapes and dimensions depending on the car manufacturer. For this reason, it is necessary to have a workstation capable of ensuring precise welding for serial production and meeting all customer requirements through the specific standards QR 83 and CQ I-15 designed for the automotive industry.

Fig. 2. Part of a car transmission 1 - steel hub, 2 – disc (https://www.zf.com/products/en/cv/products_65885.html).

2. ISSUE ADDRESSED BY LASER WELDING TECHNOLOGY

The customer's primary requirement for welding clutch carriers is that the weld surface should be raised by a maximum of 0.2mm and have a maximum depression of 0.1mm. After welding, the weld surface should be free from any spatter, and a full penetration must be present around the entire circumference.

The weld joints made on the clutch disc assembly must meet the requirements according to the standard STN EN 13919-1, acceptance level C. Before welding, the parts to be welded must be degreased in an industrial washer to ensure that no oil or contaminants are present on the surface, as they could negatively affect the quality of the weld metal.

2.1 Laser Welding Technology Procedure for Clutch Carriers

The clutch carrier consists of outer rings and flanges. The outer rings (tubes) are made of steel 16MnCr5 with the chemical composition specified in Table 1. This is a high-grade construction steel alloyed with Mn and Cr, primarily intended for carburizing, nitriding, or nitrocarburizing. The flanges are made of unalloyed steel C15E with the chemical composition outlined in Table 2.

Tab. 1 Directional chemical composition of steel 16MnCr5

Chemical composition	C	Cr	Si	Mn	P	S
Wt. %	0,14 - 0,19	0,8 - 1,1	max. 0,4	1,0 - 1,3	max. 0,025	max. 0,035

Tab. 2 Directional chemical composition of steel C15

Chemical composition	C	Cr	Ni	Si	Mn	P	S	Mo	Cu	Al
Wt. %	0,12	0,12	0,07	0,24	0,32	0,009	0,02	0,020	0,19	0,02

The exact position of the welded components during welding is ensured by a fixture (Fig. 3), which is clamped onto a rotary positioner using a three-jaw chuck.

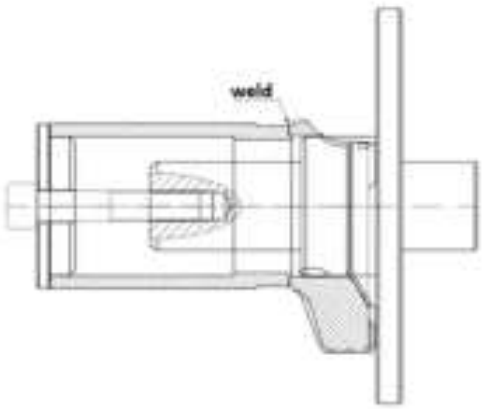

Fig. 3 The clutch carrier (flange and outer ring) placed on the fixture.

The entire welding process for clutch carriers consists of the following stages:

• Cleaning and Assembly – The surface of the supplied outer rings (tubes) and flanges is degreased with ethanol before welding. The flange is then clamped onto the fixture together with the outer ring using a screw and a spacer, which allows for the gas to be vented during welding.

• Welding – Based on technological tests, the following welding parameters were used: power 3.8 kW, welding speed 15 mm/s, and focal distance 200 mm. An important factor

affecting the quality of the welds is the precise alignment of the laser beam into the weld gap, as well as the maintenance of the rotating part within the focus of the beam.

• Post-Welding Inspection – The following quality checks are performed on the welded parts:
  - Visual inspection (each part),
  - Dimensional inspection (first piece),
  - Penetrant inspection (selected random pieces),
  - Macrostructure inspection (test samples),
  - Microstructure inspection (test samples).

2.1.1 Evaluation of Welded Parts Quality

Each welded part is evaluated in terms of the integrity and formation of the weld bead, as well as the quality of the root area of the weld. The position of the weld relative to the flange is then measured using a calibrated gauge.

During visual and penetrant testing of the weld joint on a selected random piece, no indications of defects were observed, and the welds were deemed satisfactory.

The macrostructure and microstructure of the welds on the test samples were assessed on a metallographic section after etching with 3% Nital. No internal discontinuities were observed in the weld metal, and the surface formation of the weld met the customer's requirements (Fig. 4).

Fig. 4. Macrostructure of the weld metal

The microstructure of steel 16MnCr5 (Fig. 5) is ferritic-pearlitic with a polyhedral morphology. The structure is lamellar due to prior mechanical processing. The microstructure of steel C15E (Fig. 7) is polyhedral ferritic-pearlitic with a small proportion of tertiary cementite. The microstructure of the weld metal (Fig. 6) consists of columnar ferrite crystals with the presence of acicular ferrite. Sufficient mixing of the weld metal with the base material can be observed, and the transition from the weld metal to the base material is smooth. The maximum width of the heat-affected zone (HAZ) is 1,850 µm for TOO1 and 1,400 µm for

TOO2. The microstructure of TOO1 (Fig. 5) is ferritic-pearlitic, while partial spheroidization of the pearlite occurred in TOO2.

Fig. 5. Microstructure of steel 16MnCr5 – base material (left) and HAZ1 (right)

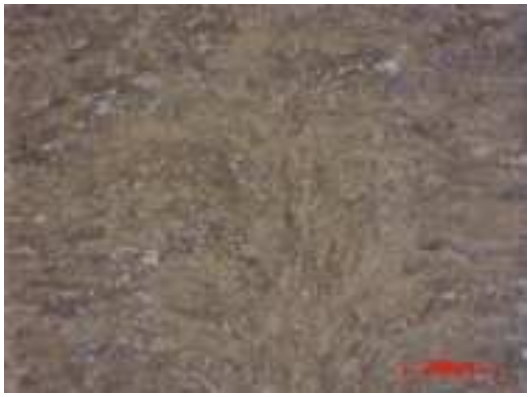

Fig. 6. Microstructure of the weld metal

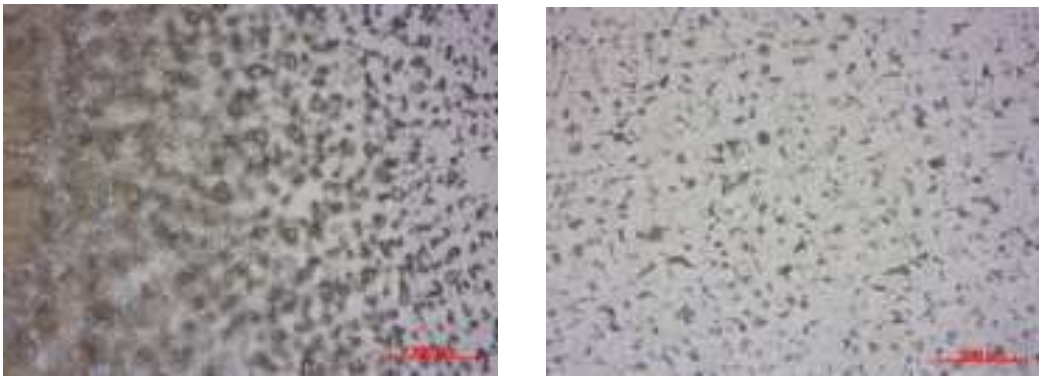

Fig. 7. Microstructure of steel C15 – HAZ2 (left) and base material (right)

2.2 Laser Welding Technology Procedure for Clutch Disc Assembly

The discs are made from carbon microalloyed steel with good cold-forming properties, with the chemical composition provided in Table 3. The hubs with internal gearing in various shapes are made from steel S355J2G3C, with the chemical composition specified in Table 4. In terms of welding technology, this involves fusion rotary welding with the laser head in a static position perpendicular to the welding axis. In this type of weld joint, the critical area is the overlap between the start and end of the weld bead. This area is prone to cracking, which can occur due to the repeated passage of the laser beam with welding power or an incorrectly chosen welding speed. A key parameter that significantly affects the overlap area is the power ramping of the laser beam. By appropriately selecting the ramping time, we can influence the laser beam's power at the critical overlap area.
Another important parameter is the precision of the rotation of the welded parts. During welding, the weld gap must align with the laser beam axis. Any misalignment can lead to a weakening of the weld strength.

Tab. 3 Indicative Chemical Composition of Steel S500MC

Chemical composition	C	Al	Si	Mn	P	S	Nb	V	Ti
Wt. %	0,12	min. 0,015	max. 0,5	1,7	max. 0,025	max. 0,015	max. 0,09	max. 0,2	max. 0,15

Tab. 4 Indicative Chemical Composition of Steel S355J2G3C

Chemical composition	C	Cr	Ni	Si	Mn	P	S	Co	Cu
Wt. %	0, 2	0,03	0,03	0,2-0,5	1,5	0,04	0,04	0,2	0,3

The exact position of the welded components during welding is ensured by a fixture (see Fig. 8), which consists of two parts (bottom and top), and is pressed together using a hydraulic unit.

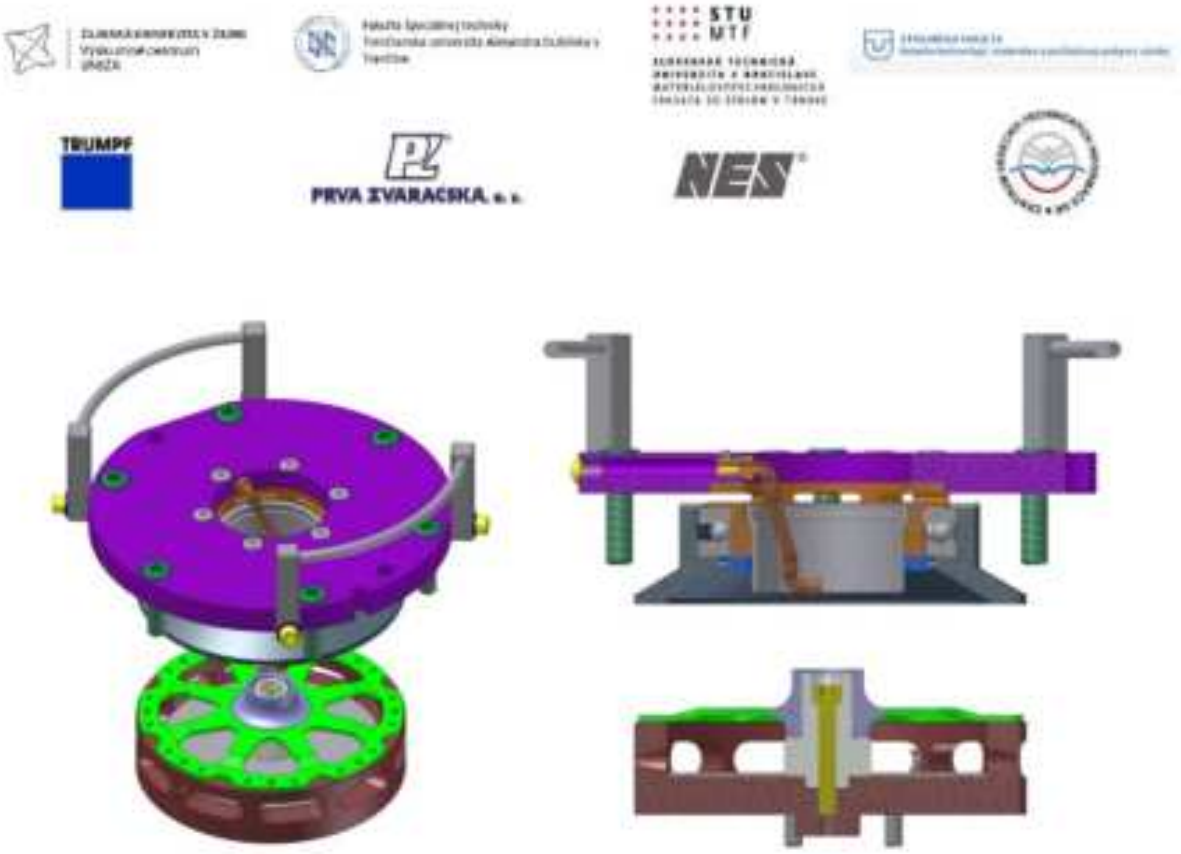

Fig. 8. Fixture for laser welding of clutch disc assemblies for automotive transmission systems

The entire welding procedure for the clutch disc assemblies consists of the following stages:

- Cleaning and Assembly – The surface of the supplied hubs and discs is chemically cleaned in an industrial washer before welding. The hub is then mounted on a centering pin on the bottom part of the fixture, together with the disc.
- Welding – Based on technological tests, the following welding parameters were used: stitch welding power 900W, welding power 3500W, stitch/welding speed 50 mm/s, and focal distance 200 mm.
- Post-Welding Inspection – The following quality checks are performed on the welded parts:
  - Visual inspection (each part),
  - Dimensional inspection (first part and every 100th part),
  - Macrostructure inspection (first part).

2.2.1 Evaluation of Welded Parts Quality

Each welded part is evaluated in terms of integrity and formation of the weld bead, as well as the quality of the root area of the weld. The height, i.e., the relative position of the disc to the hub, as well as the overall radial run-out, are measured using a mandrel and a dial gauge.
During the visual inspection of the weld joint, no indications of defects were observed, and the weld was found to be satisfactory.
The macrostructure and microstructure of the welds on the test samples were assessed on a metallographic section after etching with 3% Nital. No internal discontinuities were observed

in the weld metal, and the weld formation met the requirements according to the STN EN 13919-1 standard, acceptance level C (Fig. 9).

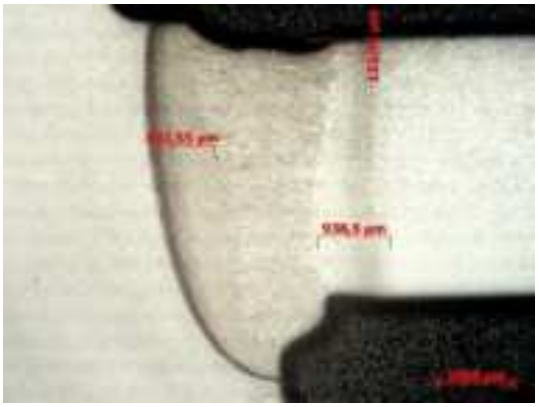

Fig. 9. Macrostructure of the weld metal

The microstructure of the base material of the disc (S500MC) is ferritic, consisting of a very fine-grained polyhedral structure with traces of coexisting pearlitic structure. Also, within the material matrix, HSLA precipitates are observed (see Fig. 10).

Fig. 10. Microstructure of base material S500MC

The microstructure of the base material of the hub (S355J2G3C) is polyhedral, consisting of a ferritic-pearlitic matrix with a distinct phase boundary. The structure shows the presence of endogenous inclusions with type II morphology (see Fig. 11).

Fig. 11. Microstructure of base material S355J2G3C

The heat-affected zone (HAZ) on the side of the S500MC material is characterized by recrystallization and subsequent grain coarsening at the fusion boundary. Due to the rapid heat dissipation, the microstructure in the overheated zone is composed of acicular ferrite with a characteristic needle-like morphology across the polyhedral grain (see Fig. 12).

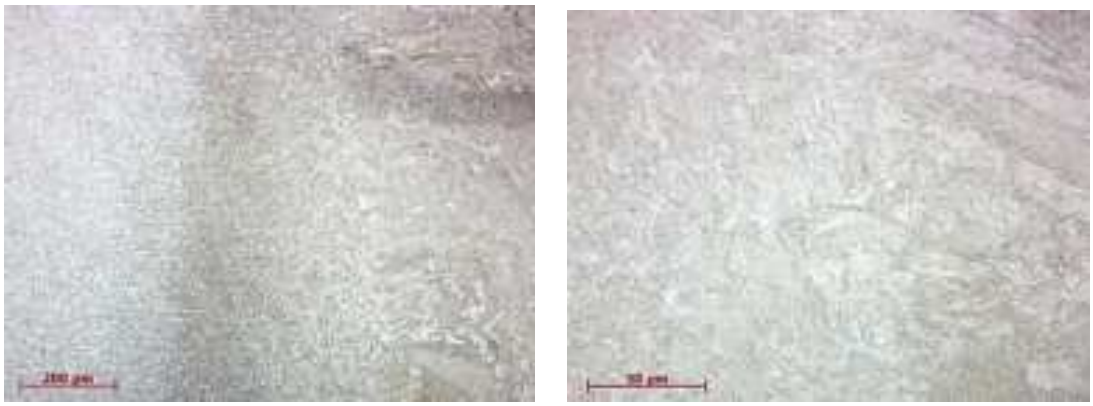

Fig. 12. Heat-affected zone (left) and fusion boundary in HAZ (right) on the side of base material S500MC

The substructure of the weld metal is characterized by the morphology of epitaxial growth toward the axis of the weld joint. The matrix consists of a columnar arrangement of ferritic phase with the occurrence of Widmanstätten structure (see Fig. 13).

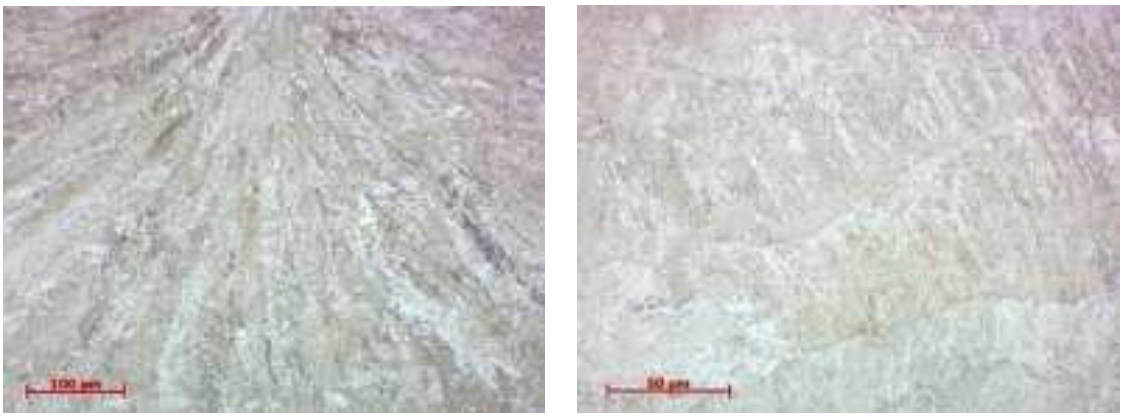

Fig. 13. Structure of the weld joint

The HAZ on the side of the S355J2G3C material, like on the side of S500MC, is characterized by recrystallization of the structure. At the fusion boundary, a bainitic transformation of the original ferritic-pearlitic structure occurs, followed by grain coarsening. The microstructure of the overheated zone is composed of a non-lamellar mixture of plate-like – lath crystals of bainite and residual austenite (see Fig. 14).

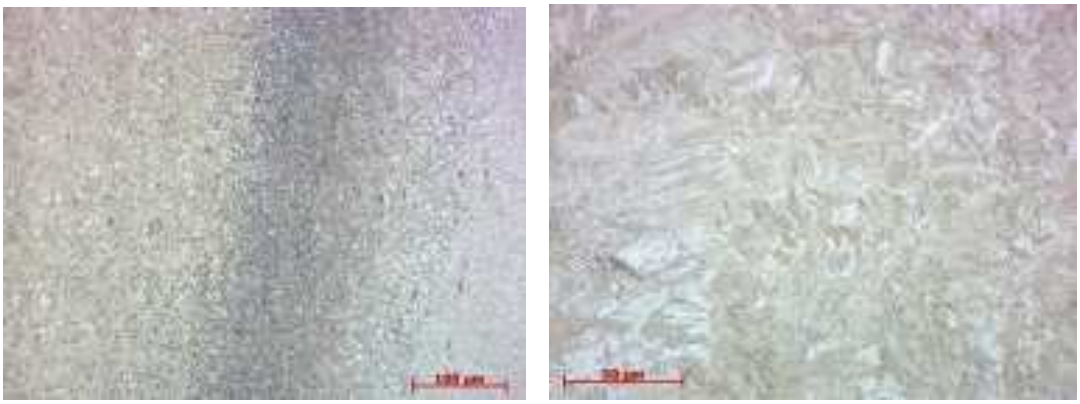

Fig. 14 The heat-affected zone (on the left) and the melting boundary in the heat-affected area (on the right) on the side of the base material S355J2G3C.

3. CONCLUSION

Currently, laser beam welding is used in almost all industrially advanced countries. This constantly evolving technology covers a wide range of material processing applications in industrial production.

In the laser welding of clutch carriers for passenger cars, all customer requirements for the final weld joints were met. This was achieved through the appropriate design of the clamping fixture as well as by fine-tuning the resulting laser welding parameters. The technology used enables productive welding with minimal heat-affected zone and complete penetration of both welded materials.

By appropriately setting the laser welding process for the clutch disc assembly, all the standards for weld joint quality required for this type of part were met. An important element in meeting quality requirements in laser welding is an accurate welding fixture as well as the welding process parameters. The designed and fine-tuned technology at the given laser workstation allows for welding the entire range of sizes and types of clutch disc assemblies, with capacity for large-scale production.
The use of a solid-state disk laser from TRUMPF for welding clutch components for passenger cars represents a suitable manufacturing technology.

ACKNOWLEDGEMENTS

This article was developed with the assistance of the research and development support agency based on contract no. APVV-0224-18 and no. APVV-0232-21.

REFERENCES

Gausinger, F.: Zváranie laserom: Súčasný stav a perspektívy rozvoja laserových zdrojov a aplikácii. In Zvárač, 2005, roč. 2, č.1, s. 16- 21. ISSN 336-5045.
Kolenič, F. - Packo, M. - ŠIMEK, M.: Štúdium vlastností návarov vytvorených diskovým laserom s prídavným materiálom vo forme drôtu. In Technológia 2011 = Technology 2011, STU, 2011, ISBN 978-80-227-3545-2.
Available at: https://www.zf.com/products/en/cv/products_65885.html
Šimek M., Kolenič F., Packo M.: Laserové zváranie spojkových nosičov pre osobné automobily, Zborník prednášok High-tech technológie 2014 – zdroj inovácií EÚ, Bratislava, November 2014, AlumniPress 2014, ISBN 978-80-8096-205-0.

STUDY OF WETTABILITY OF BI-AG-TI-(MG) – BASED SOLDERING ALLOYS ON CERAMIC SUBSTRATES SOLDERED BY LASER-ULTRASOUND TECHNOLOGY

Ing. Mikuláš Sloboda[1],
Prof. Ing. Roman Koleňák, PhD.[1],
Ing. Tomáš Gabrhel[1],
Ing. Tomáš Meluš, PhD.[1],
Ing. Peter Gogola, PhD.[1],
Ing. Ján Milde, PhD.[1],
Ing. Michal Šimek, PhD.[2]

[1]Slovak Technical University Bratislava, Faculty of Materials and Technology Trnava, Jána Bottu No. 2781/25, 917 24 Trnava, **Slovakia**

[2]THE FIRST WELDING COMPANY, Inc., Kopčianska 14, 851 01 Bratislava, **Slovakia**

Abstract
The research deals with the study of Bi-Ag-Ti and Bi-Ag-Ti-Mg – based soldering alloys destined for soldering the ceramic materials as Al_2O_3, SiC and AlN by use of combined laser-ultrasound soldering technology. The BiAg11Ti3 solder with the melting point of 402 °C is formed of bismuth matrix with silver lamellas. In the case of BiAg11Ti1.5Mg1 solder, with melting point of 437 °C, the solder matrix is formed of pure bismuth, where also the islands of binary eutectics (Ag)+(Bi) with silver lamellas appeared irregularly. In the case of joints fabricated by the use of BiAg11Ti1.5Mg1 solder, the effect of alloying elements was exerted by formation of intermetallic phases and Mg distribution to substrates. These findings suggest that the alloying elements have met their purpose and contributed thus to bond formation in both cases. The measurements of contact angles suggest that the more suitable seems to be the BiAg11Ti1.5Mg1 solder. The best average contact angle of wettability was obtained in case of Al_2O_3/BiAg11Ti1.5Mg1 combination, (48°) – assessed as good wettability. The remaining combinations have attained acceptable quality of wettability, while the average values varied within the interval from 50° to 70°.

Keywords: Electron beam soldering, BiAg11Ti3, BiAg11Ti1,5Mg1,

1. INTRODUCTION

Soldering is the most widely used technology of joining semiconductor and ceramic materials with the conductive and non-conductive materials. Ever more attention is at present devoted to ultrasonic soldering of ceramic materials without flux application [1]. That is proved also by increasing number of studies dealing with soldering of SiC, AlN and Al_2O_3 [2,3 and 4] materials.

The electronic industry is just one of the most rapidly developing industries, where the tendency to miniaturize the electronic parts is ever more observed, together with efforts to manufacture them as environmentally friendly as possible and economically most favourably for the manufacturer [5]. Those parts are during their entire working cycle thermally and mechanically loaded, what naturally necessitates the development of new materials capable to meet these requirements [6].

Just these Bi-Ag soldering alloys belong to the group of solders for higher application temperatures. This technology becomes ever more frequently used technology, owing to the irreplaceable properties of final products, namely very good thermal conductivity and high reliability [7]. Application of these soldering alloys is oriented not only to the field of packaging technologies but also for the optical components, modules and soldering in the automotive and aviation industries [8].

The eutectic Bi-Ag system provides suitable melting point [265 °C at 2.5 wt. %] and acceptable price [9]. It was at the same time proved, that at addition of 11 wt. % Ag to soldering alloys, an increase of thermal conductivity takes place [10].
Ultrasonic soldering is mostly used for soldering hard-to-wet parent metals. Just ultrasound assistance causes the formation of cavitation bubbles in the molten solder, whereby the zones with high temperature and pressure occur, removing the surface oxide layer and improving thus the wettability of parent materials [11].

The Bi-Ag-Ti-(Mg) - based soldering alloys used in this study are destined for higher application temperatures. The task of magnesium and titanium, contained in the solder as alloying additions, is to wet the ceramic materials as Al_2O_3, AlN and SiC. The study deals with assessing the effect of these elements on the joint properties and mutual interactions of elements.

2. EXPERIMENTAL

The substrates of ceramic materials studied in this work were in the shape of disk with dimension Φ 15 x 3 mm. Within preparation of soldering process,these substrates were first degreased and the soldering alloy in form of a cube in dimensions 4 x 4 mm was laid on their surface.
The soldering alloys used in this study are based on Bi-Ag-Ti and Bi-Ag-Ti-Mg, whereas their chemical composition is given in Table 1. The task of alloying elements used in these alloys is to improve the wettability of ceramic substrates and mutual interactions between the solder and parent material. The actual proportion of individual elements contained in the soldering alloys was determined by the ICP- AES analysis.

Tab. 1: Chemical composition of soldering alloys

Soldering alloy	Chemical composition [wt. %]
BiAg11Ti3	80,4% Bi, 16,9% Ag, 2,68% Ti
BiAgTi1.5Mg1	85,0 % Bi, 12,0% Ag, 1,21% Ti, 1,87% Mg

For preparation of wettability specimens the equipment for laser soldering type TRUMPF TruDisk 5001 and the ultrasonic equipment type HANUZ UZPE2 were used. The digitalised scheme of the workplace, on which these equipments were employed is shown in Fig. 1. The working parameters of both equipments are given in Table 2.

Tab. 2: Working parameters of equipments used

Laser soldering device TRUMPF TruDisk 5001	Working parameters
Power	750 W
Laser wavelength	1,03 µm
Beam diameter	2,5 mm
Ultrasonic generator HANUZ UZPE2	
Work frequency	40 kHz
Sonotrode diameter	3 mm
Protective atmosphere - Argon	25 l/min

Fig 1 Digitalisation of the workplace

Soldering procedure consisted of laying a graphite jig (destined for indirect heating of substrate by laser beam) on working table, followed by installation of a thermocouple and supply of argon to the jig. An ultrasonic sonotrode was mounted on the working table and laser beam, performing the circular motion on the jig surface, was set. Laser beam thus acted on a circular area, by what the heating in joint zone within the temperature interval of 400-500 °C was achieved.

The metallographic preparation consisted of grinding, polishing and etching. The specimens were ground on the emery papers with the grain size of 240, 600 and 1000 grains/cm^2. Polishing was performed by the diamond emulsions with the grain size of 15, 8 and 3 μm. Two types of etchants were used for the polished specimens. The first one for the solder type BiAg11Ti1,5Mg1: 2ml HCl, 5ml HNO_3 and 93 ml methanol and the second for the solder type BiAg11Ti3: 10ml HF 10ml H_2O_2 and 40ml H_2O.

3. RESULTS OF EXPERIMENT

The DTA analysis served for determination of melting point of soldering alloys. It resulted in DTA curve. The BiAg11Ti1.5Mg1 solder (Fig. 2) exerts the melting point of 437 °C. The thermal interval of 263 °C, recorded by DTA analysis, corresponds to an eutectic reaction. The alloy matrix was formed of pure bismuth, where the islands of binary eutectics (Ag)+(Bi) with silver lamellas have irregularly appeared. In the case of first heating, gradual dissolution of Ag-Mg-Bi and Ti_8Bi_9 phases occurred. In the case of BiAg11Ti3 alloy (Fig. 3), Ag lamellas in Bi matrix were formed by eutectic reaction at the temperature of 264 °C. The liquidus temperature of 402 °C corresponds to binary diagram of Ag-Bi.

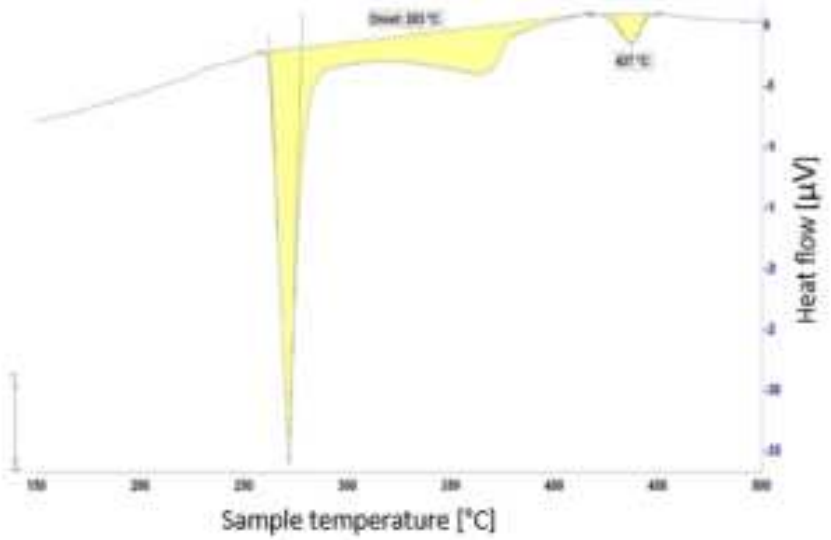

Fig. 2: DTA analysis of BiAg11Ti1.5Mg1 solder

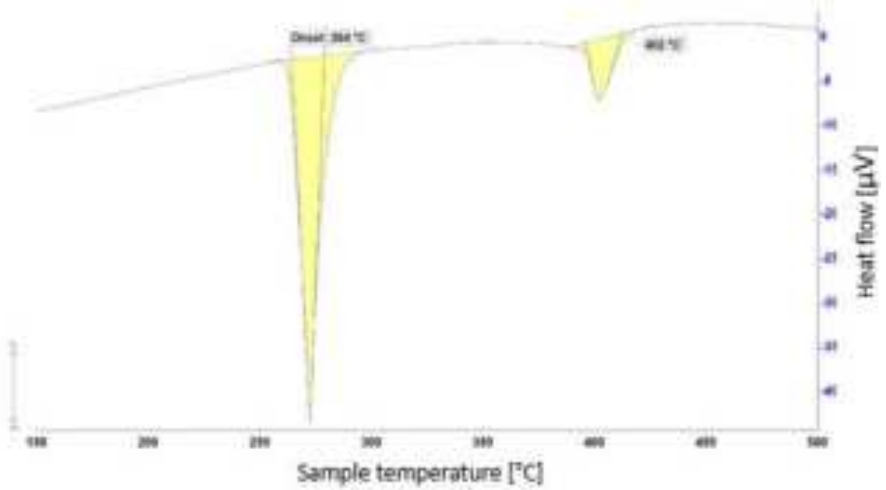

Fig. 3: DTA analysis of BiAg11Ti3 solder

Mechanical tensile test served for determination of mechanical properties of soldering alloys and their mutual comparison. The test pieces 4 mm in thickness were prepared. Three specimens for each solder were used at the loading rate of 1 mm/min. The results suggest that magnesium addition affects the strength improvement. The BiAg11Ti1.5Mg1 alloy can be therefore considered for more suitable, owing to its capability to resist heavier loadings.

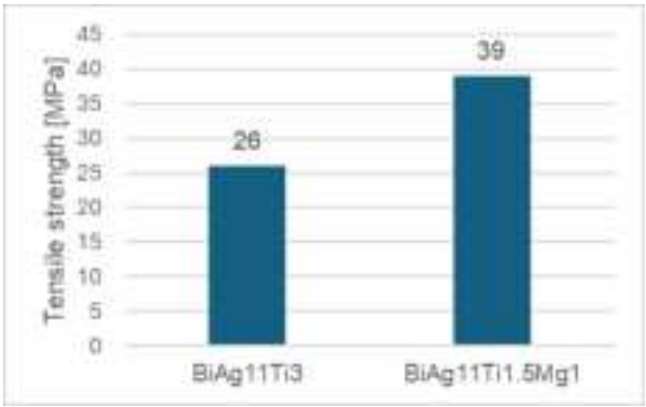

Fig. 4 Tensile strength of soldering alloys

The wettability of substrates was determined by application the technology of optical scanning on the equipment type GOM Atos Triple scan with measuring volume of MV100 and 5 MPx resolution. Since a non-destructive technique is concerned, it is possible virtually cut the 3D model of specimen to arbitrary number of cross sections, and to determine thus the average value of wettability angle on a given specimen, what may be considered for a priority, compared to the customary goniometric technique. The individual specimens were scanned and their images could be virtually cut three times, what allowed to determine the average value of wettability angle on an actual substrate, based on three measurements.

The determined average wettability angles are represented in the graphs for both solders, as shown in Figs. 5 and 6.

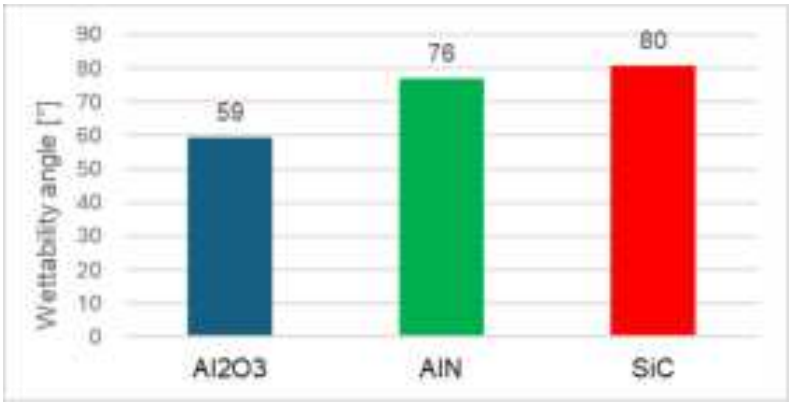

Fig. 4 Average value of wettability angles in case of BiAg11Ti3 solder

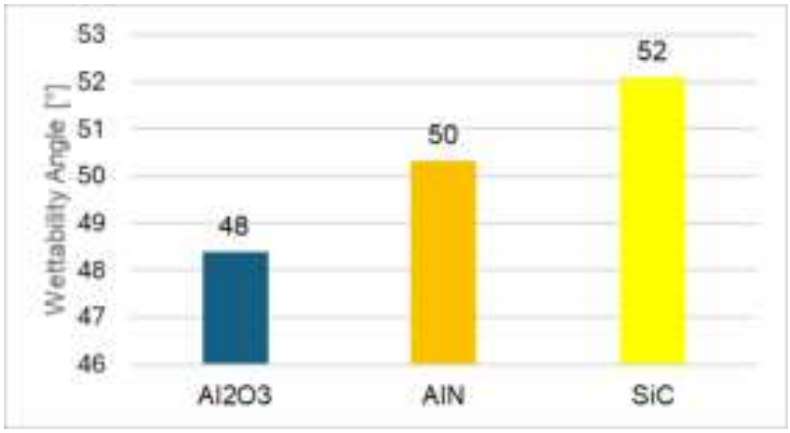

Fig. 5 Average value of wettability angles in case of BiAg11Ti1.5Mg1 solder

Based on these measurements, it may be concluded that the best value was achieved with the Al_2O_3 substrate wetted by BiAg11Ti1.5Mg1 solder (48°). The obtained value can be at the same time assessed as a good wettability. The measured values suggest that the BiAg11Ti1.5Mg1 solder has provided better results on all three ceramic substrates. On the other hand, it can be concluded that the SiC substrate and BiAg11Ti3 solder was the worst combination, in spite of the fact that the value of 80° corresponds to quality criterion as acceptable. It may be finally stated that all the remaining combinations offer acceptable quality of wettability. This part of study also suggests, that the solder alloyed with magnesium wets better the ceramic materials and therefore it is more suitable for appropriate applications. It may be also stated, that owing to reaction of active elements in soldering alloys, the wetting of ceramic substrates takes place.

The mutual interactions of soldering alloys and ceramic substrates were studied by microscopic analysis oriented to determination of effects of alloying elements in the solder on bond formation.

The colour map of Al_2O_3/BiAg11Ti1.5Mg1 boundary presents the distribution of Mg and Al across the boundary, what proves the positive reaction between the solder and substrate. In this case, formation of Ag islands is observed also in the vicinity of joint boundary, suggesting the mixture Bi+Ag+Mg phases. Titanium also in this case does not exert visible effect on joint boundary formation, in spite of the fact that it is partially distributed to boundary zone.

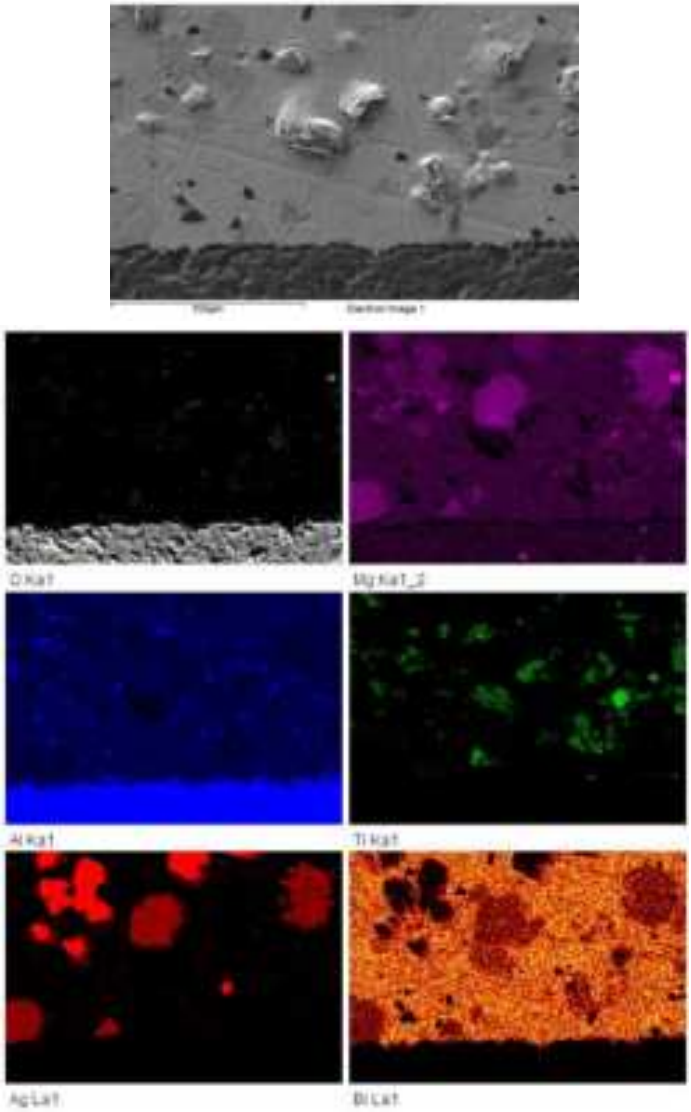

Fig. 6 Colour map of Al_2O_3/BiAg11Ti1.5Mg1 boundary

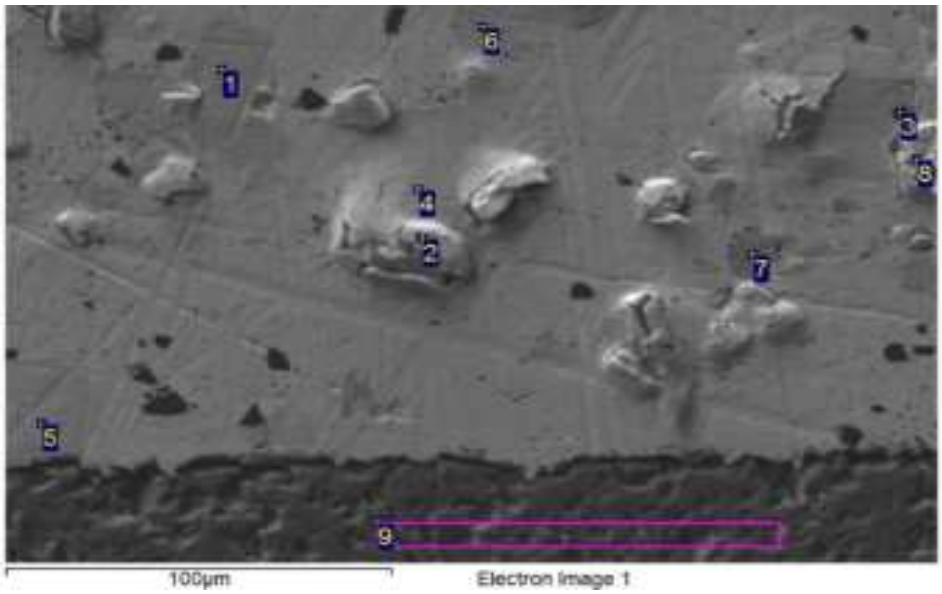

Fig. 7 Point analysis of Al_2O_3/BiAg11Ti1.5Mg1 boundary

Tab. 3: Result of point analysis in Al_2O_3/BiAg11Ti1.5Mg1 boundary

Spectrum	Mg [at.%]	Al [at.%]	Ti [at.%]	Ag [at.%]	Bi [at.%]	
1	12,07	2,31	0	84,08	1,54	Two-phase region (Ag) + $MgAg_3$
2	2,23	1,23	41,51	3,02	52	Ti_2Bi_3
3	95,85	0,46	0,88	0,41	2,39	High content of Mg with slightly dissolved Al, Ti, Ag a Bi.
4	25,05	0,66	0	44,46	29,84	$Mg_5Bi_6Ag_9$
5	24,05	0,76	0	46,09	29,1	$Mg(Bi,Ag)_3$,
6	11,03	11,03	0	76,37	1,56	$(Al,Mg)Ag_3$
7	6,68	1,88	70,89	0,86	19,69	Ti_3Bi
8	0	0	41,8	0	58,2	Ti_2Bi_3
9	0,48	98,89	0	0,63	0	Al_2O_3 substrate

The point analysis suggests that segregation of parent metal to solder zone has occurred in Al_2O_3/BiAg11Ti3 boundary, what is proved by Spectrum 3, similarly as Spectrum 6. The analysis additionally detects the formation of $Mg_5Bi_6Ag_9$ phases in Spectrum 4 and also Ti_3Bi and Ti_2Bi_3 phases (Spectrum 2, 7 and 8), which correspond with the binary diagrams of these systems.

4. CONCLUSIONS

The aim of this contribution was to assess the wettability and mutual interactions of AlN, SiC and Al_2O_3 substrates soldered with the solders type BiAg11Ti3 and BiAg11Ti1.5Mg1 applied for higher application temperatures. These solders belong to the group destined for higher application temperatures and are applied in power semiconductor devices.
Via DTA analyses, the melting points and reactions in soldering alloys during their heating were determined. The BiAg11Ti3 solder attains the melting point at 402 °C, what corresponds to binary diagram Ag-Bi and at the temperature of 264 °C the formation of Ag lamellas in Bi matrix takes place. In the case of BiAg11Ti1.5Mg1 solder, its melting takes place at 437 °C, while the matrix of this older is formed of pure Bi with irregularly appearing binary eutectics (Ag) + (Bi).

The tensile test of solders has revealed the tensile strength of BiAg11Ti3 solder in the value of 29 MPa and in the case of BiAg11Ti1.5Mg1 solder it was 39 MPa.

The assessment of wettability angles has shown that the best combination of soldered materials is Al_2O_3/BiAg11Ti1.5Mg1 with the value of 48°, classified as a good wettability. The mutual comparison suggests that the solder alloyed with Mg is more suitable for these applications, since it wets the ceramic substrates demonstrably better. The combination of SiC/BiAg11Ti3 with the value of 80° was the worst case, what however still corresponds to acceptable wettability. All the remaining material combinations have also attained acceptable wettability within the range of 50°-70°.

From the analysis of Al_2O_3/BiAg11Ti1.5Mg1 specimen it may be concluded that the alloying elements have met their purpose and they sufficiently wetted the parent materials. The microstructure of Al_2O_3/solder combination reveals the distribution of Mg and Al across the boundary, indicating thus positive reaction with substrate and in that case the Ag islands were observed in the vicinity of joint boundary. The point analysis has shown that formation of Ti_2Bi_3 and Ti_3Bi phases takes place in the solder zone, what is proved also by the binary diagrams of these systems, and also formation of zones with high Mg content and dissolved Al, Ti, Ag and Bi elements was observed. The study of soldering the ceramic SiC, AlN and Al_2O_3 materials by a combined laser-ultrasound technology with use of Bi-Ag-Ti-(Mg) – based solders has proved the suitability of this combination of soldering technologies and soldered materials for the application in electro-technical industry.

ACKNOWLEDGMENTS
This work was supported by the Slovak Research and Development Agency under the contract no. APVV-21-0054 and no. APVV-17-0025. The paper was also prepared with the support of VEGA 1/0237/24: Research of active soldering alloys filled with ceramic material nanoparticles, and VEGA 1/0026/23: Modification of the structure and mechanical properties

of soldering alloys to increase the reliability of soldered joints in advanced electronic applications.

REFERENCES

1 HU, F. Q.; ZHANG, Q. K.; JIANG, J. J., SONG, Z. L. Influences of Ag addition to Sn-58Bi solder on SnBi/Cu interfacial reaction, *Materials Letters* **2018**, 214,142-145, ISSN 0169-577X [https://doi.org/10.1016/j.matlet.2017.11.127]

2 ZHAO, D.; ZHAO CH.; XIU, Z.; YAN, J. Ultrasonic-assisted soldering of SiC ceramice and aluminum alloy with commercial inactive Sn3.0Ag0.5Cu solder, *Materials Science and Engineering* **2024**, 889, 145833, ISSN 0921-5093 [https://doi.org/10.1016/j.msea.2023.145833]

3 FAN, Z.; CHEN, CH. Microstructure, joining mechanism, mechanical properties and optimization of inactive solder (Sn9Zn) in low temperatureultrasonic soldering of AlN ceramics and 2024Al, *Ceramics International* **2024**, ISSN 0272-8842 [https://doi.org/10.1016/j.ceramint.2024.08.157]

4 GORJAN, L.; BLUGAN, G.; et. al. Fracture behavior of soldered Al_2O_3 ceramic to A356 aluminum alloy and resistance of the joint to low temperature exposure, *Marterials & Design* **2015**, 88, 889-896, ISSN 0264-1275 [https://doi.org/10.1016/j.matdes.2015.09.067]

5 ISLAM, M.N.; CHAN, Y.C.; RIZVI, M.J.; JILLEK, W. Investigation of interfacial reactions of Sn-Zn based and Sn-Ag-Cu lead-free solder alloys as replacement for Sn-Pb solder, *Journal of Alloys and Compounds* **2005**, 136-144, ISSN 0925-8388 [https://doi.org/10.1016/j.jallcom.2005.03.053]

6 BERGER, R.; SCHWERZ, R.; ROLLIG, M.; HEUER, H. Influence analysis of joint attributes on the fatigue progress of SnAgCu solder joints under thermomechanical loading, *Microelectronics Reliability* **2023**, 140, 114870, ISSN 0026-2714 [https://doi.org/10.1016/j.microrel.2022.114870]

7 SPINELLI, J.E.; SILVA B.L.; GARCIA, A. Microstructure, phases morphologies and hardness of Bi-Ag eutectic alloy for high temperature applications, *Materials & Design* **2014**, 482-490, ISSN 0261-3069 [https://doi.org/10.1016/j.matdes.2014.02.026]

8 KOLEŇÁK, R.; HODÚLOVÁ, E. Study of direct soldering of Al_2O_3 ceramics and Cu substrate by use of Bi11Ag2La solder, *Weld World* **2018**, 62, 415-426 [https://doi.org/10.1007/s40194-017-0538-6]

9 SONG, JM.; CHUANG, HY.; WU, ZM. Interfacial reactions between Bi-Ag high-temperature solders and metallic substrates, *J. Electron. Mater.* **2006**, 35, 1041-1049 [https://doi.org/10.1007/BF02692565]

10 SONG, J.; TSAI, CH.; FU, Y. Electrochemical corrosion behaviour of Bi-11Ag alloy for electronic packaging applications, *Corrosion Science* **2010**, 52, 2579-2524, ISSN 0010-938X [https://doi.org/10.1016/j.corsci.2010.03.031]

11 LI, Z.; XU, Z.; REN B.; YAN, J. Fast low-temperature ultrasonically soldering porous Si3N4 ceramics in the air, *Ceramics International* **2022**, 48, 5663-5673, ISSN 0272-8842 [https://doi.org/10.1016/j.ceramint.2021.11.111]

POSSIBILITIES OF IMPLEMENTING LSP TECHNOLOGY TO IMPROVE ESSENTIAL SURFACE INTEGRITY INDICATORS ON MATERIALS FOR AUTOMOTIVE INDUSTRY

Doc. Ing. Michal Šajgalík, PhD.[1]
Ing. Tatiana Czánová, PhD.[2]
Ing. Jozef Holubják, PhD.[3]
Ing. Richard Joch, PhD.[4]
Ing. Miroslav Cedzo, PhD.[5]
Ing. Miroslav Matuš[6]
Ing. Martin Kasenčák, PhD.[7]

[1]ORCID: 0000-0002-4908-1046, Dpt. Of Machining and Production Technologies, Faculty of Mechanical Engineering, University of Žilina, Univerzitná 8215/1, 010 26 Žilina **Slovakia**
[2]ORCID: 0000-0002-6943-6393, Dpt. Of Machining and Production Technologies, Faculty of Mechanical Engineering, University of Žilina, Univerzitná 8215/1, 010 26 Žilina **Slovakia**
[3]ORCID: 0000-0003-3226-9445, Dpt. Of Machining and Production Technologies, Faculty of Mechanical Engineering, University of Žilina, Univerzitná 8215/1, 010 26 Žilina **Slovakia**
[4]ORCID: 0000-0002-9937-0057, Dpt. Of Machining and Production Technologies, Faculty of Mechanical Engineering, University of Žilina, Univerzitná 8215/1, 010 26 Žilina **Slovakia**
[5]ORCID: 0000-0002-1872-0925, Dpt. Of Machining and Production Technologies, Faculty of Mechanical Engineering, University of Žilina, Univerzitná 8215/1, 010 26 Žilina **Slovakia**
[6]ORCID: 0009-0002-9214-8696, Dpt. Of Machining and Production Technologies, Faculty of Mechanical Engineering, University of Žilina, Univerzitná 8215/1, 010 26 Žilina **Slovakia**
[7]ORCID: 0000-0003-4606-6411, FIRST WELDING COMPANY - PRVÁ ZVÁRAČSKÁ, a. s., Kopčianska 14, 851 01 Bratislava, **Slovakia**

Abstract: Each manufacturing technology that is currently used to produce various components leaves a mechanical influence in the surface layers in the form of residual stresses. The nature and magnitude of these residual stresses are a consequence of both mechanical and thermal loading and affect the functional properties of each individual component. Current trends in engineering production, especially automotive, aerospace, etc., emphasise materials with specific properties when using high-performance technologies. In the case of machining, these technologies are characterised by high force and temperature loads, which are generated in the cutting zone and affect the tool, but above all the machined surface. For welding technologies, the temperature influence is a necessity, however, its distribution in the TOO region and the gradient towards the unaffected material often generates a non-equilibrium state of the component structure. Therefore, all the above-mentioned processes need to be monitored, especially with regard to qualitative indicators of surface integrity, but also functional properties. The aim of this research was to investigate how advanced surface hardening technology can be used through laser application and its effect on surface integrity. The experiments presented in this paper describe the

measurements of surface integrity indicators and identify the possibilities of positively influencing the surface after turning.
Keywords: machining, surface integrity, laser shock peening

1. INTRODUCTION

The current automotive industry and related industries use a wide range of materials whose mechanical properties require the application of productive technologies with specific approaches. This includes various machining technologies, additive and also welding technologies. Machining technologies, among others, are characterized by high force effects on the machined material. And together with welding technologies, processes in which heat is generated. These phenomena, by their character, can have both a positive and a negative effect on the integrity of the surface. (Al-Ghamdi&Iqbal, 2015; Hoffman et. al, 2003, Whitenton et. al, 2008; Kozový et al., 2024)

The surface of the component thus represents a critical interface between the material and the environment, which significantly influences its functional properties and service life. According to Davim, the surface separates the internal structure of the material from external influences, and its condition and quality directly affect the overall reliability of the component. (Davim et. al, 2010) Ganev further develops this idea and defines surface integrity as a complex set of properties that influence the functional behavior of surface layers. These properties are often the result of technological processes and have a direct impact on the functionality and durability of the component under operating conditions. (Ganev et. al, 2013)

It can most often be evaluated by three basic indicators: white layer formation, metrological characteristics (mainly surface roughness) and residual stresses. (Jawahir et. al, 2018)

Current trends in surface integrity assessment focus on so-called non-destructive approaches, hence the paper itself focuses mainly on geometric characteristics and residual stresses in its analysis.

To improve these properties, we can use various methods of strengthening primarily based on mechanical contact influence of surface. The first method is to reinforce the surface during the machining process. This can be achieved by appropriate tool geometry. Independent research has shown that if the rake angle is close to zero, or negative, or if a wiper is located on the clearance surface (angle), it is possible to achieve surface hardening during the machining process. Similar results have been found when investigating the effect of cutting edge radius (in conjunction with depth of cut) or by adjusting the conditions during high-shear machining. (Kozový et al, 2023; Petru et al., 2018, Xu et al., 2020)

In a real production process, however, it is not always possible to use the adjustment of tool geometry and cutting conditions in this way. This is where additional surface hardening comes in. For this purpose, it is suitable to use the rolling, with the possibility of adjusting the tool pressure. For shape-complex components, the shot peening method has also proven its

worth. In both cases it is possible to achieve the desired changes in surface hardening while respecting the surface roughness and geometry requirements of the component. (Bumbálek et al., 1991; Qiang et al. 2018, Slabejová, et al. 2023)

The above-mentioned surface hardening technologies impose requirements for special tools, the use of suitable hardening material, etc. Thus, the implementation is subject to various limitations caused by the substance of the technology. Laser shock peening (LSP) technology appears to be a promising technology that has some versatility.

1.1. LASER SHOCK PEENING

Laser shock peening is based on generating of high amount of energy, when the laser beam hits the surface.

The first experiments using pulsed laser on the surface of a material were performed at the Battelle Institute (Columbus, OH, USA) in 1968 (Montross, 2006; Peyre, 1995). By 1981, research work was then carried out on aluminium alloys and steels for aerospace applications. Subsequently, experiments were carried out in the laboratories of the European institutes CLFA (Cooperation Laser Franco-Allemande-Arcueil Cedex), LALP (Laboratoire d'Application des Lasers de Puissance-Arcueil Cedex) and LULI (Laboratoire d'utilisation des Lasers Intenses-Ecole Polytechnique, Palaiseau cedex), for the sake of further research on the applicability of the LSP process in industry (Montross, 2006).

LSP is a mechanical process (cold forming) in which laser pulses (high energy) strike a surface and shock waves are generated (Fig. 1). These waves plastically deform the surface and compressive stresses are transmitted to the layers below the surface. These dynamic stresses are highest at the surface of the component thus treated and decrease towards the material (Zhang, 2010; Clauer, 2019).

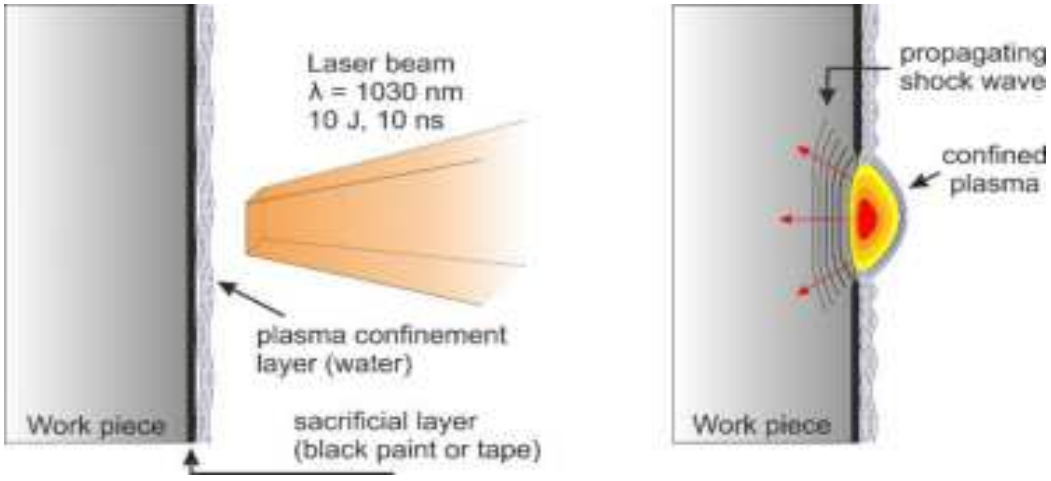

Fig. 1. Principle of laser shock peening (Brajer, 2018)

Several requirements must be met for the laser to generate a shock wave. The most important one is that the target surface is covered with an absorptive coating that is intended to be removed - ablation (ablation occurs only from the absorptive layer). This layer is vaporized by the laser and a plasma is generated on the surface, thus creating pressure during and shortly after the laser exposure. The absorption layer prevents melting and laser ablation of the base material, thus maintaining a high surface quality. The technology can also be used without an absorber layer, but there is no effective conversion of the laser energy into a shock wave passing through the material and the surface of the material shows signs of plasma damage (Hong, 1998)

The effectiveness of Laser Shock peening is dependent on the material of the component being processed, the laser parameters and the properties of the absorber and sealing layer.

The duration of the shock wave pressure (laser pulse length) typically ranges from 10 to 100ns with an energy of 1 to 10J in pulses and the spot size (diameter of the area of the component surface hit by the laser beam) is 1 to 6 mm. The beam profile can be circular, elliptical, rectangular, polygonal, but the use of a square shape has been found to be the best, showing better uniformity of intensity and a good possibility of overlapping individual pulses. The use of frequencies below 1kHz and power intensities well in the range of 0.1 up to 106 GW.cm^2 (depending on the application of the technology) is required. Typical process parameters are radiant flux density I_e (intensity), pulse length t, absorber layer and transparent overlay. The choice of processing parameters is solely limited to the laser type, substrate condition and target applications. Based on the results of various research institutions, a database with parameters for the processing of common metals and their alloys by laser shock peening has been developed by the Society of Automotive Engineers (SAE)

(Clauer, 2019, Sakhvadze 2019)

The LSP technique also changes the surface roughness of the processed material. The measurement of surface roughness after LSP is carried out by means of surface evaluations, either by contact through roughness meters or by non-contact methods based on the principle of optics. Increased surface roughness may indicate the appearance of stress concentration areas and incipient cracks, which adversely affect the fatigue life of the components. Similarly, the microhardness and nanohardness of the machined surface is also measured. The increase in measured hardness is attributed to plastic deformation, leading to multiplication and movement of dislocations. All these techniques convey insight into the changes occurring in the material after LSP processing. The general improvement can then be further quantified after a series of mechanical tests depending on the type of application. These tests include fatigue resistance, wear resistance, stress corrosion and cavitation resistance. The effect of the LSP process can have beneficial effects on residual stress history, microstructure, mechanical properties, and corrosion resistance. (Sakhvadze 2019; Zhang, 2010; Martinez 2003; Cao, 2011; Ruschau, 1999).

3. MATERIALS AND METHODOLOGY OF EXPERIMENTS

The main target of presented experiments was the analysis of changes in geometrical characteristics, surface roughness and residual stress. As an initial measurement, there was chosen C45E steel for measurements. This kind of steel is usable for construction materials in usual atmospheric conditions. It is suitable for welding, refining and hardening. It is also used in construction of machines and in automotive industry.
The next examined material was 42CrMo4 steel. It is steel suitable for automotive components, especially shafts, piston rods and other large and medium-sized mechanical parts with high strength, toughness and hardenability.

Table 1
Chemical composition of C45E and 42CrMo4 steel (%)

C45E steel	**C**	**Si**	**Mn**	**Mo**	**Ni**	**Cr**	**Co**
	0,45	0,3	0,6	0,08	0,2	0,3	0,037
42CrMo4 steel	**C**	**Si**	**Mn**	**Mo**	**Ni**	**Cr**	**Cu**
	0,42	0,2	0,76	0,19	0,16	1,07	0,22

Table 2
Mechanical properties of C45E

Material\Parameter	**Yield strength**	**Elastic Limit**	**Hardness**
C45E steel	350 MPa	560 MPa	22 HRC
42CrMo4 steel	500 MPa	920 MPa	38 HRC

For turning, there was used 3-axes CNC lathe Hurco MT8. The used cutting tool was tool holder with indexable cutting insert DCMT 11 T3 08-LF 4225. Initial cutting conditions were based on used material and CNC lathe. They are suitable for both types of materials.
The first part of the samples was prepared by turning, creating 6 different surfaces on the surface. Each surface represented different cutting conditions or combinations (v_c=100-160m.min^{-1}; f_n=0,05-0,1mm; a_p=1mm). In this way, various conditions that are commonly encountered in real production conditions when creating functional surfaces were simulated.
During the experiments, there were measured: geometrical deviations of shape (roundness), surface roughness and residual stress. Zeiss Eclipse, the 3D measuring device was used for measuring of geometrical deviations. Alicona Infinite Focus G4 was used for surface roughness analysis and Proto XRD, the X-ray diffractometer was used for analysis of residual stress.
For application of LSP, there was used special device developed by CVUT Praha and HiLASE company. (Rostohar, 2018)
All measurements were performed after machining and after application of LSP.

4. RESULTS

Before LSP application, there were measurement geometrical characteristics on the samples: diameter and roundness. Nominal value was 66mm for both materials. Nominal value for roundness was not defined, only the measured values were compared.
In the Fig. 2, there are shown differences from nominal value for both materials.
Expect of Sample 1 (C45E) all differences are negative. It is possible to see that higher differences were on material 46CrMo4. In the Fig. 3, there are values of roundness. Better values are identified on surfaces of C45E steel. It can be caused by worse machinability against to C45E.

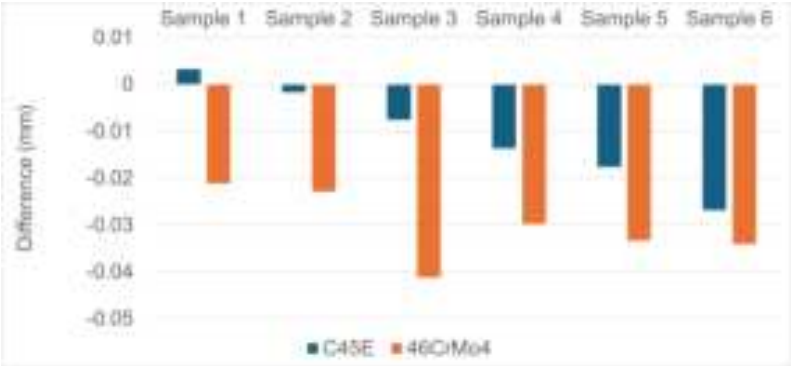

Fig. 2. Deviations from nominal value after machining (units: mm)

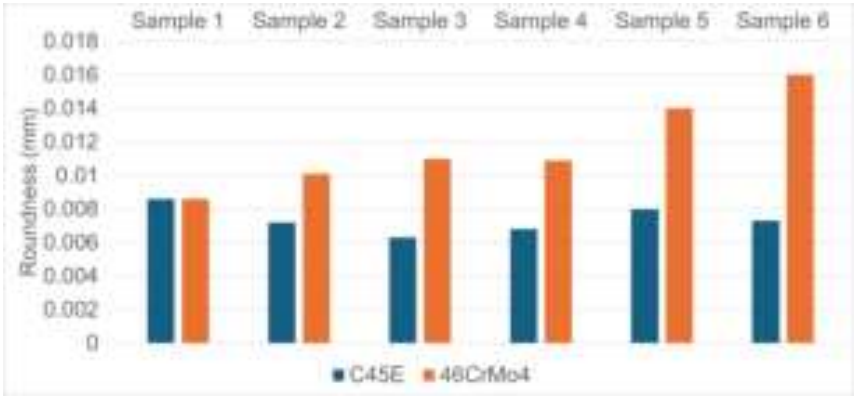

Fig. 3. Roundness of samples after machining (units: mm)

There were also analysed residual stress (Table 3). Measurements were performed in the direction of cutting tool feed, on three regular angle positions. Analysis of residual stress was focused on surface layers (0-10μm).

Table 3
Mean values of residual stress after machining (units: MPa)

Material	C45E			42CrMo4		
Angle	0˚	120˚	240˚	0˚	120˚	240˚
Sample 1	-13.01	-12.13	-15.35	-176.58	-218.32	-166.76
Sample 2	342.93	363.86	372.96	-103.94	-121.75	-102.22
Sample 3	734.74	745.50	751.56	125.3	174.88	217.19
Sample 4	376.41	386.54	372.96	-118.74	-106.18	-153.86
Sample 5	456.4	427.05	461.18	-35.05	-69.37	3.62
Sample 6	-215.51	-201.85	-220.48	433.24	458.21	377.07

After LSP application, there were measurement same indicators (Fig. 4 and 5). The better values were observed on samples from 46CrMo6. Also, all values indicate that real diameter is lower as nominal value at all samples. Roundness was better for samples from 46CrMo4 than C45E, only for the Sample 1 was very similar (on both materials).

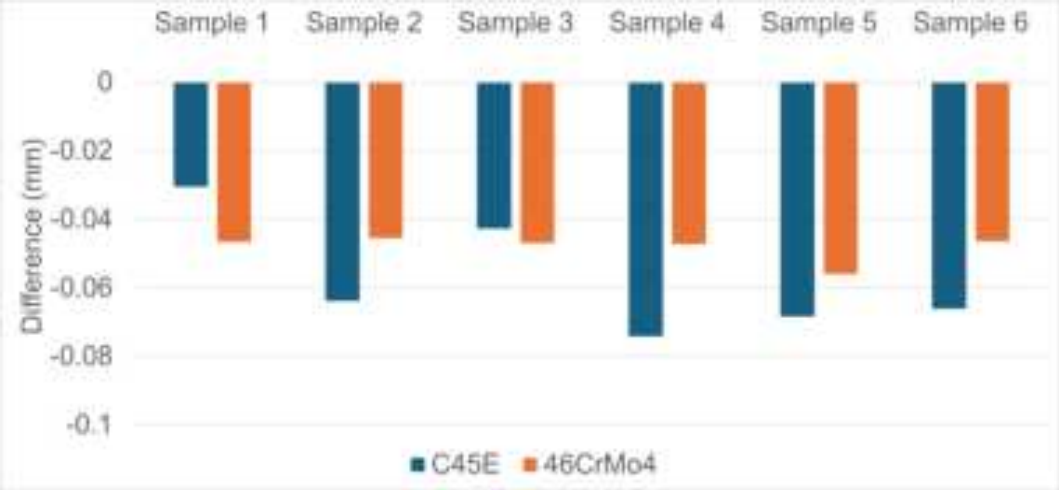

Fig. 4. Deviations from nominal value after LSP application (units: mm)

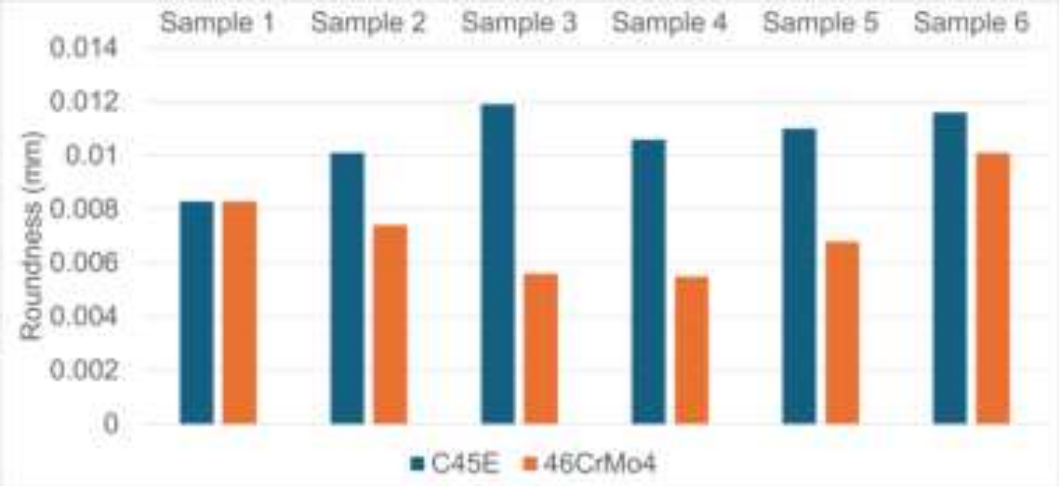

Fig. 5. Roundness of samples after LSP application (units: mm)

From the measured values of residual stress (Table 4), it can be seen that the surface hardening after the application of the LSP method was significant. All the surfaces and layers monitored show elevated values of compressive residual stresses (values with negative sign). Such a hardened surface can be considered as a functional surface able to withstand mechanical stresses, but also deteriorated environmental conditions (such as increased humidity, chemically aggressive environment, etc.). However, the identified residual stress values must be confronted with the mechanical properties of the specific material and, in order to increase the credibility of the above statement, the hardened surface must also be subjected to random checks by means of metallographic tests, since at high values of compressive stresses, the risk of micro-cracks forming due to excessive mechanical loading increases.

Table 4
Mean values of residual stress after LSP application (units: MPa)

Material	C45E			42CrMo4		
Angle	0˚	120˚	240˚	0˚	120˚	240˚
Sample 1	-680.62	-653.42	-670.38	-686.02	-659.27	-676.41
Sample 2	-646.48	-630.38	-635.33	-696.98	-681.26	-640.93
Sample 3	-591.80	-615.32	-602.32	-694.39	-692.3	-682.54
Sample 4	-657.51	-683.38	-667.45	-700.02	-715.98	-708.98
Sample 5	-671.44	-661.58	-645.11	-729.02	-739.27	-711.39
Sample 6	-680.62	-712.84	-685.00	-686.02	-659.27	-676.41

During experiments, the roughness was also measured (Fig. 6 and 7). After machining, before LSP application, better values were identified on surfaces of samples from C45E steels. The values of parameter Ra were very similar for both materials. Parameters Rz and S10z indicate lower differences on material C 45E than 45CrMo6. Also, Surface skewness is more appropriate on samples from C45E steel.

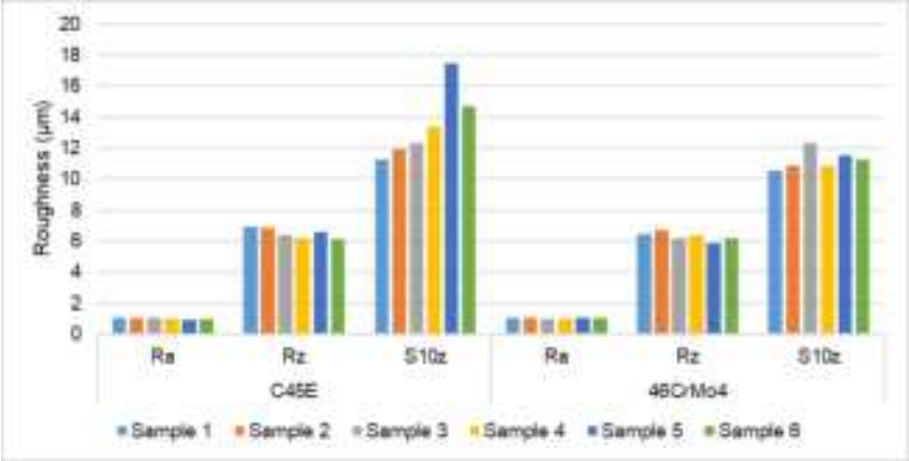

Fig. 6. Surface roughness parameters after machining.

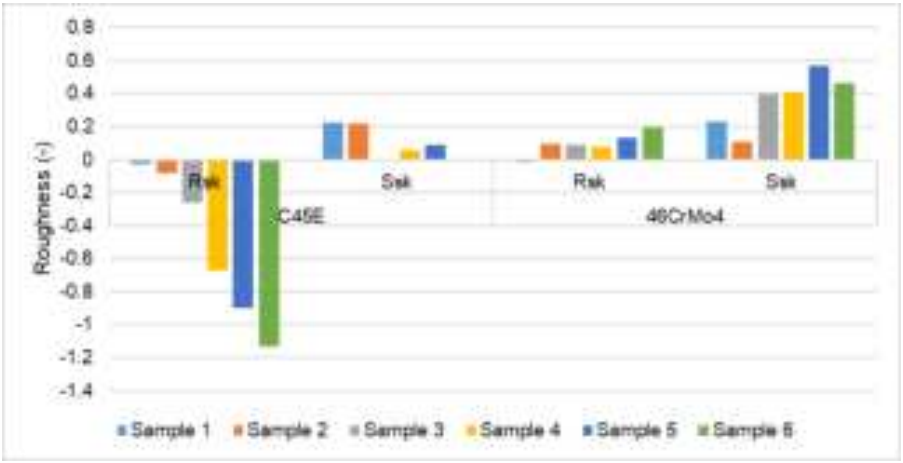

Fig. 7. Surface roughness parameters (skewness) after machining.

The surface roughness values after LSP application (Fig. 8 and 9) became more equal (parameters Ra and Rz). For the surface parameter S10z, the differences are smaller for the 46CrMo6 samples than for C45E, by about 20%.
The surface skewness is better in this case on the samples of 46CrMo6 material because all values are negative. This indicates that the load carrying capacity of such a surface is higher and it can bear loads better.
However, it can be said that all surface roghness values are suitable as functional.

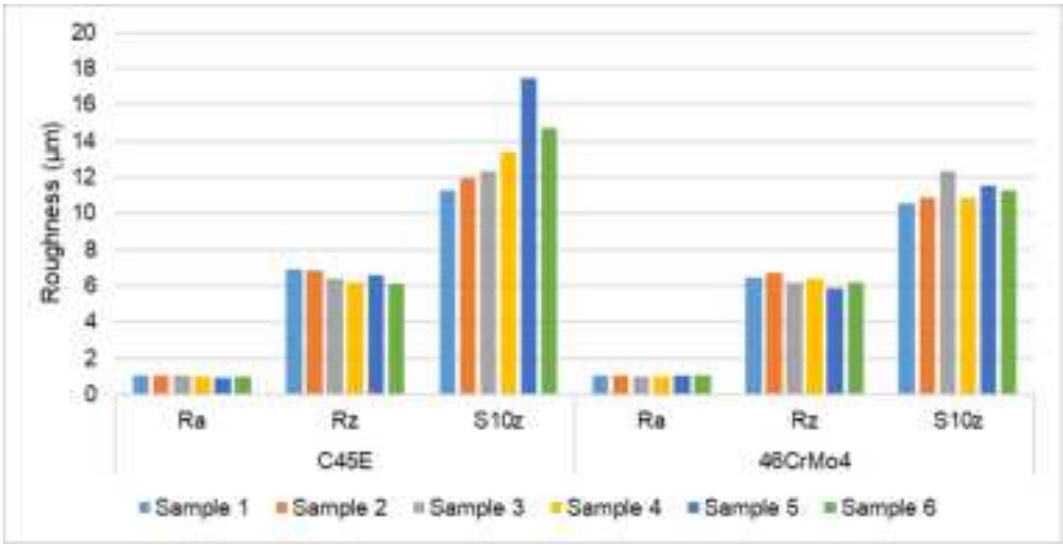

Fig. 8. Surface roughness parameters after LSP application.

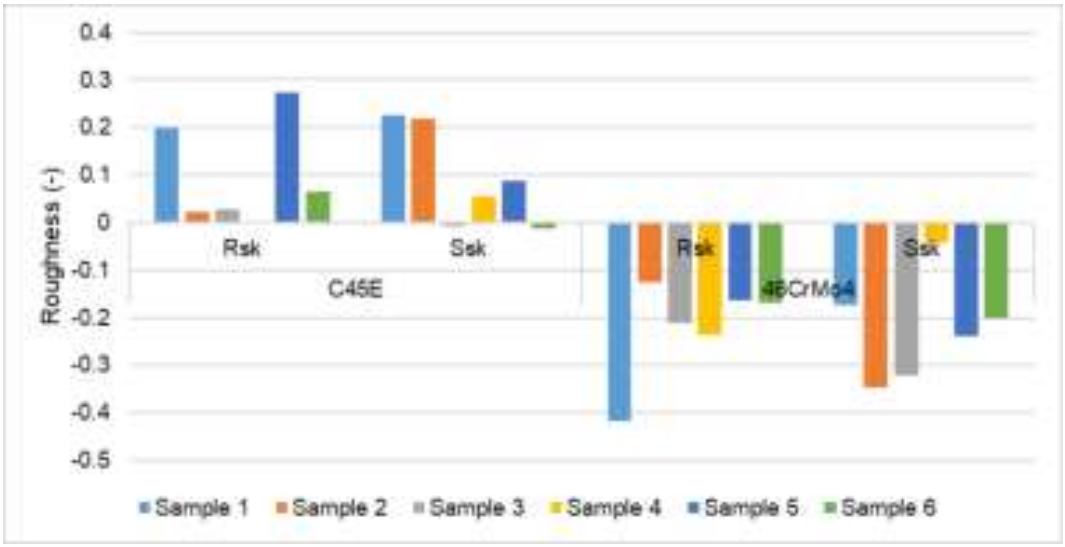

Fig. 9. Surface roughness parameters (skewness) after LSP application.

When measuring the surface roughness, thanks to 3D surface scanning (Fig. 10), the samples were also analysed visually. It can be noticed that black spots, which can be characterized as craters, occur sporadically on the surface thus affected. Their depth is in the order of a few micrometres (maximum values in the range of 10-20 μm). In general, this finding cannot be assessed negatively, but neither positively, and must be confronted with the prescribed tolerances of the resulting surface of the real component. However, if a specific roughness parameter is prescribed, it is necessary to consider the size of these detected craters and at the same time to take adequate steps to correct the hardening conditions by the LSP method.

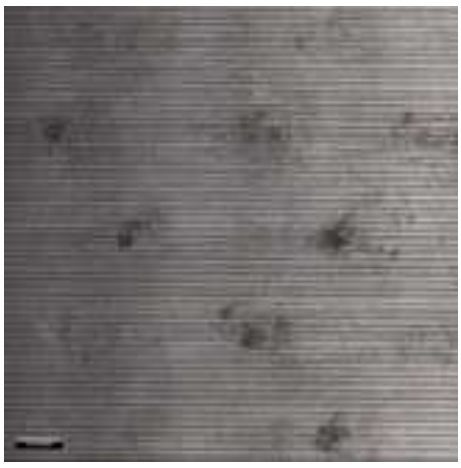

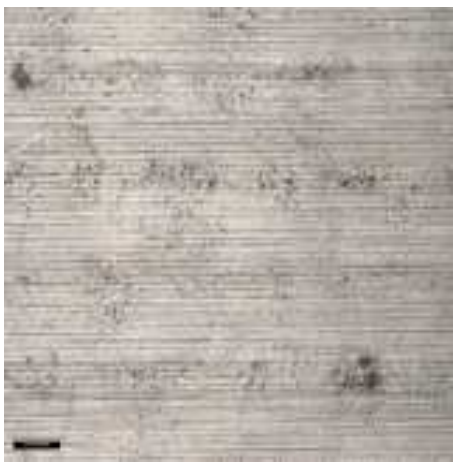

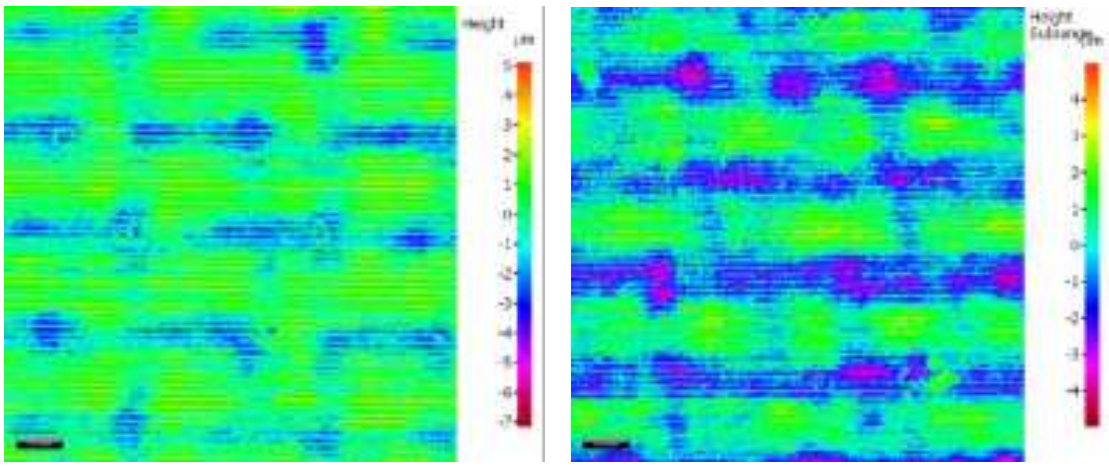

C45E 46CrMo6

Fig. 10. Visual control check of surfaces: real surface and heat map (magnification 20x)

5. CONCLUSION

Based on the acquired results, it can be concluded that the technology has a primarily positive effect on the hardening and functionality of the surfaces, and it is possible to continue to identify other suitable materials, particularly steel-based and other structural materials suitable for the automotive industry.

It is necessary to identify the dependencies on the change of conditions during the application of the technology (they were not identifiable in the presented research) and to apply them to other materials and components not only after the application of machining technologies, but also additive and welding technologies.

The roughness values were analysed. Before the application of LSP, the values were better for the C45E material than for the 46CrMo4 material. Similar facts were found when the dimensions and roundness of the individual samples were analysed. This may be due to the better machinability of the C45E material, as evidenced by the fact that this material has often been used as a machining standard in the past.

On the contrary, the values of residual stresses in the surface layers varied from tensile stresses (max. over 700MPa) to compressive stresses (ca. -200MPa) for the C45E material in sample 6. The hardening of the material is also evidenced by the initial hardness for each sample, when on the 42CrMo4 material the hardness was 40HRC, which is almost double that of C45E.

To clearly determine the cause, a detailed in-depth analysis is needed, which was not the aim of this article. The values for the 42CrMo4 material can be assessed as more appropriate in terms of surface functionality.

Identical indices were analysed after the application of the LSP method. For roughness, deteriorated parameters were observed on both materials, both for Ra, Rz and surface values of S10z. On the other hand, at the same time, due to the effect of hardening, there was a significant decrease in the parameter Rsk and also Ssk, which speak about the load

carrying capacity of the surface. From this point of view, the method can be evaluated positively.

When evaluating the residual stress, it was found that all samples achieved surface hardening. For C45E steel, the values ranged from -600 to -700MPa. More significant material hardening was achieved for the 42CrMo4 samples, where values ranged from approximately -650 to -750MPa, which can be quantified as approximately 10% more compared to C45E.

From the investigations mentioned in the review and from the results presented, it can be concluded that in terms of material hardening, a material that has a higher hardness is preferable, which does not lead to such a significant deterioration of the surface roughness and higher hardenings can be achieved by the application of LSP. From the principles of the LSP method, it is clear that the quality of the cleaned surface from grease and the continuity (thickness) of the applied protective film also have a significant influence on the resulting surface and crater formation. If this layer is breached, craters are more likely to occur. At the same time, the continuity and uniformity of the protective layer can be ensured by appropriate handling (choice of a suitable preparation or increasing the degree of automation and reducing the manual adjustment of the component to the LSP device).

ACKNOWLEDGEMENTS

This article was funded by the University of Žilina project APVV-20-0216 "Research on the implementation of high-impact surface technologies for precision automotive components".

REFERENCES

Al-Ghamdi, K. – Iqbal, A. (2015). A sustainability comparison between conventional and high-speed machining. In Journal of Cleaner Production, 12/2015, Volume 108, Part A, pp. 192-206, ISSN 0959-6526, https://doi.org/10.1016/j.jclepro.2015.05.132

Brajer, J. (2018). Vliv metody laser shock processing na integritu povrchu (Effect of laser shock processing on surface integrity), dissertation thesis, ČVUT Praha,

Cao, Z., Che, Z., Zou, S., Fei, Q. (2011). Numerical simulation of residual stress field induced by laser shock processing with square spot. J. Shanghai Univ. 15, 553– 556, https://doi.org/10.1007/s11741-011-0785-1

CLAUER, A. H. (2019). Laser Shock Peening, the Path to Production, In Metals, 9(6), 626, https://doi.org/10.3390/met9060626

GOLDEN, J., HUTSON, A., SUNDARAM, V., ARPS, J. (2007). Effect of surface treatments on fretting fatigue of Ti-6Al-4V. Int. J. Fatigue 29, 1302–1310, https://doi.org/10.1016/j.ijfatigue.2006.10.005

Hofmann, P., Svoboda, J., Skopeček, T., Řehoř, J. (2003). Tvorba třísky při vysokorychlostním obránění (Chip formation in high-speed machining). In MM Průmyslové spektrum, 2003, č. 4, 96 s., ISSN 1212-2572

Hong, X., Wang, S., Guo, D., Wu, H., Wang, J., Dai, Y., Xia, X., Xie, Y. (1998). Confining medium and absorptive overlay: Their effects on a laser-induced shock wave. Opt. Lasers Eng., 29, 447–455, https://doi.org/10.1016/S0143-8166(98)80012-2

Jawahir IS, Brinksmeier E, M'saoubi R. (2011). Surface integrity in material removal processes: recent advances. Manuf Technol., 60: 603–626, https://doi.org/10.1016/j.cirp.2011.05.002

Kozový P, Matuš M, Bechný V, Holubják J, Joch R, Šajgalík M. (2024). Analysis of Tool Load Concerning the Cross-Sectional Size of Removed Material. Journal of Manufacturing and Materials Processing. 8(3):92. https://doi.org/10.3390/jmmp8030092

Kozový, P., Šajgalík, M., Holubják, J., Slabejová, S., Joch, R., & Drbúl, M. (2023). Influence of the microgeometry of work tool on generation of residual stress in superficial layers of material after trochoidal milling. AIP Conference Proceedings, 2976(1), 060008. https://doi.org/10.1063/5.0172791

Martinez, S. A., Sathish, S., Blodgett, M. P., Shepard, M. J. (2003). Residual stress distribution on surface-treated Ti-6Al-4V by X-ray diffraction. Exp. Mech. 43, 141–147. https://doi.org/10.1007/BF02410495

Montross, C., Wei, T., Ye, L., Clark, G., Mai, Y. (2006). Laser shock processing and its effects on microstructure and properties of metal alloys: A review. Int. J. Fatigue, 24, 1021–1036, https://doi.org/10.1016/S0142-1123(02)00022-1

Petrů J., Zlámal, T., Špalek, F., Čep, R. (2018). Surface Microhardening Studies on Steels After High Feed Milling. In: Adv. Sci. Technol. Res. J., 12(2):222-230, https://doi.org/10.12913/22998624/91888

Peyre, P., Fabbaro, R. (1995) Laser shock processing: A review of the physics and applications. Opt. Quant. Electron., 27, 1213–1229. https://doi.org/10.48550/arXiv.1605.07672

Qiang B, Li Y, Yao C, Wang X. (2018). Effect of shot peening coverage on residual stress field and surface roughness. Surface Engineering., 34(12) pp.:938-945. https://doi.org/10.1080/02670844.2017.1391939

Rostohar, D., Bohm, M., Brajer, J., Kaufman, J., Zulić, S., Mocek. T. (2018) Development of experimental station for laser shock peening at HiLASE, Proc. SPIE 10523, Laser 3D Manufacturing V, 105230K, https://doi.org/10.1117/12.2297092

Ruschau, J., John, R., Thompson, S. R., Nicholas, T. (1999). Fatigue crack nucleation and growth rate behavior of laser shock peened titanium. Int. J. Fatigue, 21, 199–209, https://doi.org/10.1016/S0142-1123(99)00072-9

Sakhvadze, G.Z., Kavtaradze, R.Z., Nikabadze, M.U. (2019). Improvement of the Fatigue Life of Stainless Steel Specimens by Laser Shock Processing. J. Mach. Manuf. Reliab. 48, 353–360, https://doi.org/10.3103/S1052618819040137

Slabejová, S., Šajgalík, M., Kozový, P., Holubják, J., Joch, R., & Drbúl, M. (2023). Simulation of the effect of cutting forces on surface integrity after machining with monolithic ceramic cutters. AIP Conference Proceedings, 2976(1), 060001. https://doi.org/10.1063/5.0172775

Whitenton, E., Heigel J., Ivester, R. (2008). Measurement and characterization of dynamics in machining chip segmentation. 11th CIRP Conference on Modeling of Machining. 2008. https://tsapps.nist.gov/publication/get_pdf.cfm?pub_id=824652 [Accessed: 10 Sept. 2022]
Xu, J., Yan, F., Li, Y., Yang, Z. (2020) Effect of Milling Parameter on the Surface State of Ultra-high strength Steel 16Co14Ni10Cr2Mo 2020 J. Phys.: Conf. Ser. 1676 012041 https://doi.org/10.1088/1742-6596/1676/1/012041
Zhang, H., Ren, X., Tong, Y., Larson, E. A., Adu-Gyamfi, S., Wang, J., Li X. (2019). Surface integrity of 2A70 aluminum alloy processed by laser-induced peening and cavitation bubbles. In Results in Physics, vol. 12, 2019, pp. 1204-1211, https://doi.org/10.1016/j.rinp.2018.11.093

.

LASER WELDING OF ALUMINUM ALLOY AW6005A USING BRIGHTLINE TECHNOLOGY

Ing. Daniel Dřímal, PhD.[1]
Ing. Marián Oselský[2]
Ing. Rudolf Nerád[3]
Ing. Rastislav Ormandy[4]
[1]ORCID: 0000-0003-2311-6228, PRVÁ ZVÁRAČSKÁ, a.s., **SLOVAKIA**
[2]ORCID: 0009-0007-8931-4733, PRVÁ ZVÁRAČSKÁ, a.s., **SLOVAKIA**
[3]ORCID: 0009-0000-5124-5145, PRVÁ ZVÁRAČSKÁ, a.s., **SLOVAKIA**
[4]ORCID: 0000-0002-3581-7921, PRVÁ ZVÁRAČSKÁ, a.s., **SLOVAKIA**

Abstract

The paper describes the laser welding of aluminum alloy AW6005 A and the defects caused by the welding process. The thickness of the experimental material was 2 mm. Three welding modes were chosen for small, medium, and high welding parameters so that the entire thickness of the experimental material was welded. For these welding parameters, the laser beam was divided between the core and the ring in the ratio 100:0, 80:20, 60:40, 40:60, 20:80. Furthermore, the influence of such energy distribution, called BirightLine, on the resulting weld quality was investigated.

Keywords: Laser beam, BrightLine, aluminum alloys

1. INTRODUCTION

The use of aluminum alloys in various industries is an increasingly discussed topic, mainly due to their good strength properties in combination with low specific gravity and good corrosion resistance. These properties provide guaranteed operational reliability of the structure in question with optimized weight, which, in terms of reducing fuel or electricity consumption, has excellent applications, particularly in the automotive industry, which is currently a hotly debated topic from the point of view of the use of alternative energy sources. It is known in the industry that AW 5XXX and AW 6XXX grades are among the most widely used aluminum alloys. Both alloys have good weldability, but suffer from a relatively high susceptibility to welding defects, especially of a structural nature such as porosity, cracks, or fissures. These defects adversely affect the mechanical properties and it is therefore essential to prevent their formation. This can be approached, in particular, by an appropriate choice of the technological parameters of the welding method used. Of the fusion methods, MIG and TIG methods have good results in terms of porosity, mainly because of the good possibility of protecting the welding process. Their main disadvantages compared to methods using concentrated energy sources include, for example, a higher HAZ and the need to use higher welding currents due to the high thermal conductivity of aluminum, which can result in

weld deformation. From a production point of view, it is essential to mention that when welding weldments of more complex shapes, the problem of torch availability arises in the case of an automated welding workstation, whose welding movements are provided by an industrial robot. Therefore, in the case of using Mig, and TIG welding methods in robotic welding workplaces, it may be necessary to weld places with poorer accessibility manually, which has an adverse effect in terms of production. Also, the disadvantages of filler metal usage should be mentioned. The use of additional material in a fully automated welding workplace for welding more complex shapes can be very problematic and in a lot of cases impossible regarding the availability of the welding torch to the site. (Hrivňák, 2009)
Precisely because of these shortcomings, methods using concentrated energy sources, of which electron beam and laser beam welding are the most commonly applied, appear to be more efficient methods in such welding cases. In both cases, it is possible to achieve deep through-holes while maintaining a relatively narrow HAZ. However, the use of a laser beam is problematic, especially when it is required to weld more complex shaped surfaces, due to the protection of the welding process from the surrounding atmosphere, because the weldment often cannot be placed in a gasprotection chamber due to the dimensions and also the economic requirements for the construction of such a workstation. Reduction of internal defects in the weld metal is possible by influencing the shape and dimensions of the steam gas channel (keyhole) in the case of concentrated beam sources. (Wagner, et al., 2022) The main significance lies primarily in laser welding with low process shielding, where defects, particularly pores, can only be prevented by creating a stable and sufficiently wide keyhole. The size and shape of the keyhole can be influenced by focusing the laser beam; however, this adversely affects penetration depth. Another option is to optimize the keyhole shape without the need to focus the beam, using the BrightLine (BL) technology, which distributes the energy concentration of the laser beam on the surface of the welded material. (Punzel, et al., 2020)

2. METHODOLOGY OF THE EXPERIMENT

The main goal of the experiment is primarily to eliminate or reduce the number of defects in the weld metal and on its surface by intentionally influencing the shape and geometry of the keyhole, thereby achieving high-quality weld joints. When using the BL module, the objective is to deliberately alter the energy distribution of the laser beam as it hits the base material surface. The beam's power is split between its central (core) and outer (ring) sections, as shown in Figure 1. Therefore, an optimal power distribution ratio must be achieved between the core, which ensures penetration, and the ring, which provides keyhole stability. The investigated power distribution ratios between the core and ring are: 100:0, 80:20, 60:40, 40:60, and 20:80. The ratio of 100% power directed into the ring was not evaluated on the samples, as this configuration did not result in sufficient material melting for analysis.
For each of the mentioned ratios, different welding powers and speeds were initially proposed, maintaining a constant focal distance. After conducting these trials and performing visual surface and root analyses of the welds, a macroscopic analysis was conducted. Based

on the results of these analyses, a discussion followed on which energy distribution ratios using BL in combination with welding parameters are most favorable for the resulting weld quality.

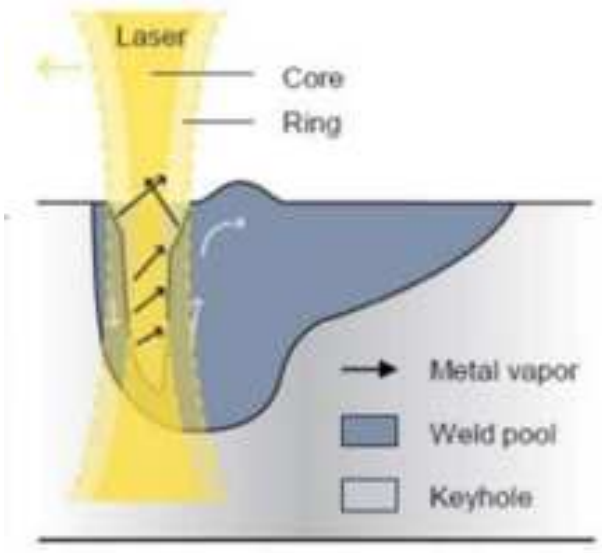

Fig. 1 The principle of energy division in the vapor-gas channel (keyhole) (TRUMPF)

2.1. DESCRIPTION OF THE WORKPLACE

The experiments were conducted at the robotic laser workstation PZ UNILAS 1 (Fig. 2). The laser source used was the solid-state disk generator TRUMPF TruDisk 5001, with a laser radiation wavelength of 1.03 μm and a maximum power of 5 kW. The laser generator has a dual-core transport optical fiber with core diameters of 100 and 400 μm. The laser beam is processed by the BEO D70 processing head with a focal length of 200 mm. The processing head is equipped with a Multispot module, which uses a pair of optical prisms rotated 90° relative to each other and divides the laser beam into four individual beams. However, in this case, the beams were directed into a single bundle to eliminate energy distribution across the impact surface in this manner, as this is the objective of the next phase of the project. The positioning of the processing head is performed by a 6-axis industrial robot OTC Daihen FD A20, designed for laser applications with enhanced accuracy. The control system also integrates a rotary tilting positioner. All eight axes are fully synchronized.

Fig. 2 Robotic laser workstation PZ UNILAS 1

2.2. DESCRIPTION OF THE BASE METAL

The experimental material was selected based on market demands, particularly for the automotive industry, where emphasis is placed on the chosen aluminum alloy's good strength properties and favorable technological properties, particularly weldability. The material available was for extruded aluminum profiles, specifically alloy AW 6005A, which belongs to the AW 6XXX series.

This is a ternary alloy with a density of 2700 kg/m³ and a melting temperature ranging from 585 to 650 °C. It falls under the category of wrought heat-treatable aluminum alloys. These alloys contain relatively small amounts of alloying elements, Si and Mg (up to 1%). Strengthening is achieved through the precipitation of the Mg_2Si phase. In areas where this phase does not precipitate, a decrease in strength occurs. AW 6005A is prone to hot cracking of the weld metal, especially when no filler material is used. The weldability of this alloy is further complicated by the degradation of the mechanical properties of the weld metal. After welding, achieving mechanical properties of the weld metal comparable to the base material is challenging, even after artificial or natural aging processes. The thermal cycle of welding also leads to a reduction in mechanical properties in the heat-affected zone (HAZ). (Mathers, 2002)

Despite these challenges, its weldability is considered high-level and can be heattreated to improve its mechanical properties. The mechanical properties (for thickness $t < 5$ mm) and chemical composition of AW 6005A are presented in Table 1 and Table (ALUMERO, 2020)

Tab. 1 Chemical composition of AW-6005A [wt.%]

Element	Si	Fe	Cu	Mn	Mg	Cr	Zn	Ti	Al
Min	0,5	-	-	-	0,4	-	-	-	Rest
Max	0,9	0,35	0,3	0,5	0,7	0,3	0,2	0,1	

Tab. 2 Mechanical properties of AW-6005A (t<5mm)

$Rp_{0,2}$[MPa]	Rm[MPa]	A[%]	HB	E[MPa]
225	270	8	90	70

Source: (ALUMERO, 2020)

2.3. PROPOSAL OF PRELIMINARY WELDING PARAMETERS FOR THE SELECTED ALLOY TYPE, THICKNESS, AND WELD TYPE

For the optimization of welding parameters, an aluminum alloy AW6005A with a thickness of 2 mm was selected. Test welds were performed using a laser beam on an automated robotic workplace, with a welding angle of 90˚. Full-penetration welds were made on extruded profiles (in areas with a thickness of 2 mm). The welding methodology involved determining the parameters for concentrating 100% of the laser beam energy into the core for three welding modes, where the focal position in all three modes was on the surface of the base material. The goal was to identify the correct parameters for the lowest, medium, and highest speeds. The power was adjusted to the respective speeds to achieve full penetration. This wide range of test experiments allowed for a more precise determination of the impact of laser beam technology (BL) at various speeds and power levels. The resulting welding parameters are shown in Table 3.

After selecting the welding parameters, full-penetration welds were performed on cut rectangular samples with a thickness of 2 mm. Each sample featured three fullpenetration welds (see Fig. 3) with a length of 100 mm, corresponding to the parameters for the lowest, medium, and highest speeds. For each such sample, a different energy distribution ratio between the core and ring was set to: 100:0, 80:20, 60:40, 40:60, and 20:80.

Fig.3 Example of a test sample with penetration weld markings No. 5, 4, 6

Tab. 3 Resulting welding parameters for BL technology

P [W]	v_z [mm/s]	Sample designation	The power ratio core:ring	h_z [mm]	h_k [mm]	h_p [mm]	Input heat Q [J/mm]
1500	38,33	3	100:0	2,74	2,25	2,42	39,13
		6	80:20	2,66	1,26	2,26	
		9	60:40	2,15	-	1,34	
		12	40:60	1,01	-	0,62	
		15	20:80	0,37	-	0,27	
2500	83,33	2	100:0	2,12	1,09	2,56	30
		5	80:20	2,23	1,76	2,5	
		8	60:40	2,05	1,21	2,32	
		11	40:60	1,88	-	1,57	
		14	20:80	1,23	-	0,77	
5000	233,33	1	100:0	1,54	1,01	2,34	21,43
		4	80:20	1,26	1,05	2,17	
		7	60:40	1,56	0,93	2,05	
		10	40:60	1,55	0,93	2,11	
		13	20:80	1,69	0,9*	2,5	

* penetration was interrupted, h_z - weld surface width, h_p – penetration depth, - marking the lack of fusion, hk – weld root width, P – power, v_z – welding speed.

2.4. VISUAL INSPECTION

The prepared samples were cleaned and illuminated for inspection. For better evaluation, individual samples were photographed under the microscope. The weld and root surfaces were assessed, specifically their morphology, spatter, weld surface width, root width, and any other observable surface and root defects.

2.5. MACROSCOPIC INSPECTION

For macroscopic inspection, three cross-sections were prepared, spaced 15 mm apart along the full length of the 100 mm penetration. These cross-sections were prepared using standard metallographic procedures, which involved embedding the sample and, after curing, grinding and polishing it. Once prepared, the samples were photographed under a microscope for analysis. For these macroscopic sections, defects in the weld metal, weld and root width, weld reinforcement, root overflow, and penetration depth were examined.

3. EXPERIMENT

The experiment was divided into two parts. In the first part, the samples were visually evaluated in terms of surface and root quality. The second part describes the macroscopic analysis of cross-sections of the individual welds.

3.1. VISUAL ANALYSIS

The surface of the weld bead was irregular in all welding modes for the BL 100% core settings (samples No. 1, 2, 3). On the welds, spatter, solidification waves formed during cooling, and slight burn-throughs were observed (Fig. 4a). Samples No. 4, 5, and 6 were similar to the first ones but with slightly reduced spatter. For the fullpenetration welds with a BL ratio of 60% core, the amount of spatter significantly decreased, but the surface remained irregular. The surface irregularity was the smallest for a BL ratio of 20% core (Fig. 4b).

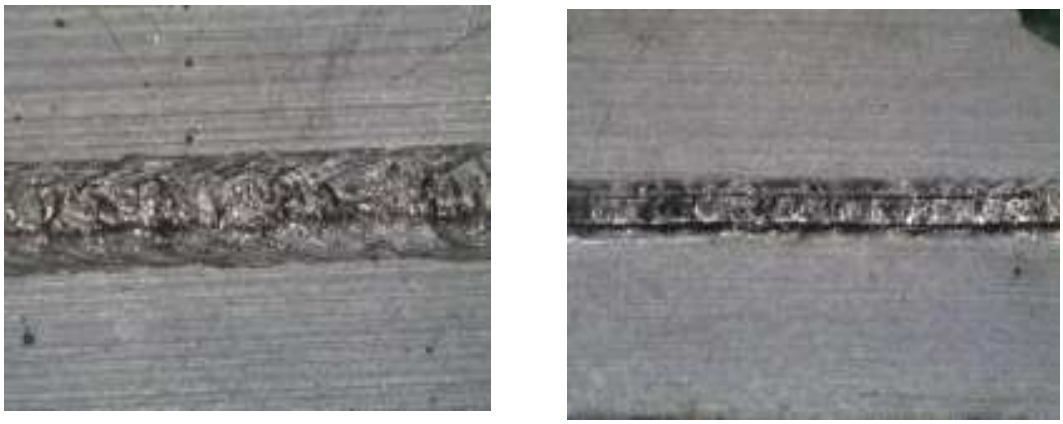

a b

Fig. 4 Weld beads with different BL core: mantle ratios: a - Full penetration No. 2
b - Full penetration No. 14 (see Table 3)

The set of samples welded with a welding speed of v_z = 233.33 mm/s and power P = 5000 W, with BL ratios of 40% and 80% to the core (samples No. 10 (Fig. 5a) and No. 4), exhibited the greatest spatter in the root area of the weld. The least spatter was observed in the samples with BL ratios of 100% and 20% to the core (samples No. 1 and No. 13), although sample No. 13 did not have a continuous weld root.

For the samples welded with v_z = 83.33 mm/s and P = 2500 W, the weld roots were evaluated only for samples No. 2 (Fig. 5b), No. 5, and No. 8, due to lack of fusion in the other samples. The spatter in these root layers was smallest again for the sample with BL 100% to the core (sample No. 2). The full-penetration welds with BL ratios of 80% and 60% to the core (samples No. 5 and No. 8) had roots with fewer defects.

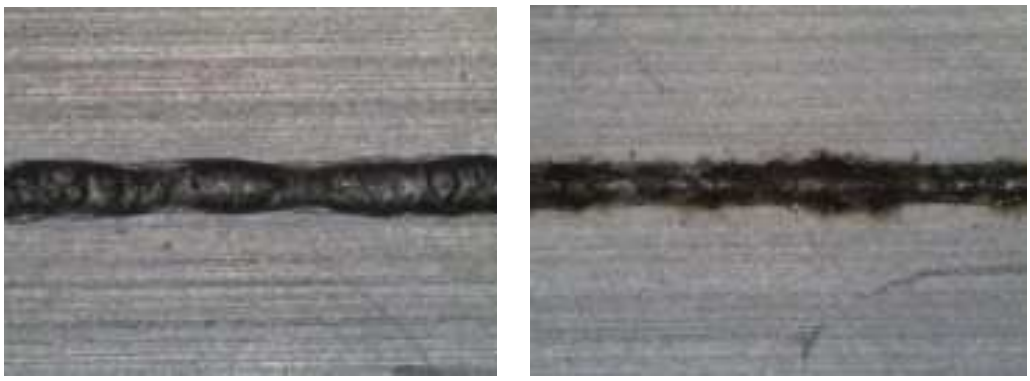

a b

Fig. 5 Samples of the weld root surfaces: a – Sample No. 2, b – Sample No. 10

The samples welded with parameters v_z = 38.33 mm/s and P = 1500 W, which had full penetration, were samples No. 3 and No. 6. The spatter in these samples was minimal.
The largest difference in weld widths was observed for the samples welded with v_z = 38.33 mm/s and P = 1500 W. For these parameters, the sample with a BL ratio of 100% to the core (sample No. 3 (Fig. 6a)) had the widest weld, with a width of h_z = 2.74 mm. In contrast, the sample with a BL ratio of 20% to the core (sample No. 15 (Fig. 6b)) had the narrowest weld, with a width of h_z = 0.37 mm.
The full-penetration welds welded with v_z = 83.33 mm/s and P = 2500 W showed a similar trend, except that the widest weld, with h_z = 2.23 mm, was observed on the sample with a BL ratio of 80% to the core (sample No. 5). The weld widths, when energy was distributed into the ring, decreased at a lower rate compared to the samples welded with v_z = 38.33 mm/s and P = 1500 W (see Fig. 8).
Full-penetration welds welded with v_z = 233.33 mm/s and P = 5000 W had a completely different trend. The widest weld, with h_z = 1.69 mm, was observed on the sample with a BL ratio of 20% to the core (sample No. 13), while the narrowest weld, with h_z = 1.26 mm, was observed on the sample with a BL ratio of 80% to the core (sample No. 4). The individual values for the other samples are listed in Table3. The dependence of weld width on the energy distribution ratio can be seen in Fig. 8.

a b

Fig. 6 Weld beads for parameters with v_z = 38.33 mm/s and P = 1500 W, with BL core:ring ratio: a – 100:0, b – 20:80

The root widths of the welds followed a similar trend to the weld surface widths. For the parameters v_z = 38.33 mm/s and P = 1500 W, the root was widest with a BL ratio of 100% to the core (sample No. 3). However, due to the energy distribution into the ring, the width decreased more rapidly compared to other speeds. For the welds made with v_z = 83.33 mm/s and P = 2500 W, the root exhibited a similar trend. In the case of parameters v_z = 233.33 mm/s and P = 5000 W, the root width remained relatively consistent across all energy distribution ratios, except for the last one, where the speed was too high, and the root was interrupted. All root layer widths are listed in Table 3.

3.2. MACROSCOPIC ANALYSIS

From the macroscopic images, it was possible to determine that for the full penetrations with v_z = 38.33 mm/s, P = 1500 W, defects such as porosity, weld sink, and root overflow were present. All three defects were observable in the sample with a BL ratio of 100% to the core (sample No. 3 (Fig. 7a)). The sample with a BL ratio of 80% to the core (sample No. 6) contained porosity, and the weld surface sink and root overflow were not as significant as in the first case. For the remaining samples with these parameters, no porosity or weld sink was found, but in these cases, a lack of penetration was observed.

For the welding parameters v_z = 83.33 mm/s, P = 2500 W, the same defects were observed but in different locations. Porosity was found in the weld metal for the full penetration with a BL ratio of 40% to the core (sample No. 11). Even surface cracks were found here. Weld sink and root overflow were present in the weld for the sample with a BL ratio of 80% to the core (sample No. 5). Root inflammation and root overflow were observed in the sample with a BL ratio of 100% to the core (sample No. 2). The best weld metal quality was found in the sample with a BL ratio of 60% to the core (sample No. 8), and also in sample No. 14, although this sample did not achieve full penetration.

For the set of samples with v_z = 233.33 mm/s, P = 5000 W, porosity was not observed. However, hot cracks were formed, and these occurred most frequently in the sample with a BL ratio of 60% to the core (sample No. 7 (Fig. 7b)). This sample also contained inflammation in the root. The remaining samples appeared to be fine, although some had root overflow (sample No. 1) or surface inflammation (sample No. 13). The best results were achieved with samples No. 4 and No. 10, which did not contain any defects in the weld metal.

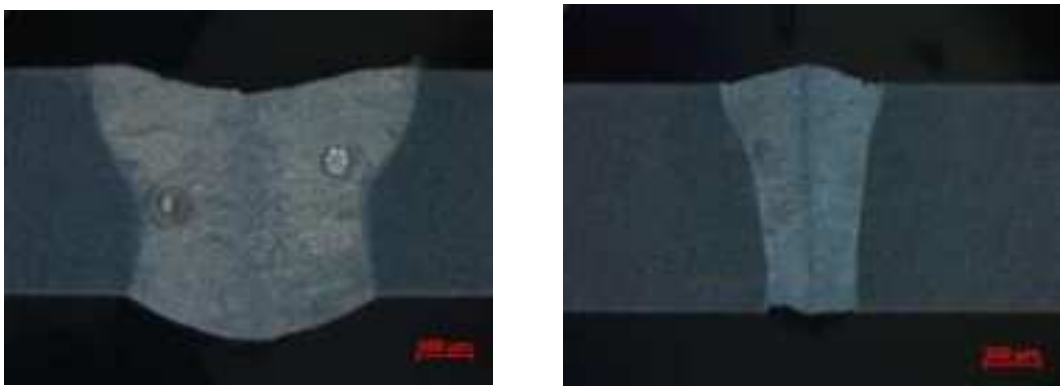

a b

Fig. 7 Macroscopic samples: a – sample No.3, b – sample No.7

Another important parameter examined in the macroanalysis was the depth of penetration. For the samples welded with the parameters v_z = 38.33 mm/s, P = 1500 W, this parameter started at higher values, which decreased starting from a BL ratio of 60% to the core and reached its minimum at a BL ratio of 20% to the core (sample No. 15).
For the samples welded with v_z = 83.33 mm/s, P = 2500 W, the trend was similar, with the deepest penetration occurring at a BL ratio of 100% to the core (sample No. 2). The main difference was that the depth changed more significantly at a BL ratio of 40% to the core (sample No. 11).
For the full penetrations welded with v_z = 233.33 mm/s, P = 5000 W, the penetration depths were relatively consistent across all BL ratios. The deviations from the average depths did not exceed 0.17 mm. All the penetration depths for each ratio and parameter are shown in Table 3. The dependence of penetration depth on the core: ring energy distribution ratio is presented in Fig. 8.

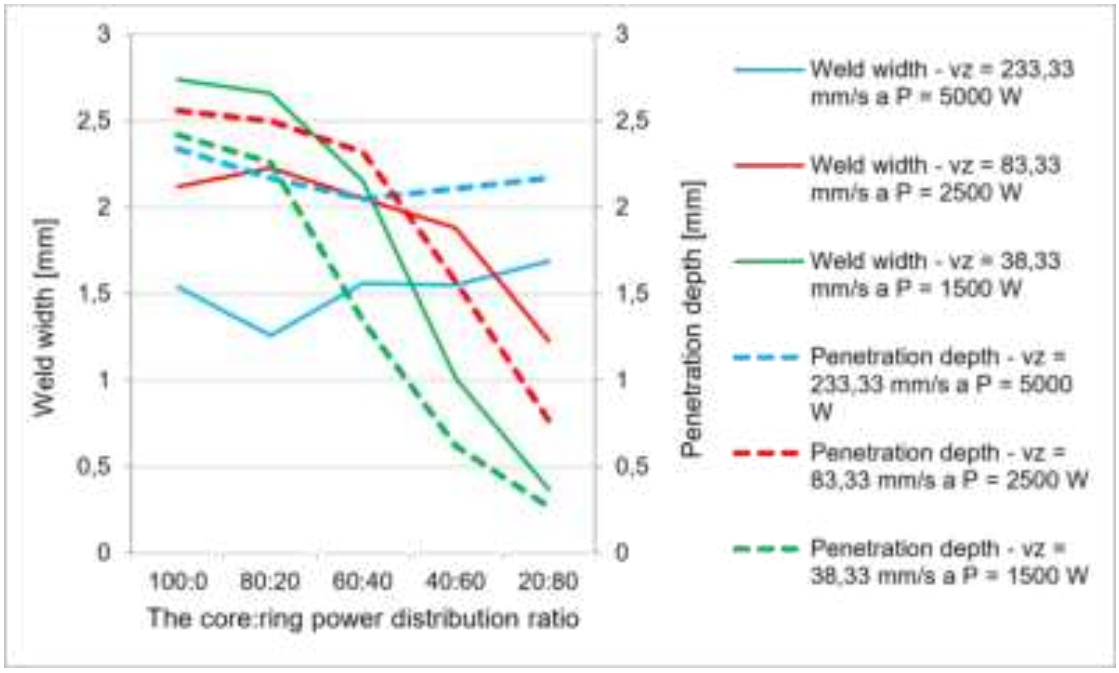

Fig. 8 The dependencies of penetration depth and weld surface width on the core:ring energy distribution ratio

6. DISCUSSION

The aluminum alloy AW 6005A welded by laser beam exhibits defects in the form of porosity, cracks, and weld geometry issues (undercut, root leakage, and burnthrough). These issues were mainly observed in samples with 100% energy distribution to the core, in combination with different welding powers and speeds. The surfaces and roots of the welds in this case also had reduced quality, primarily due to defects such as spatter, burn-through, and root leaks. All these defects likely resulted from insufficient keyhole stability, combined with inappropriate welding power and speed settings. Based on these results, it made sense to further investigate and optimize the energy distribution ratio using the BL (beam laser) technique, as it had a proven effect on weld quality.

Samples welded with parameters of travel speed v_z =38.33mm/s and power P=1500 W the penetration is lost already at the energy distribution ratio of 60% to the core. Penetration was not achieved due to insufficient energy input into the core, which meant the laser beam could not create a sufficiently deep keyhole when interacting with the surface. The weld width rapidly decreased as the energy was split into the ring, starting from the 80% energy distribution to the core, and the weld surface quality improved with a larger energy distribution to the ring. This energy was likely focused more on stabilizing the keyhole (as it was distributed more on the material surface) rather than on the penetration of the weld, and the provided power was thus insufficient to achieve penetration. For these factors, the best

weld among all the present factors was found with the energy distribution ratio of 80% to the core and 20% to the ring. This weld had the least defects and the best weld geometry among these parameters.

For the set of samples welded with v_z = 83.33 mm/s, P = 2500 W, the root pass was lost at an energy distribution ratio of 40% to the core. This could have been caused by low power related to the energy distribution to the ring, similar to the previous parameters. The weld widths showed a similar trend as v_z = 38.33 mm/s, P = 1500 W, but the decrease in width was not as rapid (due to the higher power). The surface quality of the welds was similar to the previously mentioned samples. Macroanalysis of the samples with v_z = 83.33 mm/s, P = 2500 W showed good quality for certain BL distributions. Of course, for the energy ratio of 100% to the core, the keyhole probably did not stabilize, and defects in geometry and porosity in the weld metal were present. At the energy ratio of 60% to the core, the number of defects was significantly reduced, and high weld quality was achieved. Interestingly, at an energy ratio of 40% to the core and 60% to the ring, although no root pass was achieved, defects such as porosity and cracks were observed, which did not occur for lower and higher welding parameters. These errors likely occurred because a sufficient amount of material was melted to create pores, which could not evaporate due to the lack of fusion. Alternatively, insufficient mixing of the weld metal using the BL technology in connection with the lack of fusion could have contributed. The best weld quality was found for the BL ratio of 60% to the core and 40% to the ring. This sample showed reduced porosity and no significant defects in the weld geometry.

The welding regime with parameters v_z = 233.33 mm/s and P = 5000 W showed penetrations at all energy distribution ratios. The weld widths exhibited an increasing trend because a sufficient amount of energy was entering the material, which allowed for a larger amount of material to be melted with a higher energy distribution into the ring. However, a rapid increase in the weld width did not occur due to the high welding speed. Surface quality improvement followed a similar trend as with previous parameters when using BL. Photographs of the macroscopic cross-sections showed varying weld qualities. The best results were found for the energy distribution ratios of BL 80% and 40% into the core. For 80%, there was a high occurrence of spatter on the weld surface, likely due to the weak stability of the keyhole. The best result was observed for the sample with an energy distribution ratio of core: ring 40:60. This ratio had the most favorable effect on the investigated factors, such as spatter, weld geometry, and the occurrence of cracks.

7. CONCLUSION

For the selected aluminum alloy AW6005A with a thickness of 2 mm, welded joints were made using laser welding with the BL technology. An important parameter in the BL technology is the higher welding power, which allows this technology to have a more significant impact on the formation of the weld metal. Additionally, by distributing energy in a certain ratio to the ring, the keyhole was probably stabilized to such an extent that the weld

metal contained fewer defects. The ideal energy distribution varied depending on the parameters studied.

For the parameters: v_z = 233.33 mm/s, P = 5000 W, the best sample had a BL ratio of 40:60. The only drawback was the smaller spatter in its root layer. For the parameters: v_z = 83.33 mm/s, P = 2500 W, the best sample had a BL ratio of 60:40. The disadvantage of this sample was also a smaller spatter in the root layer and a lower presence of pores. For the parameters: v_z = 38.33 mm/s, P = 1500 W, the best sample was with a BL ratio of 80:20. This sample exhibited more defects compared to the previous ones, and therefore, the resulting weld quality was considered the lowest.

ACKNOWLEDGMENTS

This work was supported by the Agency for Research and Development Support (APVV) under contract No. APVV-22-0353.

REFERENCES

ALUMERO. 2020. EN AW-6005A. [Online] Júl 2020. https://www.alumerogroup.eu/fileadmin/user_upload/downloads/folder/technologien/ALUMERO_Legierungen_EN-AW-6005A_EN.pdf.

Hagenlocher, Ch and M., Seibold. 2018. Modulation of the local grain structure in laser beam welds to inhibit the propagation of centerline hot cracks. Procedia CIRP 74. 2018, pp. 434-437.

Hrivňák, Ivan. 2009. Zváranie a zvariteľnosť materiálov. Bratislava : Citadella, 2009. p. 490. ISBN 978-80-89628-18-6.

Jabar, S., et al. 2023. Effects of the adjustable ring-mode laser on intermetallic formation and mechanical properties of steel to aluminium laser welded lap joints. Materials & Design 227. Február 18, 2023.

Mathers, Gene. 2002. The welding of aluminium and its alloys. Cambridge : Woodhead Publishing, 2002. p. 236. 0-8493-1551-4.

Punzel, E., et al. 2020. Influence of power distribution on weld seam quality and geometry in laser beam welding of aluminum alloys. Procedia CIRP 94. September 2020, pp. 601-604.

TRUMPF. High-performance solid-state laser. [Online] TRUMPF LASER TruDisk. https://www.apricon.fi/en/product/trudisk/.

Wagner, J and kol. 2022. Influence of dynamic beam shaping on the geometry of the keyhole during laser beam welding. Procedia CIRP 111. September 2022, pp. 448452.

POSSIBILITIES OF INCREASING THE RANGE OF ARTILLERY AMMUNITION CALIBER 15MM – M107

Ing. Ľudmila Timárová[1],
Doc. Ing. Michal Krbaťa, PhD.[2],
Ing. Lucia Kakošová[3],
Ing. Jozef Jaroslav Fekiač[4]

[1]0000-0003-2192-3253: Faculty of Special Technology, Alexander Dubček University of Trenčín. Ku kyselke 469, 911 06 Trenčín. **Slovak Republic.**

[2]0000-0002-0520-8180: Faculty of Special Technology, Alexander Dubček University of Trenčín. Ku kyselke 469, 911 06 Trenčín. **Slovak Republic.**

[3]0009-0002-3041-4290: Faculty of Special Technology, Alexander Dubček University of Trenčín. Ku kyselke 469, 911 06 Trenčín. **Slovak Republic.**

[4]0001-6392-8389: Faculty of Special Technology, Alexander Dubček University of Trenčín. Ku kyselke 469, 911 06 Trenčín. **Slovak Republic.**

Abstract: The aim of this article is to investigate the possibilities of increasing the range of artillery ammunition of calibre 155 M107 through optimization of its technical characteristics. In the initial part, we analyse the current state of this ammunition, focusing on its external shape and guide rim, which are key to improving aerodynamic properties and thus range. The next part of the paper details the design of the bottom sprue, which has a significant impact on the ballistics of the projectile. Next, we explore the potential use of rocket motor and intake cavities that can significantly increase the range of artillery ammunition. We conclude the paper by presenting a conceptual design of a new type of projectile that takes into account all previous findings and calculations. The final evaluation summarizes the results and presents the potential of an optimized projectile that achieves higher efficiency and longer range due to improved technical properties.

Keywords: Ballistics. M107. Munition. Artillery. Projectile.

1. ANALYSIS OF THE CURRENT SITUATION

The 155 mm calibre artillery ammunition, designated M107, is a fragmentation round. The utility of this ammunition is for partial or total destruction of enemy forces. The effect of this projectile is accomplished by the kinetic energy of the shrapnel from the projectile parts

and the pressure wave generated by the explosive charge. The maximum range of this missile exceeds 18 000 m [1].

A powder charge is used to give the initial velocity of the projectile, which is selected according to the needs of the particular application. Guns are usually designed to meet specified standards and to withstand a certain amount of barrel and chamber pressure. Based on knowledge of the ingredients used to make propellants, a propellant charge is developed that meets the needs of the weapon and will not cause damage to the weapon. When the propellant charge is ignited, a large quantity of hot gases is released. Deflagration takes place within milliseconds, with the pressure in the weapon acting on the bottom of the projectile and sweeping - accelerating it towards the muzzle of the barrel [11].

The 155mm caliber M107 ammunition is fireable with standard M4A2, M3A1 or M119A1 and M119A2 cartridges.

1.1 The outer Shape of the projectile

In order to achieve the lowest possible air resistance, the missile should have an optimal aerodynamic shape. This shape is achieved by sculpting the missiles into a high slenderness shape, where it usually consists of three main parts [13]:

- Front ogival part.
- The cylindrical part.
- Posterior ogival part.

In the case of projectiles with a driving band, the shape is further modified, including [13]:

- The driving band.
- Centering rings on the front and rear sides.
- Modification of the projectile base shape.

1.2 Driving band

Driving bands are designed to catch the projectile in the transition cone and then, as it moves through the barrel, to provide sealing and impart the required rotation to the projectile. The design requirements for a driving band are extensive [12]:

- Strength to ensure rotational movement,
- Minimum groove depth to prevent contact with the projectile body, thereby reducing stress,
- Construction matching the chamber shape,
- Creation of a sealed space,
- Positioning on the projectile that aligns with the desired range and shooting accuracy,
- Proper guidance of the projectile in the barrel,
- Smallest possible dimensions while meeting the required specifications for a driving band,
- and others.

Projectiles with a driving band cut into the barrel grooves using the driving band, allowing the projectile body itself to move freely. The maximum permissible diameter of these projectiles is naturally smaller than the caliber of the given weapon ($d_s < d$) [3].

The band is located in a groove on the projectile body, where it is either pressed, crimped, or welded in place. For the first two options, the base must be roughened to prevent the driving band from rotating. Welding the band onto the projectile provides a stronger bond [2].

The overlap between the barrel grooves and the maximum diameter of the band is necessary so that the material of the band fills the profile at points where it engages with the barrel grooves. This ensures improved sealing of propellant gases [3].

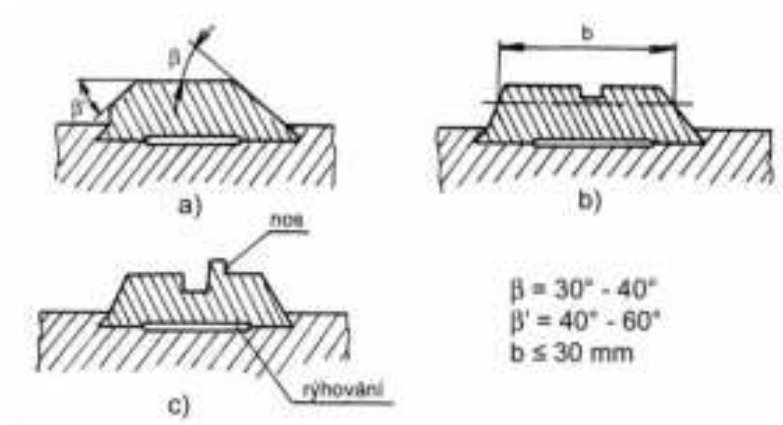

Figure 1: Shapes of driving bands

The front slope (angle β) changes according to the shape of the transition cone and helps reduce its load when inserting the driving band into the grooves. *The rear slope* (angle β') is often used in larger calibers with wide driving bands. After inserting the driving band and during the movement of the projectile, the material of the band is pushed backward, which can create asymmetrical tabs that negatively affect the ballistic properties of the projectile [7].

The optimal material for manufacturing driving bands is pure electrolytic copper. In the production of projectiles intended for powerful weapons, up to 5% nickel is added to the copper to increase its strength. Ferrous sulfide (FeS), a compound of sulfur and iron, known as soft sintered iron, can also be used as a substitute for this material. These bands are impregnated with paraffin to improve their sliding properties. Currently, various plastic materials are also used for the production of driving bands [7].

2. OPTIONS FOR INCREASING THE RANGE OF ARTILLERY AMMUNITION

To increase the range of an artillery projectile without modifying the weapon itself, the most effective method is to add an additional propulsion module to the existing projectile. This module provides additional thrust at the optimal point of the trajectory, allowing the projectile to achieve the maximum range for a given combination of weapon and ammunition [10].

Practical analysis indicates that there are three main ways to increase the range of a projectile [9]:

- Increasing the initial velocity of the projectile,
- Improving the shape coefficient of the projectile,
- Providing additional acceleration to the projectile along its trajectory.

The maximum range of a projectile depends on its initial velocity, the angle at which it is fired, as well as its caliber, weight, and aerodynamic properties related to air resistance [10].

For artillery weapons, structurally effective solutions only include reducing the shape coefficient of the projectile or providing additional acceleration along its trajectory. However, this introduces a series of problems and typically worsens the projectile's parameters [9].

In an effort to achieve an optimal shape coefficient for the projectile, the following design principles have been applied [9]:

- Utilization of a design with a suction cavity,
- Creation of various types of sub-caliber projectiles,
- Lengthening of the front ogive,
- Reduction of the base drag of the projectile.

2.1 Base Exhaust

There are two principles for solving the generator base exhaust [2]:

- Thermal.
- Rocket engine with zero thrust.

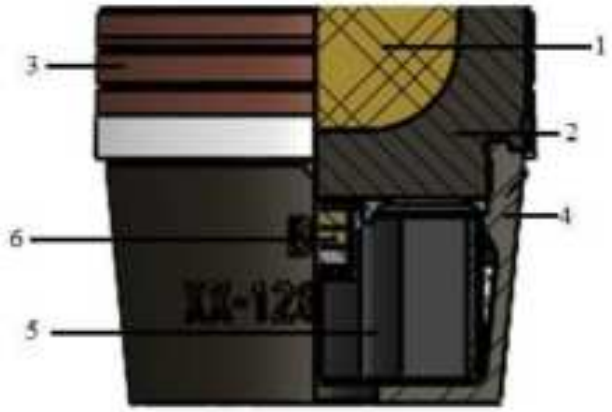

Figure 2: Base Exhaust Generator

1 – Effective charge, 2 – Projectile body, 3 – Driving band, 4 – Rear ogive, 5 – Generator charge, 6 – Ignition component

In the first principle: the source is the gas released around the base of the projectile, which also partially compensates for the base drag of the projectile. Such drag occurs behind the projectile moving at supersonic speed, where a reduced pressure is created, increasing the drag on the projectile. The use of a gas generator leads to a reduction in the pressure difference and a decrease in this drag [5].

The second principle: utilizes the combustion of solid propellant – material. The gases produced during combustion fill the space behind the projectile, as the outflowing gas velocity is less than the speed of the projectile [2].

In both principles, the influence of turbulent air flow behind the projectile is reduced [2].

When designing the base exhaust, it is essential to ensure its ability to withstand a significant drop in pressure when fired from the barrel. Equally important is ensuring reliable ignition of the propellant. During firing, the propellant charge is ignited, but when exiting the barrel, as the propellant gases – combustion products expand and pressure drops to a level similar to the surrounding atmospheric pressure, there is a high probability that the charge will extinguish. Therefore, it is crucial for the igniter to have a long operational duration to ensure re-ignition of the propellant [10].

Since the base exhaust addresses the issue of base drag, it is suitable to utilize the space of the hollow cavity for its placement. This way, the internal volume of the projectile, which houses the explosive, is not reduced, and the projectile's impact on the target is not compromised. If the base exhaust is placed in the hollow cavity, an increase in range of 13 to 32% can be achieved without changing the external shape
[10].

The charge of this gas exhaust generator may consist of solid propellants that have either a *heterogeneous* or homogeneous *(pyrotechnic*) character [9].

2.2 Hollow base

The method to reduce projectile drag lies in increasing the pressure behind the rear cross-section. This is achieved by shaping the base of the projectile into a suction cavity. This cavity enhances the stability of the projectile and reduces the area of turbulent flow behind it [10].

The rear part of the projectile, shaped like a cone or rear ogive, possibly incorporating a suction cavity, significantly reduces the base drag acting on the projectile. This influences the overall drag of the projectile and thus its range [10]. Research has also focused on the base sections of projectiles and how to alter their shapes, which are not completely symmetrical. These sections were shaped by cutting the base cylinder at a smaller angle, resulting in flat surfaces at the rear of the projectile, such as squares or triangles. Testing has shown that such shapes have advantages over the traditional conical shape, although their production is complex [10].

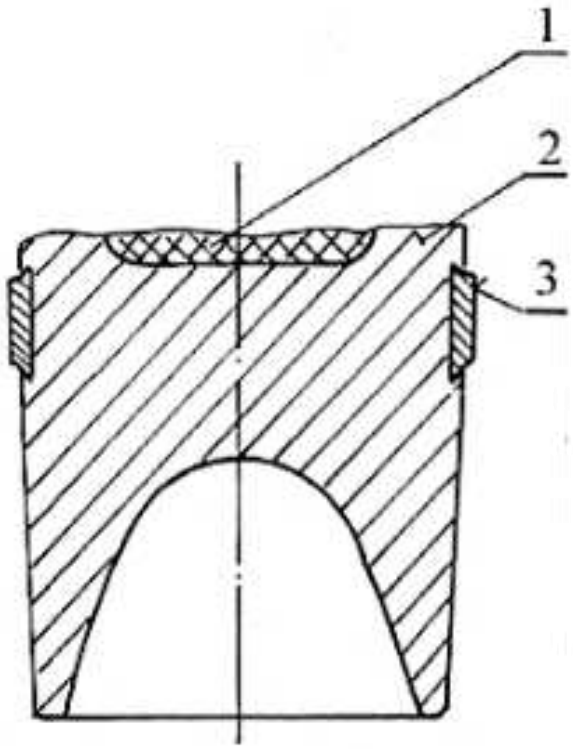

Figure 3: Suction Cavity

1– Effective charge 2 – Projectile body 3 – Driving band

3. IDEOLOGICAL PROJECTILE DESIGN

Figure 4: M107 155mm

According to the $\sigma = \frac{N}{b \cdot n_d \cdot h_d}$, it is possible to determine the stress at any point of the projectile. For this projectile, five points were chosen where this stress and centrifugal force will be calculated. Table 1 contains the input parameters for all points, and for better illustration and explanation, the calculation procedure will be demonstrated for one point.

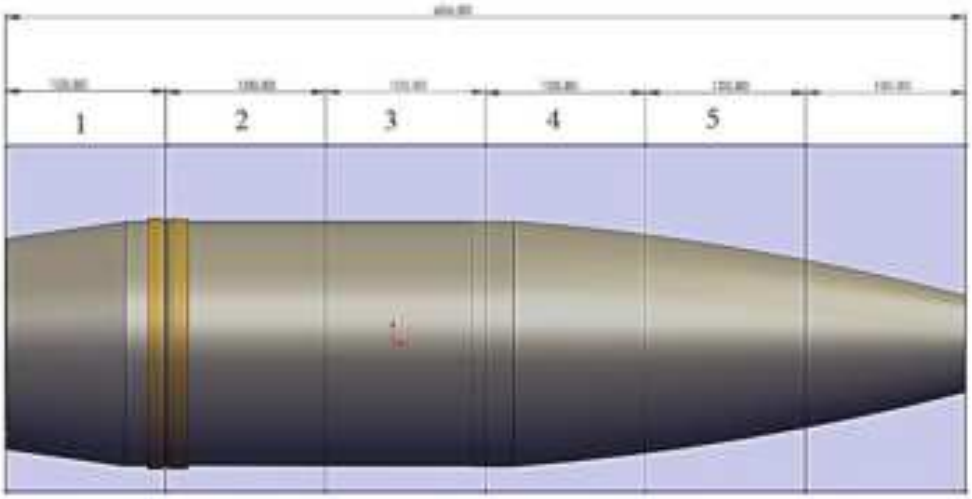

Figure 5: Points for Calculation

Where N - normal reaction [N],

b - the mean width of the guide rim [mm],

n_d - number of grooves in the barrel [mm],

h_d - groove depth [mm].

Tab. 1: Input parameters for the calculation

Cross-section	*-*	*1*	*2*	*3*	*4*	*5*
Yield strength(mat. 12 061)	*MPa*	500	500	500	500	500
Calibre	*mm*	155	155	155	155	155
Outer diameter	*mm*	153,9	154,2	154,75	137,83	105,87
Inner diameter	*mm*	104,3	122,72	123,14	107,36	76,15
Gas pressure	*MPa*	286	286	286	286	286
Total weight of the projectile	*kg*	38,365	38,365	38,365	38,365	38,365
Weight over cross-section	*kg*	27,892	20,169	13,705	7,342	2,608

Cut1

Procedure:

- Insert the input values from Table 1 into the formula [12]:

$$\sigma = \frac{155^2}{150{,}96^2 - 92{,}78^2} \cdot \frac{27{,}892}{38{,}365} \cdot 286$$

$$\sigma = 390{,}06 MPa$$

Compare the result with the yield strength for this calculation:

$$\sigma < \sigma_{mk}$$

$$390{,}06\ MPa < 500\ MPa \longrightarrow \text{COMPLIES!}$$

Tab. 2: Stress Results in Individual Cuts

Cross-section	*-*	*1*	*2*	*3*	*4*	*5*
Stress	*MPa*	390,06	414,37	279,43	176,01	86,34

Table 2 shows the results in the given cross-sections, if we compare them with the specified yield strength (500 MPa, material 12 061), we find that in all arbitrarily specified cross-sections *it satisfies* in terms of its stress.

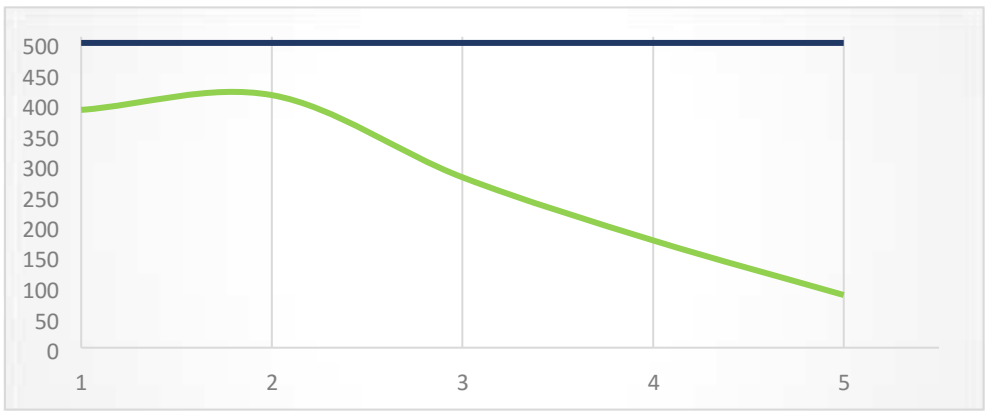

Graf 1: Stress Profile

The loading of the projectile due to centrifugal force is determined using the formula:

$$\sigma_d = \frac{\gamma}{3\,000g}\left(R^2 + Rr + r^2\right)\omega^2$$

where: γ - specific weight [g.cm-3],
g - acceleration due to gravity [cm/s2],
R - outer radius of the projectile body [mm],
r - inner radius of the projectile body [mm],
ω - angular velocity of the projectile [s-1].

From this relationship, it follows that the dynamic stress in a rotating projectile depends only on the materials from which the projectile body is made, as well as on the inner and outer diameters and the square of its angular velocity [12].

This force is determined at the same cut points with the same input parameters as indicated in Table 1, which will be supplemented with additional data in Table 3 for the calculation needs.

Tab. 3: Additional input parameters for the calculation

Cross-section	-	*1*	*2*	*3*	*4*	*5*
Specific gravity	$g.cm^{-3}$	7,85	7,85	7,85	7,85	7,85
Earth's gravity	$cm.s^{-2}$	9,81	9,81	9,81	9,81	9,81
Angular velocity	*s-1*	1205,43	1205,43	1205,43	1205,43	1205,43

Cut 1

Procedure:

$$\sigma_d = \frac{7{,}85}{3\,000 \cdot 9{,}81} \cdot \left(76{,}95^2 + 76{,}95 \cdot 52{,}15 + 52{,}15^2\right) \cdot 1205{,}43^2$$

- σ_d multiply by 100 000 to give the result in MPa.

$$\sigma_d = 49{,}04MPa$$

At that point, a centrifugal stress of *49.04MPa* is generated.

Tab. 4: Results of centrifugal stresses in individual cross-sections

Cross-section	-	*1*	*2*	*3*	*4*	*5*
Centrifugal force	*MPa*	49,04	55,97	56,36	43,91	24,29

Additional necessary calculations for this design involve calculations for the guide ring. The input parameters for the following calculations are provided in the table below, Table 5.

Tab. 5: Input Parameters for the Guide Ring

Ring Width	*[mm]*	25,42
Outer diameter of the Ring	*[mm]*	158
Inner diameter of the Ring	*[mm]*	153,2
Density of the Ring material	*[kg.m]*$^{-3}$	8 900
Weight of the ring	*[kg]*	0,264 422
Calibre	*[mm]*	155
Barrel twist Rate	*[-]*	0,157 08
Yield Strength (Copper)	*[MPa]*	80
Angular velocity	*[with]*$^{-1}$	1 145,16

The stress acting on the ring can be calculated using the formulas:

$S = \frac{D_2 - D_1}{2} \cdot b$ and $F = m \cdot \omega^2 \cdot r^2$

Where: *m* – mass of the ring [kg],

ω – angular velocity [s^{-1}],

r – mean diameter of the ring [m]; this mean diameter is obtained by summing the outer and inner diameters of the ring, which is then divided by 4.

b – mean width of the guide ring [mm],

D_2 - outer diameter of the considered cross-section [mm],

D_1 - inner diameter of the considered cross-section [mm].

These components relate to the stress ratio:

$$\sigma = \frac{F}{S}$$

Where F is the centrifugal force and S is the cross-sectional area of the ring [12].

$$F = 0{,}264\,422 \cdot 1\,145{,}16^2 \cdot 0{,}077\,8^2 = 2\,227{,}839N$$

$$S = \frac{158 - 153{,}2}{2} \cdot 25{,}42 = 61{,}008\ mm^2$$

$$\sigma = 36{,}517\,17 \rightarrow \underline{\text{COMPLIES}}$$

$$34{,}533\,6\ MPa < 80MPa$$

When *calculating the pressure* on the guide ring, it is necessary to compute the individual components using the input parameters as follows:

The formula includes the normal reaction, which is not an input parameter; therefore, it is defined by the relationship [12]:

$$N = pF\left(\frac{2Q}{d}\right)^2 \cdot \frac{tg\alpha}{cos\alpha - f sin\alpha}$$

Where: p – gas pressure in the barrel [MPa]

α – angle of twist [-]

F – cross-section of the barrel [mm²], determined by the calculation of input parameters [12]:

$$F = \frac{\pi D^2}{4} + n_d B h_d \left[1 + \frac{1}{6}\left(\frac{B}{D}\right)^2\right]$$

Where: D – inner diameter of the barrel [mm],

n_d – number of grooves in the barrel [-],

B – groove width [mm],

h_d - groove depth [mm]; for this quantity, the empirical formula applies, which can determine the minimum and maximum groove depth:

$$h_d = (0{,}010 \div 0{,}015) \cdot D$$

$\left(\frac{2Q}{d}\right)^2$ – the square of the ratio of the moment of inertia radius to the half-caliber of the gun, which is a constant value of 0.56 for this calculation;

$\frac{tg\alpha}{cos\alpha - f sin\alpha}$ – the value of this expression can be found in tables, for this calculation, the value is 0.163526.

Tab. 6 Additional Parameters for Calculating the Guide Ring

Gas Pressure in the Barrel	*[MPa]*	169
Inner Diameter of the Barrel	*[mm]*	154,94
Number of Grooves in the Barrel	*[-]*	48
Groove Width	*[mm]*	6,332
Groove Depth	*[mm]*	1,27
Allowable Pressure	*[MPa]*	260

After substituting the parameters from Table 8, we can calculate the following [12]:

$$F = \frac{\pi 154{,}94^2}{4} + 48 \cdot 6{,}332 \cdot 1{,}27\left[1 + \frac{1}{6}\left(\frac{6{,}332}{154{,}94}\right)^2\right] = 19\,240{,}69 mm^2$$

$$N = 169 \cdot 19\,240{,}69 \cdot 0{,}56 \cdot 0{,}163\,536 = 297\,770{,}9N$$

Thus, by substituting these values into the formula, we can calculate the pressure in the ring:

$$\sigma = \frac{297\,770{,}9}{25{,}42 \cdot 1{,}27 \cdot 48} = 192{,}159\,4 MPa \rightarrow \text{COMPLIES!}$$

Comparing the resulting pressure in the ring with the allowable pressure, we can conclude that these input parameters and additional parameters are satisfactory.

In these calculations, we can observe how the stress changes with respect to the muzzle velocity in the barrel. When calculating stress, we monitor the transfer of torque to the ring. By continuously increasing the aforementioned muzzle velocity, we can determine exactly when it exceeds the yield strength, as shown in Graph 2.

From this Graph 2, we can read that the x-axis represents the muzzle velocity in m/s, while the y-axis represents stress in MPa. With a constant increase in velocity (+50 m/s), the increase in stress is proportional, reaching the yield strength at a velocity of 859.949 m/s, and beyond this value, it behaves similarly.

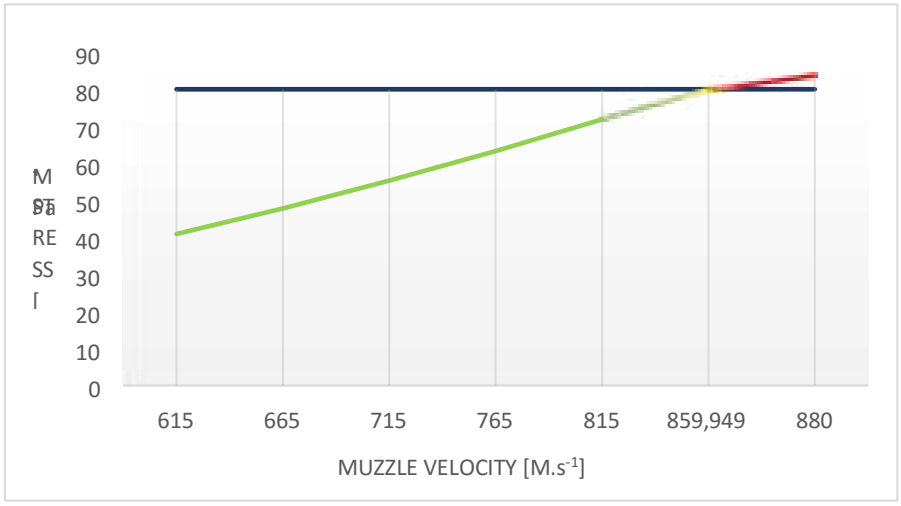

Graf 2: Stress Variation with Speed

The projectile, while moving in the barrel, generates friction work (A) on the ring, which can be expressed as:

$$A = 50{,}234 \cdot G\left(\frac{v_o}{100}\right)^2 \cdot \frac{tg\alpha}{cos\alpha - f sin\alpha}$$

Where all values are known, the allowable friction work for this projectile is set at a value of 10. In Graph 3, we will demonstrate the relationship between friction work and muzzle velocity.

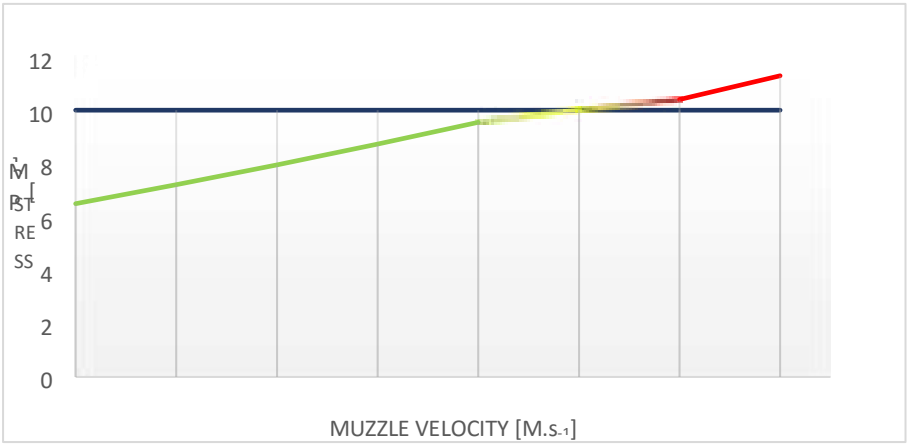

Graf 3: Dependence of Work on Muzzle Velocity

From graph 3, it is evident that the x-axis represents the coordinates of muzzle velocity in m/s, while the y-axis indicates the amount of work in kg·m. According to the graph's trend, we can deduce that the permissible work is achieved at a muzzle velocity of 701.2138 m/s. Even after exceeding this threshold, the trend continues in a straight line. In

this case, with a low value for permissible work, it was sufficient to increase the velocity by 30 m/s.
As we continue to increase the velocity, we will show how this affects the projectile itself, as depicted in graph 4.

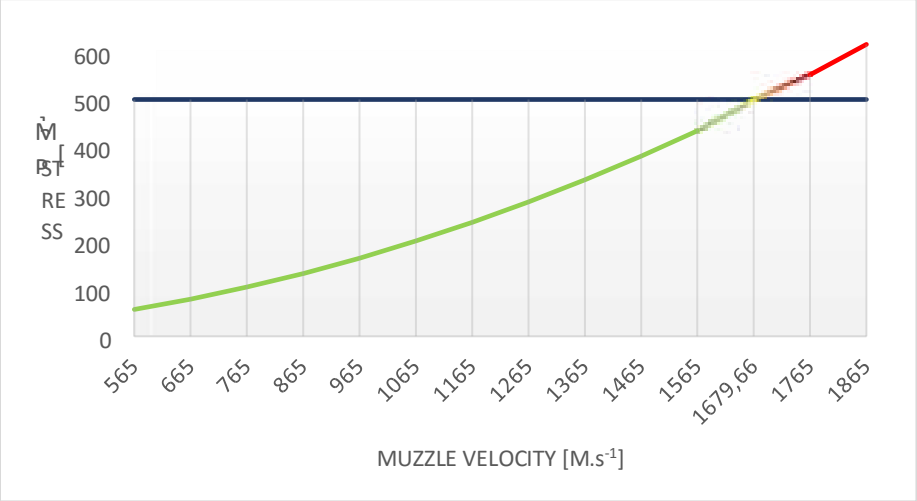

Graf 4: The relationship between bullet strength and muzzle velocity.

On the x-axis, we have velocity in $m.s^{-1}$, which consistently increases by 100 $m.s^{-1}$ increments, while on the y-axis, the scale represents stress in MPa. At first glance, it is evident that for the projectile body to reach equivalence with the yield strength threshold, it requires higher values of muzzle velocity than the guiding band. This yield strength is reached at a speed of *1,679.66 $m.s^{-1}$*.

Using simulations, we can determine the range of this projectile. Given that the permissible work for this projectile is set to 10, the input velocity parameter is defined by the maximum value it can sustain. From calculations, this value was determined to be approximately 702 $m.s^{-1}$. At this point, the guiding band ceases to transmit torque, creating excessive friction, which may lead to deceleration of the projectile by the guiding band.

From Figure 6, we can see that with the correct elevation and this muzzle velocity, the projectile can achieve a maximum range of 18,000 meters. The x-axis indicates distance in meters, while the y-axis shows height, also in meters.

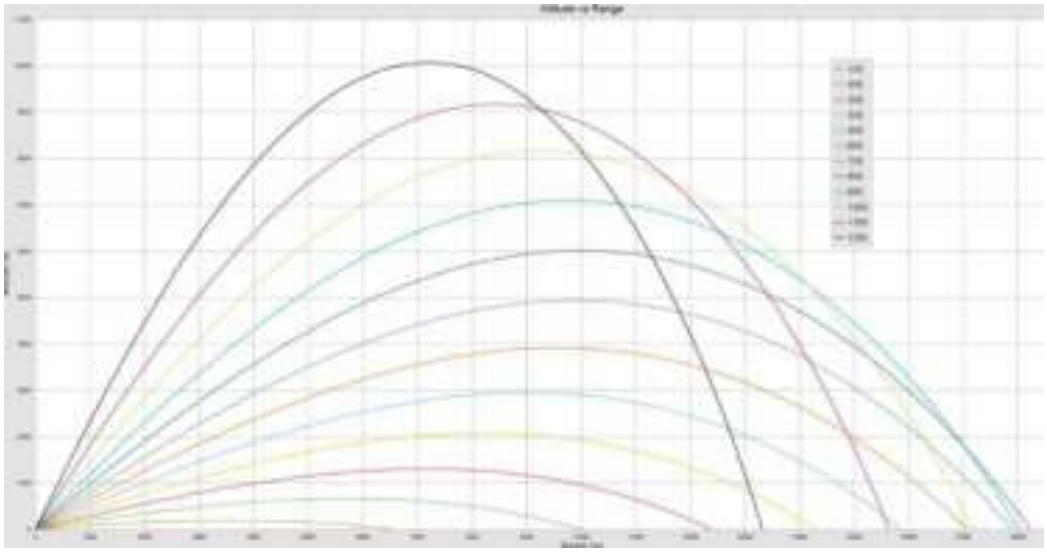

Figure 6: Simulation of the M107 Range

In the introduction of the article, we outlined the types of charges this projectile can contain. The most suitable for this caliber is the M119A2 charge, which allows the projectile to reach its maximum possible range at an optimal angle and a velocity *of 682 m.s⁻¹*, as shown in Figure 7.

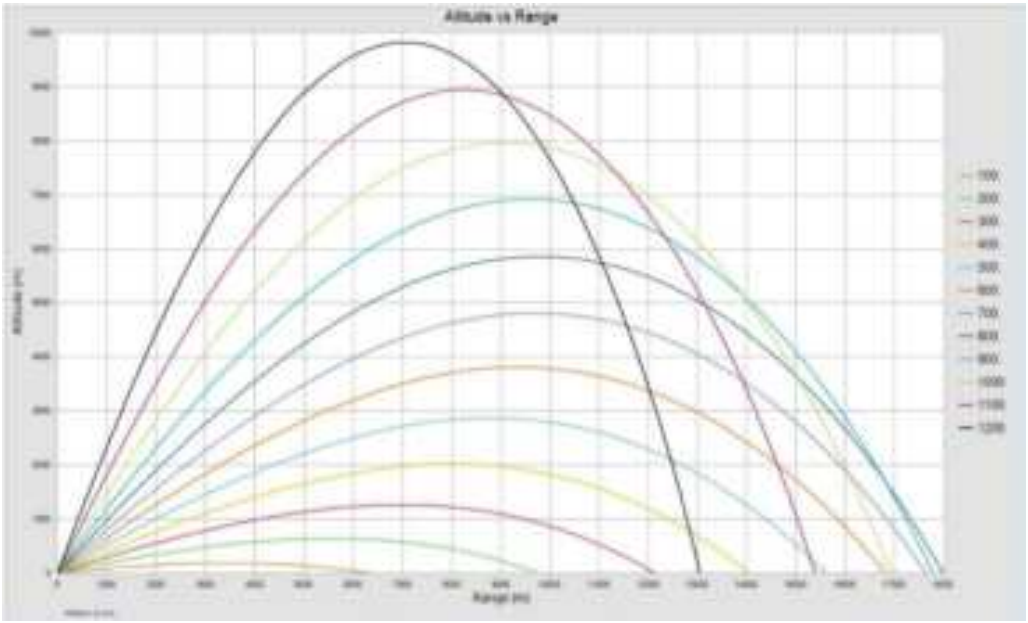

Figure 7: Simulation M107_M119A2_682m/s

Due to the larger cartridge chamber and longer barrel, the pressure in the chamber upon firing decreases, and therefore, the muzzle velocity does not increase accordingly and remains the same. For comparison, we present simulations with the same muzzle velocity of *682 m.s⁻¹* and the same M119A2 charge but with different barrel lengths of 39 cal and 52 cal.

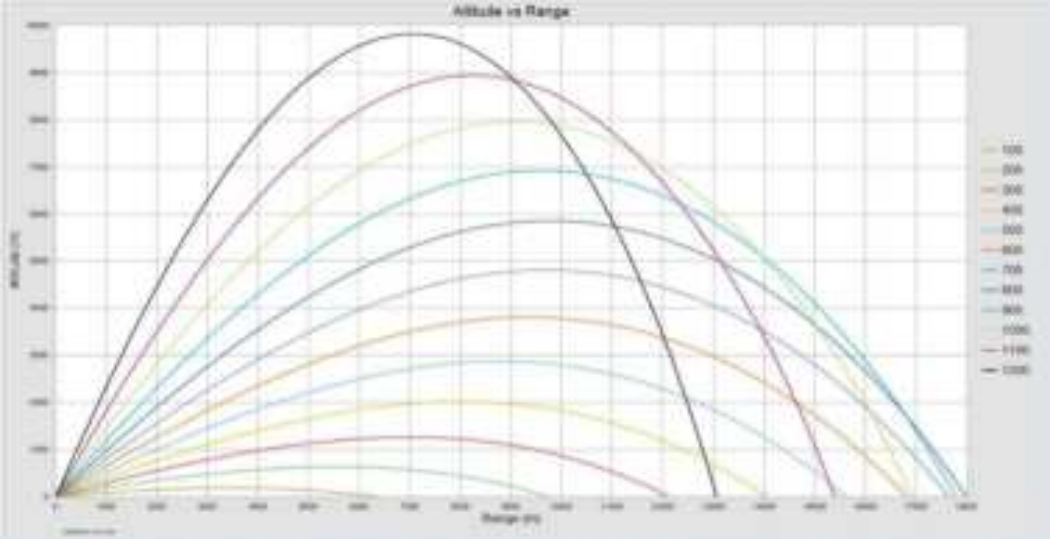

Figure 8: 39. cal M119A2 682m.s-1

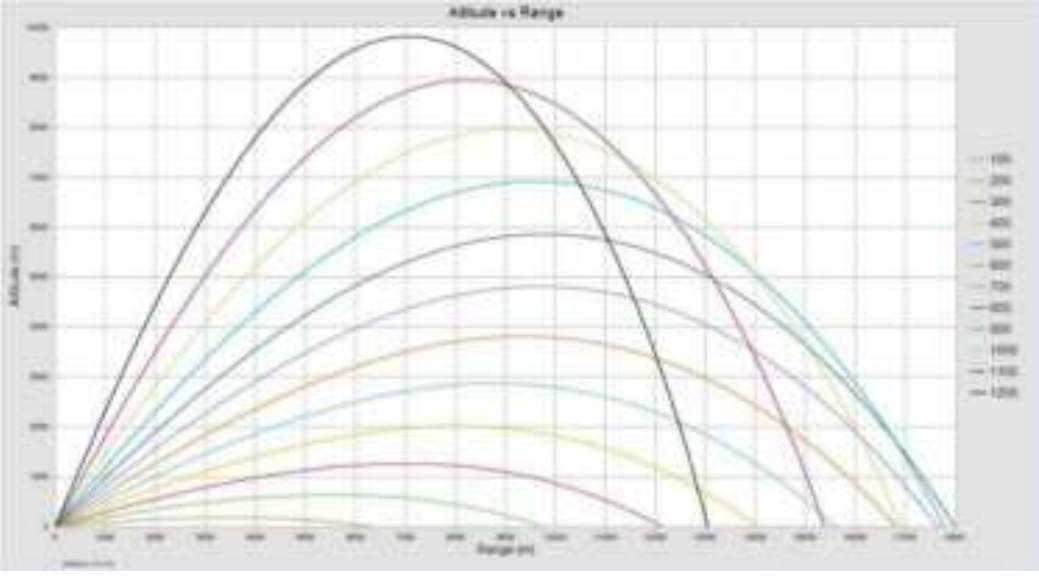

Figure 9: 52 cal. M119A2 682m.s-1

The projectile is designed so that it does not exceed a speed of approximately *700 m/s.* If it surpasses this threshold, frictional work increases, which would cause significant issues for the projectile's movement within the barrel. This could lead to the rotation band slipping or being stripped, preventing the projectile from achieving the required spin, thereby reducing its stability and leaving it gyroscopically destabilized. This phenomenon results in irregular flight and a significant reduction in range. In extreme cases, the range reduction could be so severe that fire is directed onto friendly territory.

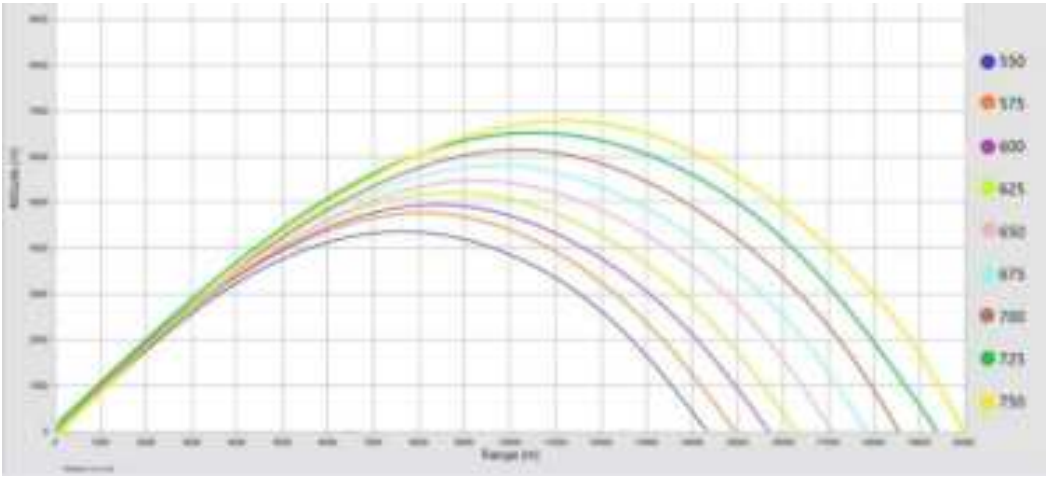

Figure 10: Range Simulation

In Figure 10, it is possible to see the range of the 155mm M107 projectile at optimal elevation and given muzzle velocities, without considering its maximum possible speed as limited by frictional work.

4. CONCLUSION

This projectile has a range of 18 km under suitable conditions. Possible optimization proposals include changing materials or increasing the number of guiding rings.

If the strength of the projectile body is inadequate, its material could be changed from *12 061* to *13 270*. This would increase the yield strength from approximately 500 MPa to about *720 MPa*.

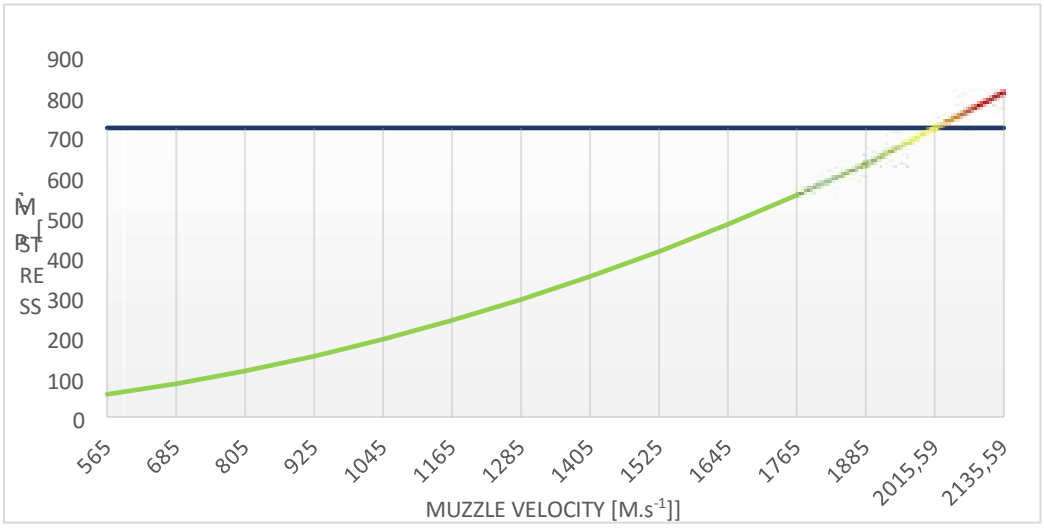

Graf 5: Dependence of Projectile Body Strength on Muzzle Velocity – Optimization

If we compare graph 4 with this graph 5, we see that to achieve the yield strength, we need to develop a muzzle velocity *of 2,015.59 m/s*. By using a new material for the projectile body, the maximum muzzle velocity increased by approximately *336 m/s*.

The guiding ring can be optimized by increasing the nickel content in the material and also by securing the ring to the projectile. By increasing the nickel content in the material by 7 - 7.5%, the yield strength of the guiding ring increases by approximately *250 MPa*.

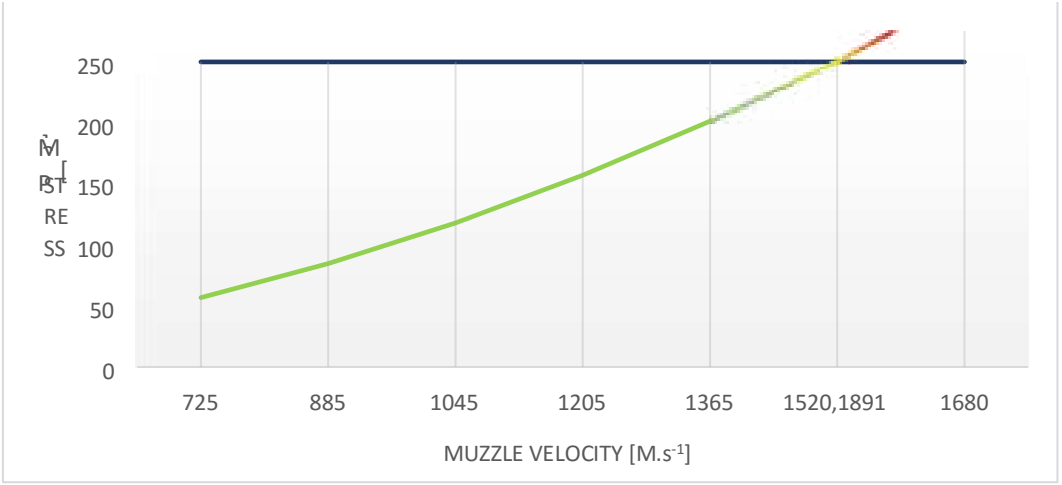

Graf 6: Stress behavior in the ring as a function of speed – optimization

By comparing graph 6 with graph 2, we can see that increasing the yield strength significantly changes the muzzle velocity. The previous graph shows that the yield strength is exceeded at a speed of *859.949 m/s*, but with this optimization, we can raise this limit to *1520.1891* m/s, resulting in an increase in speed of approximately 660 m/s.

Due to the increase in these values, the given ring would not suffice with its current performance; therefore, the next step in optimizing the guiding ring and thus the entire projectile is to weld this ring to the projectile. This process will double its allowable friction work and thus its strength.

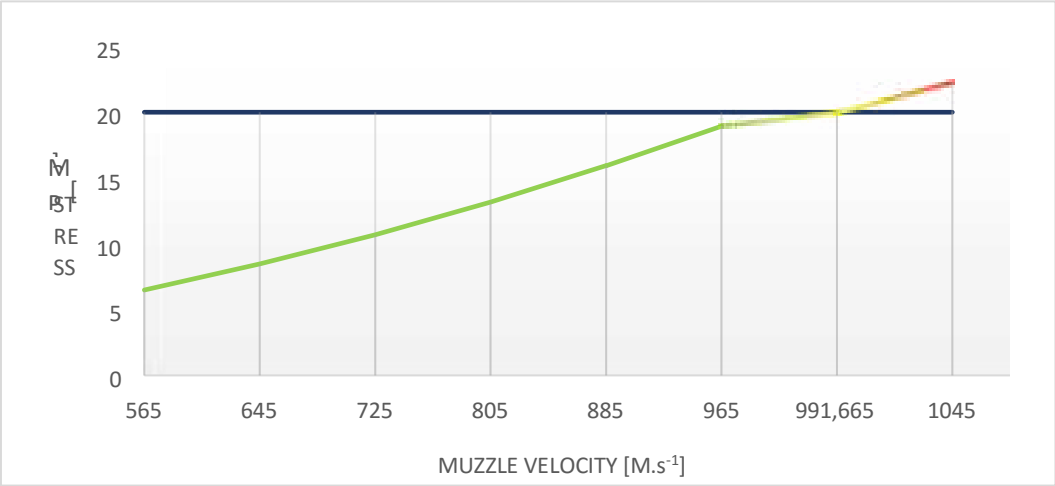

Graf 7: The course of transferred work with respect to speed - optimization

By comparing graph 7 and graph 3, we can see that the required speed to achieve the allowable work has significantly increased. In previous calculations, the allowable work was valued at 10, and its speed was *701.218 m/s*. In this case, we increased its strength by welding, thus achieving a value of 20, and the speed increased to *991.665 m/s*. The muzzle velocity increased by approximately *290 m/s.*

REFERENCES

[1] MSM GROUP. Slovensko. [online]. Dubnica nad Váhom. Available online: https://www.msm.sk/co-robime/obrana/municia/delostrelecka-municia/155-mmhe-m107/

[2] GALETA, A. – JOZEFEK, M. – LIPTÁK, P. 2005. *Munícia a výbušniny časť – Streliviny*, Trenčín: TnUAD, 2005. 100 s., skriptum

[3] GREXA, J. – ŘEBÍČEK, V. 1972. *Munice I.* Brno: VAAZ, 1972. 209 s.

[4] KOLEKTÍV AUTOROV. 1976. *Speciálni technika I. díl*. Praha: FMVS Praha a GŘt ZVS Brno 1976. 536 s.

[5] KUSÁK, J. 2003. *Základy konstrukce munice I*. Pardubice: Univerzita Pardubice, 2003. 272s. ISBN 80-7194-62-9X

[6] JANČO, J. 2002. *Výbušniny, základy munície a výroba munície I diel.* Trenčín: TnUAD, 2002. 170s., Učebné texty k predmetu Výroba munície

[7] BEER, S. – KOMENDA, J. – JEDLIČKA, L. 2004. *Munice*. Brno: Univerzita obrany. 2004. 406s. skriptum

[8] KOLEKTÍV AUTOROV. 1976. *Speciálni technika II. díl*. Praha: FMVS Praha a GŘt ZVS Brno 1976. 480 s.

[9] MSM GROUP. Slovensko. *Interné dokumenty 1*. Dubnica nad Váhom.

[10] ZLATOVSKÝ, P. *Analýza dostrelu diaľkového delostreleckého granátu kalibru 155mm s predĺženou funkciou DV (dnového výtoku)*. Diplomová práca. Trenčín: Trenčianska univerzita Alexandra Dubčeka v Trenčíne, Fakulta špeciálnej techniky, 2014, 58 s.

[11] VUONO, C. 1990. *Military explosives.* USA [online] Washington, DC. 1990. 355s.

Available online:

https://www.bulletpicker.com/pdf/TM-9-1300-214-1984.pdf#page=223

[12] RAFTL, J. 1958. *Základy munice II. Konstrukční část.* Praha: studijní a informační ústav odborného školství. 1958.


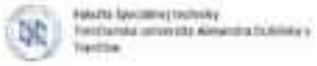





ISBN 978-80-8096-307-1

EAN 9788080963071